MASARYKOVA UNIVERZITA
PŘÍRODOVĚDECKÁ FAKULTA
Ústav teoretické fyziky a astrofyziky

DIPLOMOVÁ PRÁCE

BRNO 2023 KRISTÍNA KALLOVÁ

MASARYKOVA UNIVERZITA

PŘÍRODOVĚDECKÁ FAKULTA
Ústav teoretické fyziky a astrofyziky

Výzkum extrémně zakrytých galaktických jader v našem blízkém okolí

Diplomová práce

Kristína Kallová

Vedoucí práce:
Dr. Peter Boorman

Brno 2023

Bibliografický záznam

Autor:	Bc. Kristína Kallová Přírodovědecká fakulta, Masarykova univerzita Ústav teoretické fyziky a astrofyziky
Název práce:	Výzkum extrémně zakrytých galaktických jader v našem blízkém okolí
Studijní program:	Fyzika
Studijní obor:	Astrofyzika
Vedoucí práce:	Dr. Peter Boorman
Akademický rok:	2022/2023
Počet stran:	viii + 113
Klíčová slova:	rentgenovo zakrytá aktivní galaktická jádra, pozorování s nízkym počtem countů, XMM-Newton, NuSTAR, širokopásmová rentgenová reflexní spektroskopie, empiricky motivované modely torusů, NGC 3982

Bibliographic Entry

Author:	Bc. Kristína Kallová Faculty of Science, Masaryk University Department of theoretical physics and astrophysics
Title of Thesis:	Probing extremely obscured accretion in our cosmic backyard
Degree Programme:	Physics
Field of Study:	Astrophysics
Supervisor:	Dr. Peter Boorman
Academic Year:	2022/2023
Number of Pages:	viii + 113
Keywords:	X-ray obscuration of active galactic nuclei, low-count observations, XMM-Newton, NuSTAR, broadband X-ray reflection spectroscopy, empirically motivated torus models, NGC 3982

Abstrakt

Silně zahalená aktivní galaktická jádra (z angličtiny AGN) nabízejí jedinečnou příležitost ke studiu okolí akreujících supermasivních černých děr (z angličtiny SMBH). Studium zahalení AGN je klíčové pro pochopení komplexnosti jejich populace, protože většina AGN ve vesmíru je zahalena (Comastri, 2004). Rovněž nám může pomoci zodpovědět některé z hlavních otázek týkajících se vývoje galaxií a jejich společného vývoje s centrálními černými dírami. Právě potrava černých děr je pravděpodobně tím, co nám zakrývá výhled, a proto nám studium cirkumnukleární oblasti může také pomoci pochopit proces pohánění i růstu většiny populace AGN, k němuž dochází pravděpodobně během silně zastíněných fází prudké akrece (Fabian a spol., 2000). Nová observatoř v tvrdém rentgenovém pásmu (*NuSTAR*) představila novou éru studia takových systémů, neboť pozorovaný tvar spektra v pásmu > 10 keV je klíčový pro pochopení geometrických a fyzikálních vlastností stínícího torusu, stejně jako pro odhad vlastních parametrů systému, jako je vlastní rentgenová svítivost nebo Eddingtonův poměr.

V této práci představuji detailní studium hluboce zakryté akreující SMBH v Seyfertově galaxii 2 NGC 3982 pomocí dalekohledů *XMM-Newton* a *NuSTAR*. Na širokopásmové rentgenové spektrum zdroje jsem fitovala několik různých modelů stínícího materiálu, o němž se předpokládá, že se nachází ve vzdálenosti $\sim 1 - 10$ parseků od SMBH. Každý model reprezentuje jinou geometrii zakrývajícího cirkumnukleárního regionu, ale také porovnávám výsledky s empirickým modelem předpokládajícím nefyzikální polo-nekonečnou odraznou plochu. Pomocí platformy Bayesian X-ray Analysis (BXA), která spojuje balík Xspec pro fitování rentgenového spektra s vnořeným vzorkováním, je prozkoumán celý předdefinovaný prostor parametrů každého modelu, aby se odstranily problémy s lokálními minimy a přesně reprodukovaly degenerace parametrů. Všechny modely nalezly sloupcovou hustotu stínícího materiálu větší než 10^{24} cm^{-2}, což potvrzuje silně zahalenú povahu zdroje, a vlastní rentgenovou svítivost v pásmu $2 - 10$ keV $\log L_{2-10\ \mathrm{keV}} = 41,4$ erg s^{-1} pro nejvíce pravděpodobný model založený na komplexní shlukovité geometrii s více reflektory, UxClumpy. Vzhledem k tomu, že studovaná AGN je ze své podstaty málo svítivý zdroj a je silně zakrytá, jsou geometrické vlastnosti torusu s ohledem na kvalitu dat špatně omezeny a všechny modely poskytují zhuba konzistentní výsledky. Nicméně pomocí simulací spekter High Energy X-ray Probe (*HEX-P*, nadcházející mise NASA typu sondy) z nejpravděpodobnějšího modelu pro NGC 3982 s využitím složité geometrie s více diskrétními reflektory ilustruji budoucí potenciál pro citlivé studia stínících torusů i mezi populací AGN s nízkou svítivostí.

Abstract

Heavily obscured Active Galactic Nuclei (AGN) offer a unique opportunity to study the circumnuclear environment in accreting supermassive black holes (SMBH). Study of the obscuration in AGN is crucial for comprehension of complexity of the AGN population as most of the AGN in the Universe are obscured (Comastri, 2004). It can also help us to answer some of the major questions regarding the galaxy evolution and its coevolution with the central black holes. The food of black holes is likely what is obscuring our view, thus studying the circumnuclear region can also help us understand the fuelling process as well as the growth of the bulk of the AGN population, occurring likely during heavily obscured phases of rapid accretion (Fabian et al., 2000). A new observatory in the hard X-ray band, *NuSTAR* introduced a new era for studying such systems as the observed spectral shape in the >10 keV band is crucial for understanding the geometrical and physical properties of the obscurer, as well as for the estimation of the intrinsic properties of the system such as the intrinsic X-ray luminosity or the Eddington ratio.

In this work I present a detailed study of the a deeply buried accreting SMBH in the Seyfert 2 galaxy NGC 3982 with *XMM-Newton* and *NuSTAR*. I fit several different models of the obscurer believed to be located within $\sim 1-10$ parsecs from the SMBH to the broadband X-ray spectrum of the source. Each model represents a different circumnuclear obscurer geometry but I also compare the results with empirical model assuming an unphysical semi-infinite reflecting slab. By using the Bayesian X-ray Analysis (BXA) platform that connects X-ray fitting package XSPEC with nested sampling, the full pre-defined parameter space of each model is explored to remove issues with local minima and reproduce parameter degeneracies precisely. All models find the column density of the obscurer above 10^{24} cm^{-2} confirming the Compton-thick nature of the source, and the intrinsic X-ray luminosity in the 2-10 keV band $\log L_{2-10\ \mathrm{keV}} = 41.4$ erg s^{-1} for the best-performing complex multi-reflector clumpy-geometry model, UXCLUMPY. As the studied AGN is intrinsically a low-luminosity source and heavily obscured, regarding the data quality, geometrical properties of the obscurer are poorly constrained and all the models are giving consistent results. However, by simulating High Energy X-ray Probe (*HEX-P*, an upcoming NASA probe class mission) spectra from the best-fit for NGC 3982 in a complex multi-reflector clumpy geometry I illustrate the future potential for sensitive studies of the obscurer geometry even amongst the low-luminosity AGN population.

MUNI
SCI

MASARYKOVA UNIVERZITA
PŘÍRODOVĚDECKÁ FAKULTA
KOTLÁŘSKÁ 2, 611 37 BRNO
IČ: 00216224
DIČ: CZ00216224

ZADÁNÍ DIPLOMOVÉ PRÁCE

Akademický rok: 2022/2023

Ústav:	Ústav teoretické fyziky a astrofyziky
Studentka:	Bc. Kristína Kallová
Program:	Fyzika
Specializace:	Astrofyzika

Ředitel *ústavu* PřF MU Vám ve smyslu Studijního a zkušebního řádu MU určuje diplomovou práci s názvem:

Název práce:	Výzkum extrémně zakrytých galaktických jader v našem blízkém okolí
Název práce anglicky:	Probing extremely obscured accretion in our cosmic backyard
Jazyk závěrečné práce:	angličtina

Oficiální zadání:
To answer the major open questions in supermassive black hole (SMBH) and galaxy evolution requires an unambiguous and robust selection strategy of growing SMBHs (aka active galactic nuclei; AGN). The majority of mass is accreted onto SMBHs behind thick columns of gas and dust, and it follows that an accurate assessment of the most obscured AGN is essential for a complete understanding of SMBH growth. However, current estimates of the fraction of heavily obscured AGN vary dramatically between ~20-70%, and it remains unclear whether this uncertain range is driven by selection biases, inadequate sample sizes, luminosity/accretion rate dependencies or something else entirely. To investigate such issues, this project will first involve a large-scale search and compilation of candidate heavily obscured AGN selected from literature and multi-wavelength photometric surveys. The student will then extract broadband X-ray spectra from NASA's NuSTAR hard X-ray telescope in combination with XMM-Newton and the Neil Gehrels Swift Burst Alert Telescope. By modelling the extracted spectra with physically-motivated state-of-the-art AGN obscurer models, complex geometrical and physical characteristics of the deeply buried accreting systems will then be inferred. The resulting catalogue of confirmed heavily obscured AGN will be extremely useful to the astrophysical community, and serve as a benchmark for next-generation surveys dedicated to a census of accretion in our cosmic backyard.

Vedoucí práce:	Dr. Peter Boorman
Datum zadání práce:	16. 12. 2020
V Brně dne:	27. 12. 2022

Zadání bylo schváleno prostřednictvím IS MU.

Bc. Kristína Kallová, 14. 1. 2021
Dr. Peter Boorman, 10. 5. 2021
Mgr. Michael Krbek, Ph.D., 14. 5. 2021

Acknowledgement

My greatest thanks goes to Peter for his infinite patience, countless consultations and discussions, repeated explanations and guidance throughout the entire work, conferences, meetings and presentations. You are the person responsible for my motivation and enthusiasm for the topic of my work and high energy astrophysics in general. Thank you! I am grateful also to Jirka Svoboda for all the support and multiple possibilities to visit the Astronomical Institute for meetings and also for the opportunity to attend an international conferences and financial support. Thanks Anastasyia and Romy for all the fun while learning new things, all your support and for standing by my side. I learned much from both of you! I also want to thank Norbert for providing motivating environment for students and bringing high energy astrophysics to Masaryk University. I am grateful to everyone in the HEA group as you guys are so supportive, it is also thanks to you I want to carry on in this field. Last but not least, thanks to my parents, my grand parents and especially my grand mother for blaming me for my incompetence. Thank you, Zdenda, for all those years discussing science and thank you, Matej, and everyone else who believed in me, for having so much faith in me. It pushes me forward.

Prohlášení

Prohlašuji, že jsem svoji diplomovou práci vypracovala samostatně pod vedením vedoucího práce s využitím informačních zdrojů, které jsou v práci citovány.

Brno 3. ledna 2023 . . . . . .

Kristína Kallová

Contents

Introduction

The cosmic X-ray Background (CXB) was the first cosmic background ever discovered (Giacconi et al., 1962), two years before the discovery of the famous Cosmic Microwave Background in 1964 (CMB, Penzias & Wilson, 1965). It is a largely isotropic emission with an extragalactic origin whose spectrum has shape of a broad bump ranging across wide range of wavelengths in the X-ray band (Gilli, 2013). At first sight it resembles a residual diffuse emission, but from detailed studies (Mushotzky et al., 2000) it has been shown, that the CXB above 3 keV is composed of emission from many individual unresolved point sources distributed isotropically across the sky, primarily of discrete accreting black holes in the centres of active galaxies. Active Galactic Nuclei (AGN) were confirmed to be the dominant contributors to the CXB (Fiore et al., 1999; Lehmann et al., 2000) and with deep observations performed by a more sensitive new-generation X-ray observatories a large fraction of these discrete point sources was resolved (Hasinger et al., 1993; Fiore et al., 2001). The average redshift of the objects contributing mostly to the observed CXB emission is believed to peak at $z \sim 1$ as at higher refshifts the AGN emission is redshifted to the softer wavebands (Ueda et al., 2014; Ananna et al., 2019).

To explain the spectral shape of CXB with the prominent peak at ~ 30 keV we need to assume that large fraction of AGN in the Universe are actually heavily obscured (Setti & Woltjer, 1989; Comastri et al., 1995), as its spectral shape resembles the one of typical reflection-dominated AGN in hard band (Matt et al., 2000). Despite this prediction shown by synthesis models of CXB (Ueda et al., 2003; Treister & Urry, 2005; Ballantyne et al., 2006; Gandhi et al., 2007; Gilli et al., 2007; Treister et al., 2009; Akylas et al., 2012; Ueda et al., 2014; Comastri et al., 2015), the intrinsic fraction of Compton-thick AGN is highly uncertain (Brightman & Ueda, 2012). Additionally, there is only a small fraction of heavily obscured AGN observed in the local Universe varying significantly from the predicted values, as they are observationally challengeable to detect and identify. In the local Universe the best way for identifying heavily obscured AGN is in the hard X-ray band, as at higher energies the emission becomes less affected by the gas and dust absorption (Ricci et al., 2015).

The thesis is structured in the following way. Chapter 1 summarizes the fundamental information about AGN. The composition of an AGN with the description of all its components is in section 1.1. Section 1.2 characterizes the broadband emission from an AGN with the focus on the X-ray band in section 1.2.1. AGN classification with the basic characteristics of the AGN family members is in the section 1.3 together with the Unified Model description in section 1.3.4. The first chapter ends with more detailed characterization of obscured AGN in section 1.4. Chapter 2 describes the methodology of the work. Sections 2.1 and 2.2 describe the X-ray observatories *XMM-Newton* and *NuSTAR* respectively with the basics of the data reduction in the subsections. The fundamental approach to the X-ray spectral analysis is in the section 2.3 with brief description of the applied statistic, used binning methods and the characterisation of the complex spectral models in subsection 2.3.3. Bayesian X-ray Analysis is discussed in section 2.4. In 3rd chapter the spectral analysis is presented. Section 3.1 summarizes the information about NGC 3982 from the literature and the spectral analysis performed locally in the Xspec fitting package and with the Bayesian approach is summarized in sections 3.2 and 3.3, respectively. Chapter 4 discusses the future prospects of this work.

1 Active galactic nuclei

Active Galactic Nuclei (AGN) are among the most luminous sources of electromagnetic radiation, as they are powered by accretion onto compact supermassive black holes (SMBHs, with masses approximately $10^5 - 10^{10} M_\odot$) in their centres. Their bolometric luminosities can reach non-negligible fractions of Eddington limit for black holes, as in the case of powerful quasars. Even though AGN are typically very bright sources across the entire electromagnetic spectrum, in this work I focus on the emission of X-rays in the energy band $0.3 - 78.0$ keV, emitted only by very hot and energetic processes in the Universe, as they trace the very inner regions of these compact systems.

1.1 Composition of an AGN

AGN are believed to consist of several components described each individually in this section. Generally the nucleus of an active galaxy spans across several orders of magnitude in size, from the SMBH in the very center of an AGN with sizes around 10^{-5} of a parsec, up to the torus and the narrow line region located at several units of parsecs up to hundreds of parsecs respectively from the central engine. All components described in this section can be found in the order corresponding their location in the AGN: from the smallest scales in the very center to the host-galaxy scales. The illustration of an AGN and its components is in the figure 1.1.

1.1.1 Supermassive Black Hole

Black holes are the most massive and compact objects known in the Universe hiding singularity in their centres. The strong gravitational fields of black holes cause that not even light can escape from below the so called event horizon, which is the boundary where the escape speed equals the speed of light c. Generally a black hole can be described only by three properties; its mass, angular momentum or spin, and charge; even though the charge is often assumed to be zero for the neutral black holes.

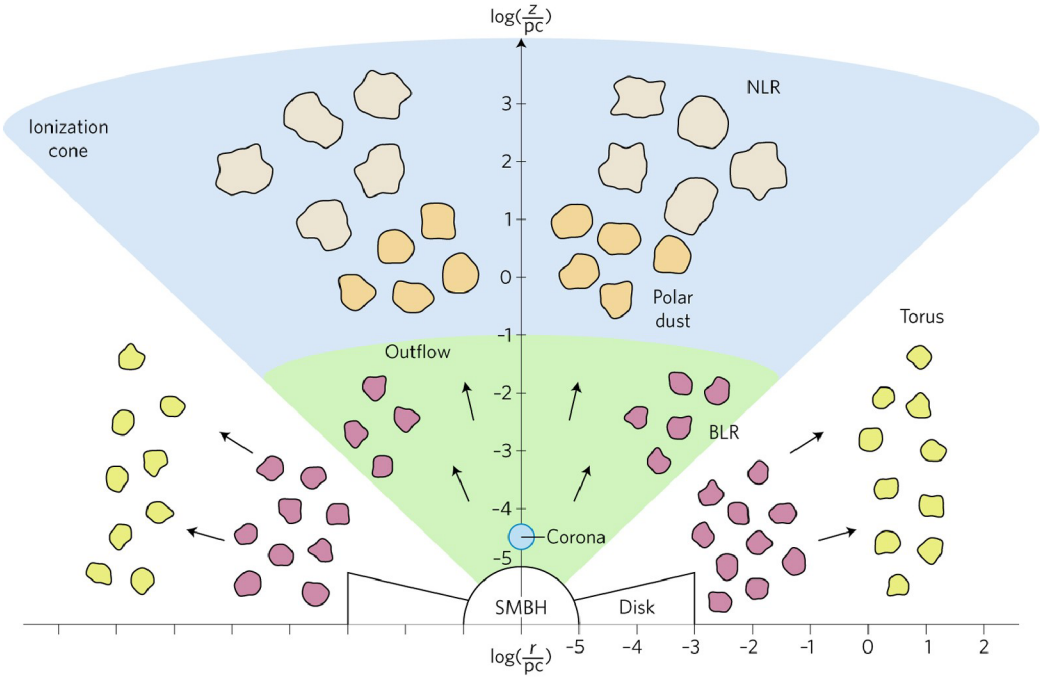

Figure 1.1: Figure adapted from Ramos Almeida & Ricci, 2017 shows a sketch of AGN components along the equatorial and polar directions with corresponding scales. From the center of an AGN to the galactic scales the components are: SMBH, accretion disc and corona, BLR, obscuring torus, NLR located within the ionization cone. Colours indicate different composition and/or different densities.

It has been shown that in the very center of the AGN there is a compact SMBH with masses ranging from fraction of millions of Solar masses up to tens of billions of Solar masses ($10^6\ M_\odot - 10^9\ M_\odot$). The radius of the event horizon is usually given in the units of gravitational radii r_g;

$$r_g = \frac{GM_{BH}}{c^2} \tag{1.1}$$

where G stands for the gravitational constant with defined value of $G = 6.674\times 10^{-11}$ $m^3kg^{-1}s^{-2}$ and M_{BH} is the mass of the black hole. Another significant radius is described by the innermost stable circular orbit r_{ISCO}, which is the distance from the event horizon where the particles orbiting the black hole fall directly into the black hole's singularity. The radius if the innermost stable circular orbit is given in the gravitational radii r_g and is highly dependent on the black holes angular momentum.

The AGN is located within the sphere of influence of the black hole, where its gravitational potential dominates over the gravitational potential of the host galaxy. The gravitational influence radius r_{h} is dependent except of the black hole mass on the velocity dispersion of the host galaxy bulge σ.

$$r_{\mathrm{h}} = \frac{GM_{\mathrm{BH}}}{\sigma^2}. \tag{1.2}$$

1.1.2 Accretion Disc

The formation of the accretion disc happens when a gas clouds falling towards the central SMBH lose their potential energy in favour of their kinetic energy. A part of the potential energy is transformed into the thermal energy and the gas clouds are heated. Due to collisions between the individual clouds, their orbits are becoming circular. As the particles in the newly formed disc are moving at the Keplerian orbits, the inner parts are moving with larger velocities than the outer parts of the disc and the friction leads to kinetic energy loss and more heating to temperatures up to $\sim 10^4$, so the discs thermal emission peaks at optical-UV band. The angular momentum is transported by viscous forces within the disc towards its outer edge, and the outer parts spiral inwards to the smaller circular orbits up to the innermost stable circular orbit, from where the matter falls directly into the black hole.

The accretion disc spans at distances around 10^{-3} to 10^{-2} parsecs from the central engine and it gets hotter and brighter towards its inner edge. Nearest to the central black hole it reaches supersonic velocities.

Accretion power

The accretion of matter onto a compact object is one of the most efficient process of conversion of mass into energy in the Universe. If a mass m is accreted onto an object, the energy gain is dependent on its compactness, therefore on the M/R fraction as follow

$$\Delta E_{\mathrm{acc}} = \frac{GMm}{R}. \tag{1.3}$$

The energy gain can be also written as

$$\Delta E_{\mathrm{acc}} = \mu mc^2, \tag{1.4}$$

where μ is the efficiency of conversion of the rest-mass energy of the accreted matter into the thermal energy. Therefore the efficiency of the accretion process can be expressed in dependence of the compactness in following way

$$\mu = \frac{GM}{Rc^2} \tag{1.5}$$

In AGN, the accretion efficiency of the mass rest energy reaches between $\mu = 0.06$ for Schwarzschild black hole up to enormous $\mu = 0.426$ for maximally rotating Kerr black hole (Longair, 2011). Comparing this to the greatest release of nuclear energy occurring in the thermonuclear synthesis of hydrogen into helium for which $\mu = 7 \times 10^{-3}$ or 0.7%, the accretion onto black holes is more than an order of magnitude more efficient. In particular the accretion onto maximally rotating black holes stands for the most powerful energy sources known in the Universe.

If the mass rate at which the matter is accreted is $\dot{m}$, the luminosity of such accreting source $L_{\rm acc}$ would be defined as

$$L_{\rm acc} = \mu \dot{m} c^2. \tag{1.6}$$

There is a maximum energy that can be radiated away in form of an electromagnetic waves given by the balance between the radiation pressure oriented outwards and the inward oriented gravitational pressure. The luminosity corresponding to this maximum energy a spherically symmetric black hole can emit in a steady spate is known as the Eddington luminosity $L_{\rm Edd}$ and is dependent on the black hole mass

$$L_{\rm Edd} = \frac{4\pi c G M_{\rm BH} m_{\rm p}}{\sigma_{\rm T}} \simeq 1.3 \times 10^{38} \left(\frac{M_{\rm BH}}{M\odot}\right) {\rm erg/s}, \tag{1.7}$$

where the constant $m_{\rm p}$ stands for proton mass, c is the speed of light and $\sigma_{\rm T}$ is the cross-section for Thompson scattering.

1.1.3 Corona

The short time scales of AGN variability in the X-ray band indicate that the size of the region where the X-rays are produced is very small. As the accretion discs in AGN do not reach the temperatures high enough to emit photons in the X-ray band, it is generally accepted that the inverse Compton scattering in a corona is responsible for the production of hard X-ray power law emission.

Corona is believed to be a region filled with hot ultra-relativistic electrons in close vicinity of the accretion disc and the black hole. Once the thermal optical-UV photons from the disc reach the corona, the energetic electrons scatter the low energy photons to high energies at the expense of their own kinetic energy. This process is often referred to as Comptonization or Compton up-scattering and is believed to be responsible for the isotropic emission of the hard X-ray photons in AGN. However, the origin, geometry and localization of corona is still a largely discussed problem with several different models proposed throughout the years (Bambi, 2017).

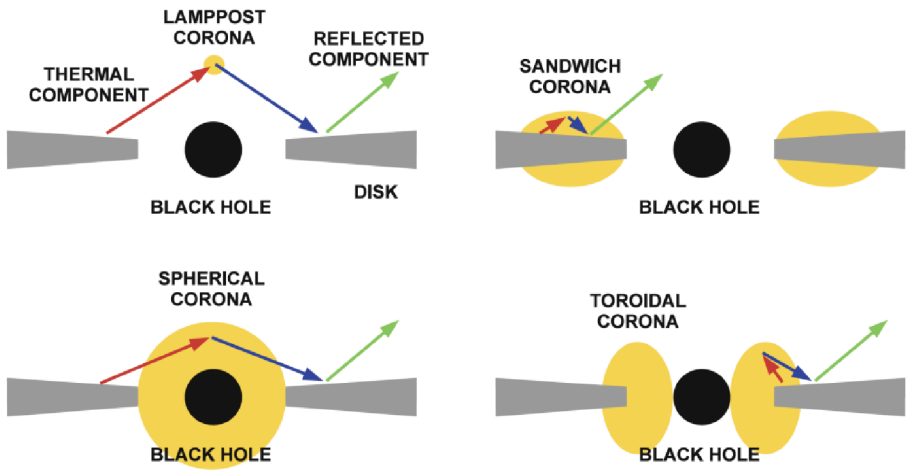

Figure 1.2: Figure adapted from Bambi, 2017 shows the different geometries of different coronal models.

1.1.4 Broad Line Region

There are several dominant features in the AGN spectra that can be used to characterize the regions in the close vicinity of the SMBH. One of such features are broad emission lines present in many AGN spectra easily probing the central engine. (Peterson, 1997).

The region where the broad spectral lines are believed to be produced is referred to as broad-line region (BLR) localized in close proximity of the central engine. The bulk motions of cloudlets of gas in the BLR are most certainly determined by the balance between the gravitational force and radiation pressure. As the widths of the emission lines can be at some sources reach very large full widths at half maximum intensity (FWHM), it is assumed that the broadening can not be produced purely by thermal motions, as this would suggest temperatures in the BLR much higher than expected. From the typical widths assuming purely thermal broadening a $T \gtrsim 10^9$ K would be indicated, but from the relative intensities of the lines the average gas temperature is expected to be $T \sim 10^4$ K. Due to this, the lines are believed to be Doppler-broadened with FWHM usually measured in velocity units, spanning between $\Delta v_{\mathrm{FWHM}} \approx 500$ km s^{-1} up to $\Delta v_{\mathrm{FWHM}} \gtrsim 10^4$ km s^{-1} with values typically around $\Delta v_{\mathrm{FWHM}} \gtrsim 5000$ km s^{-1}, indicating very large orbital velocities of the individual line emitting cloudlets in the BLR.

From the absence of broadened forbidden lines in spectra the lower limit for the electron density of BLR can be derived to be $n_{\mathrm{e}} > 10^8$ cm^{-3} (Netzer, 1990). Even though the forbidden lines are collisionally suppressed, allowing only permitted

atomic transitions, a semi-forbidden lines have been observed with the same equivalent width (EW) as permitted lines, suggesting the upper limit of electron density to be $n_e \lesssim 10^{11}$ cm^{-3}.

The average distance of the BLR from the central black hole varies from 0.01 parsecs up to 1 parsec for different types of active galaxies. The gaseous cloudlets reside deeply inside the strong gravitational potential of the SMBH and are dust-free, as the dust grains would be evaporates in such hot and dense environment. Whether the BLR is present in every AGN is still an open question, nevertheless its presence or absence in the observed spectra is used as one of the key elements in the optical line-of-sight dependent AGN classification.

1.1.5 Torus

The presence of a broadly asymmetric obscuring torus is required by the largely accepted unified scheme of AGN (see section 1.3). It spans at units of parsecs from the central region, absorbing the emission from the innermost regions of the AGN and re-emitting this radiation at longer wavelengths. The torus is generally believed to be formed by both gas and dust forming a smooth transition between the BLR and galactic-scaled interstellar environment. The dusty torus spanning from the sublimation radius is easily traced by high-resolution mid-infrared emission as it reprocesses the optical/UV radiation from the accretion disc.

The inner region of the circumnuclear torus is rather compact (< 1 pc). It is generally inhomogeneous in density, temperature and composition, as shown by high resolution infrared imaging Hickox & Alexander, 2018. The outer edge is believed to be the gravitational sphere of influence of the SMBH placing the clumpy torus within the gravitational influence of the central black hole. More details about the obscuring torus properties are in the section 1.4.

1.1.6 Narrow Line Region

Another characteristic spectral feature in the AGN spectra are narrow emission lines emitted in the so called narrow line region (NLR). Due to the presence of forbidden lines in the optical spectra that are not collisionally suppressed and remain narrow, the derived electron densities in the NLR must be $n_e \lesssim 10^5$ cm^{-3}. Permitted and forbidden spectral lines evince similar EW with typical values spanning in range $200 \lesssim \Delta v_{\rm FWHM} \lesssim 900$ km s^{-1}. Gaseous material in the NLR is orbiting the SMBH at much smaller velocities compared to the material in BLR and exhibits wide range of different ionization states. The low-density cloudlets in NLR are excited and partially ionized by photoionization as they are illuminated by the ultraviolet radiation from the inner regions of the accretion disc. Therefore the NLR is believed to be located within the so called ionization cone at much larger

distances from the central engine as the BLR, generally up to several hundreds of parsecs from the SMBH. In distant quasars the NLR can span up to few kiloparsecs, which makes it the most extended component of an AGN that can exceed the size of the host galaxy.

1.1.7 Jets

Jets belong to the large scale structure characteristics of active galaxies and are typical for radio-loud AGN (see section 1.3.1 about radio-loudness) as they are powering the extended radio lobes. These narrow linear features spanning from a few parsecs up to hundreds of kiloparsecs from the nuclei are aligned with the rotational axis of SMBH and are highly collimated. Jets emit mostly through non-thermal synchrotron radiation, from radio band up to energetic γ-rays. The dominant radio emission is often more symmetric on large kiloparsec scales with continuum appearance and rather asymmetric on small scales, presenting knots or blobs.

Jet formation is still largely discussed and not well understood problem. They are likely to form in the innermost regions of an AGN, within several gravitational radii r_{g} from the SMBH. Several formation scenarios have been proposed by R. Blandford, as described in Thorne et al., 1986. Kuraszkiewicz et al., 2021 found that the low-frequency radio emission from the extended radio lobes is largely independent of the orientation and therefore of the amount of obscuration by gas and dust present in the circumnuclear torus.

1.2 Spectral properties of AGN

Nuclei in the active galaxies rank among the most luminous objects in the Universe. Emission from the AGN components discussed in section 1.1 plays key role while building up its broadband spectral energy distribution (SED), that shows to be rather flat, as AGN are bright across the entire electromagnetic spectrum. In the first approximation, within a limited energy range, the AGN SED visualized in the figure 1.3 can be often described by a power-law

$$L_\nu \propto \nu^{-\alpha}, \tag{1.8}$$

where the value of the spectral index α ranges between 0 and 1 (Koratkar & Blaes, 1999).

Radio emission. The radio luminosity of an AGN can span across several orders of magnitude. This dichotomy is why we distinguish AGN between radio-loud and radio-quiet sources with the majority of AGN being radio-quiet

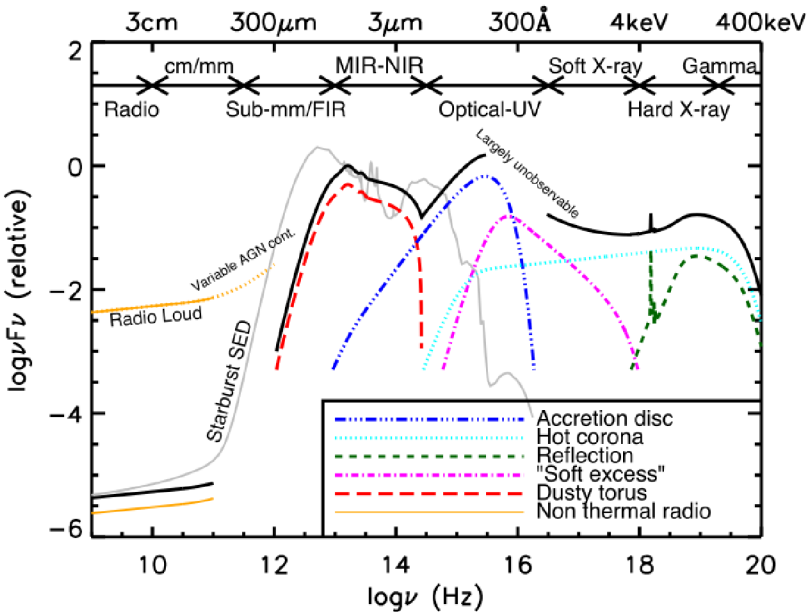

Figure 1.3: Spectral energy distribution of an AGN adapted from Hickox & Alexander, 2018.

with intermediate or weak radio emission, and only about 10% of AGN being radio-loud with powerful radio emission. The radio-loud sources are characterized by compact core and/or extended radio emitting regions, where the non-thermal synchrotron radiation mechanism is responsible for the strong radiation, as the charged particles are being accelerated in the jets. The radio core is believed to be the base of the jet formation, while the extended emission is due to the radio emitting lobes interacting with the galactic and extragalactic medium.

Infrared emission. As the accreting black holes are generally not intrinsically bright in the infrared (IR) band, most of the AGN IR emission comes as an emission reprocessed in the dusty environment around the SMBH. Due to the strong ionization radiation emerging from the nucleus, the dust can not survive in the close vicinity of the central engine, and forms only behind radius given by the sublimation temperature. The dusty torus than heats up by optical-UV light from the central engine up to several hundreds of Kelvins and radiates thermally with the emission peaking in the mid-infrared (MIR, $\sim 3 - 30\,\mu$m) band. Therefore, the most optically obscured AGN are bright MIR emitters and trace the dusty environments around nuclei. The MIR luminosity at $\sim 12\,\mu$m is also used by AGN Surveys such as LASr

(Asmus et al., 2020) as a selection criteria for AGN classification.

Optical-UV emission. The strong optical-UV AGN radiation has thermal origin in the accretion disc heated up to $T \sim 10^5$ K. The strong UV emission known as the *big blue bump* is one of the main characteristics of AGN spectra, peaking around 1050 Å (Huang et al., 2000), although gets easily obscured by the dusty torus and/or the dust in the host galaxy. The optical spectra of AGN are also often featured by strong emission lines emitted from both BLR and NLR (see setions 1.1.4 and 1.1.6 respectively).

1.2.1 X-ray emission

X-ray emission has been found to be one of the key features defining AGN, representing a significant fraction of its bolometric luminosity (typically $\sim$ 10% Peterson, 1997; Brightman et al., 2017). In the past few decades the X-ray domain has become one of the most crucial energy ranges for the AGN study, as the short time-scale variability indicates that the X-rays emerge from the very central regions of an AGN. The emission in this high-energy band can be separated into several components, discussed in this section and visualized in figure 1.4.

The primary component

The primary X-ray emission of an AGN is believed to be produced by inverse Compton scattering of low-energy photons on the energetic electrons in hot plasma. During this process the photons gain energy at the expense of the kinetic energy of the ultra-relativistic coronal electrons. The seed photons are supposed to be the thermal optical-UV photons originating particularly in the accretion disc. The Comptonization process produces the emission continuum spectrum described to the first order as a power-law, extending from the lowest X-ray energies (the soft X-ray band, $\sim 0.1 - 2$ keV), up to the cut-off energy typically in the the hard X-ray band ($\sim 2 - 100$ keV) or even in the γ-ray band up to ~ 300 keV. The high energy cut-off depends on the optical depth and the temperature of the electron distribution function in the corona. The higher temperature and larger optical depth, the harder power-law spectrum is obtained. The energy flux $F(E)$ as a function of energy can be given using the differential photon number density $N(E)$ as following,

$$N(E) = kE^{-\Gamma} \text{ photons s}^{-1} \text{ cm}^{-2} \text{ keV}^{-1} \tag{1.9}$$

$$F(E) = EN(E) = kE^{-\alpha} \text{ keV s}^{-1} \text{ cm}^{-2} \text{ keV}^{-1}, \tag{1.10}$$

with Γ being the photon index, the energy index α is given as $\alpha = \Gamma - 1$, and k is the normalization of the power-law at 1 keV. In order to represent the energy

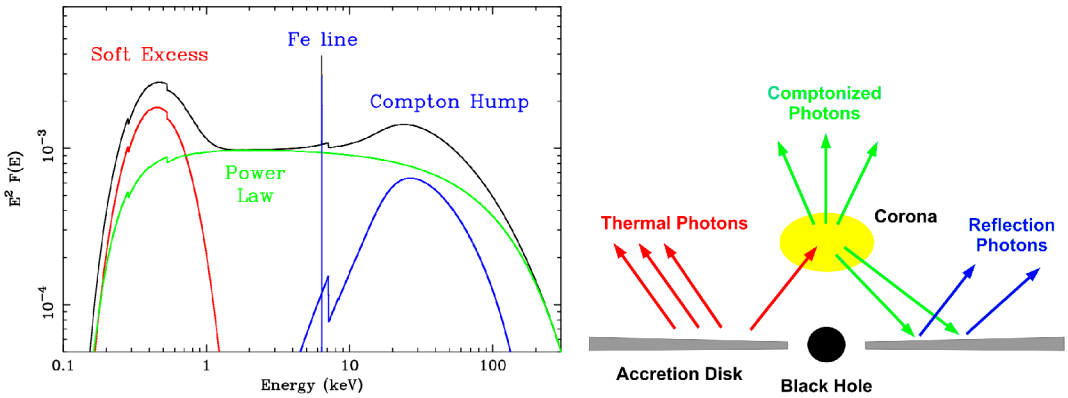

(a) X-ray spectral components of an AGN. (b) Central constituents of an AGN.

Figure 1.4: The main spectral components of the intrinsic X-ray emission are shown in (a) adapted from Fabian, 2006 with a visualization of the central regions of an AGN and the corresponding components labelled by the same colors in (b) from Bambi, 2021. The soft excess (*red*) is not necessarily connected to the thermal photons from the accretion disc as the thermal component in AGN dominates rather in the optical/UV band. The primary power-law component (*green*) is produced by Comptonization of the soft thermal photons from the disc in the hot corona. The reflection component (*blue*) is composed of the Compton hump and fluorescent emission Fe Kα line as the primary photons are reflected and absorbed with following fluorescent line emission in the dense gaseous disc.

at which the source peaks at, we usually plot $EF(E)$ versus E in the logarithmic space. In such plot we can distinguish between soft spectra, peaking in the soft band, characterized by photon index $\Gamma > 2$, the hard spectra peaking at the higher energies with $\Gamma < 2$ and flat spectra with $\Gamma = 2$.

The soft excess

In addition to the primary X-ray component, both obscured and unobscured AGN show an excess in the soft X-rays below $\sim 1 - 2$ keV Ricci et al., 2017b, even though this so called *soft excess* is believed to have a different physical origin in these two cases.

In obscured AGN the origin of the soft excess may account for the emission from a thermal plasma possibly related to star formation (Iwasawa et al., 2011), radiative-recombination continuum created by gas photoionized by the AGN (Bianchi et al., 2006; Guainazzi & Bianchi, 2007) or by scattering of the primary X-ray emission in Compton-thin circumnuclear material (Ueda et al., 2007). This spectral component in obscured objects is usually modelled by adding

a second cut-off power-law component with parameters fixed to the primary X-ray component.

Even though the physical origin of the soft excess is still largely debated, it is important to add an individual spectral component in modelling of X-ray spectra as it is present in significant fraction of both obscured and unobscured radio-quiet AGN. Additionally a component describing a collisionally ionized plasma is often added to the spectral modelling.

The reflection component

The primary emission produced by the Comptonization process on hot ultra-relativistic electrons can either escape towards the observer, of be reflected by cooler, Compton thick material in the close vicinity of the X-ray source. Generally the accretion disc is assumed to be the reflecting medium of the X-ray continuum radiation emerging from the hot corona. The reflection spectrum is determined by two energy dependent processes occuring in the reprocessor: the photoelectric absorption and Compton scattering. Photoelectric absorption is dominant for softer photons < 10 keV, while the Compton down-scattering on free electrons becomes dominant for higher energies > 10 keV. Therefore the typical Compton reflection component gives rise to so-called *Compton hump* peaking at ~ 30 keV with the lower edge cut-off at $\sim 4-5$ keV given by the photoelectric absorption of the lower energy incident radiation. The higher edge cut-off is due to smaller interaction cross-section, as more energetic photons penetrate at larger depths into the disc and are less scattered. The shape of the reflection spectrum is also dependent on the ionization state of the reprocessing material, as for higher ionization the photoelectric absorption has a lower influence on the re-emitted photons and the albedo below 10 keV increases.

The iron line

An important feature of the reflection spectrum is the iron emission line at 6.4 keV rest-frame energy for neutral iron. Photons with energies higher than the iron absorption edge with threshold energy of 7.1 keV are required for ejection of one of the two electrons in the iron K-shell ($n = 1$), providing the dominant source of opacity in the accretion discs. The iron atom excited by the photoelectric absorption can decay in two ways: the fluorescent line emission or Auger de-excitation. The fluorescence happens when an electron in L-shell ($n = 2$) de-excites into the K-shell emitting Fe Kα line photon at 6.4 keV (34% probability). The Kα fluorescence is made of two components, Kα1 at 6.404 keV and Kα2 at 6.391 keV, meaning the Kα line is a doublet. The line energy rises somewhat with increasing ionization states, 6.7 keV for He-like Fe and 6.9 keV for H-like Fe (Krolik, 1999). More probable

than the fluorescence is the ejection of an Auger electron once the L-shell electron de-excites into K shell (66% probability), even though with increasing ionization the fluorescent line emission is more likely to occur (up to 50% probability).

Among all the emission lines in the reprocessed spectrum the Fe lines are the strongest due to the relative iron abundance as well because the fluorescence yield is proportional to the forth power of the atomic number ($\propto Z^4$, $Z_{\rm Fe} = 26$). The Kα transition is the most probable although Kβ line at 7.06 keV, corresponding to transition from M-shell ($n = 3$) to the K-shell is also observable with $\sim 13.5\%$ of the Kα flux.

The narrow component of the Fe Kα fluorescence emission line peaking at 6.4 keV is in obscured AGN arising from cold neutral material in the torus (Ricci et al., 2014). Even though the EW is an indicator of higher column densities, it has been found that it inversely correlates with the X-ray luminosity of the underlying continuum in the $2-10$ keV band for transmission-dominated type 1 AGN (Iwasawa & Taniguchi, 1993). Evidence of this Iwasawa-Taniguchi effect for Compton-thick AGN was found by Ricci et al., 2014 and elaborated on further by Boorman et al., 2018. A possible physical scenarios responsible for this effect account for a luminosity dependent covering factor or ionization state of the reprocessor (Boorman et al., 2018). Regarding the luminosity of the line, it has been found that the Fe Kα line emission normalized to the emission of the underlying continuum is on average weaker for type 2 sources compared to type 1 AGN (Liu & Wang, 2010).

In reflection dominated X-ray spectra of AGN the Fe Kα line evinces a tail-like feature at its low-energy side. This so called *Compton shoulder* is generated via Compton down-scattering of the monochromatic line photons (Odaka et al., 2016). However, the observation and detailed study of the Compton shoulder requires a high-energy resolution X-ray spectroscopy since the shift is very small (Odaka et al., 2016).

1.3 AGN Classification and The Unified Model

The process of accretion of matter onto a SMBH as a source of energy feeding the extensive radiation across all wavebands is nowadays generally accepted. Despite the common principle powering the AGN they tend to differ in the observed characteristics. Generally the observed differences between individual AGN types can be caused due to orientation or the inclination angle respect to the line of sight to the observer and the geometry of the obscurer, time evolution, black hole mass and black hole spin, availability of fuel or the interaction with the ambient medium. The classification of AGN is based on different spectral properties across the full electromagnetic spectrum and thus necessarily different selection criteria as well.

Among commonly used classification methods in the optical band is a diagram constructed by Baldwin, Phillips and Terlevich (known as BPT diagram, Baldwin et al., 1981) showing the ratios of emission spectral lines and allowing us to distinguish non-active galaxies from AGN and starburst galaxies. More diagnostic methods involve the study of the radio characteristics or IR colors. Despite many selection methods across the electromagnetic spectrum one of the most reliable classification technique for detected sources is in the X-ray band due to the high energy radiation in AGN being ubiquitous.

1.3.1 Radio loudness

The nature of the radio emission from AGN is clarified in the section 1.2. Based on the strength of the radio emission in AGN, usually associated with the presence of a large-scale structures such as radio jets and lobes, we classify AGN into radio-quiet and radio-loud sources. Radio loudness is measured by parameter R,

$$R \equiv \frac{F_{\nu_{\mathrm{R}}}}{F_{4400\text{Å}}}, \tag{1.11}$$

where ν_{R} is the observed frequency in the radio band. The bimodality in the distribution of parameter R was discovered by Kellermann et al., 1989 and acquires values of $R \sim 0.1 - 1$ for the radio-quiet sources and $R \sim 10 - 1000$ for radio-loud sources, usually accepting $R \sim 10$ as a threshold (Ricci, 2011).

As already mentioned, the radio loudness is generally related to the presence of jets causing large anisotropy in the radio emission. The radio lobes are usually spanning up to several kiloparsecs from the central engine into the intergalactic medium and evince distinct morphological characteristics as described by Fanaroff & Riley, 1974. They divided radio-loud sources into two classes: weaker Faranoff-Riley class I (FR-I) are brighter in the center and fainter towards the edges of the lobes, and Fanaroff-Riley class II (FR-II) with faint core and dominant edge-brightened lobes with showing hot-spots at the outer edge. Due to relativistic boosting the jet receding from us is not always observable.

The radio dichotomy of AGN is still largely discussed problem. Proposed clarifications trying to explain the difference between radio-loud and radio-quiet AGN account for different black hole masses and/or different accretion mechanism.

1.3.2 Spectroscopic and photometric classification

A separate classification is based on the spectroscopic features mostly in the optical band. Two distinct classes of AGN are based on the presence of emission spectral lines emerging from the BLR, as these are not always present in the observed spectrum. Type 1 AGN are showing broad and narrow lines whether type 2 are

showing only the presence of narrow lines. The physics of the difference between type 1 and type 2 optical classification is most probably due to the orientation of the AGN towards the observer. In AGN with a dusty absorbing torus located in the orbital plane of the system, the emission from the BLR is obscured and therefore the broad lines are not observable. Figure 1.5 shows the comparison between the type 1 and type 2 AGN optical spectra.

Regarding the differences based on the photometry we can distinguish AGN based on the surface brightness in the optical images. Such as distant quasars are so bright that they can outshine their host galaxies so that they are unobservable, other types of AGN such as Seyfert galaxies have clearly distinguishable spiral host galaxies with comparably luminous nuclei. To clarify the physics behind the distinct AGN luminosity, we need to take into account the degree of central activity conditional on the black hole mass and the availability of fuel that can be accreted.

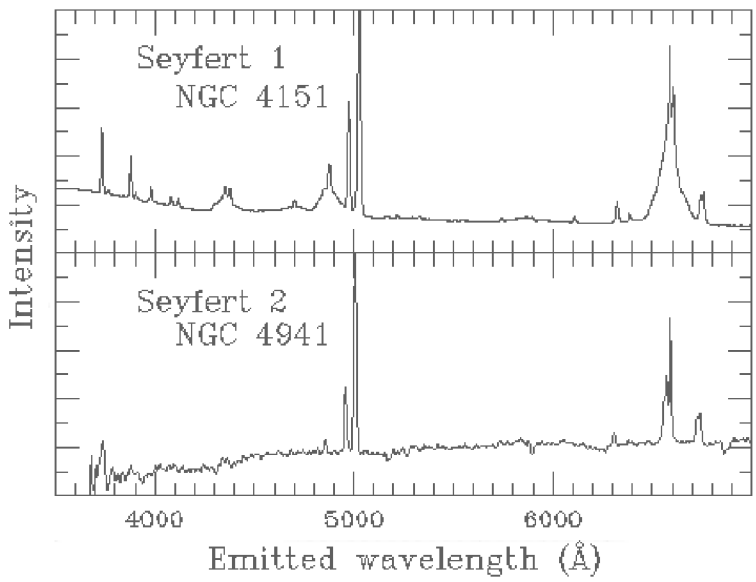

Figure 1.5: Optical spectra of two Seyfert galaxies NGC 4151 and NGC 4941 show the differences between the two classification types of AGN. Type 1 (NGC 4151) has both broad and narrow lines present, while type 2 (NGC 4941) evinces only narrow lines in the optical spectrum. The units on the y-axis are arbitrary, the wavelength is displayed in Angstroms Å. Adapted and modified from https://pages.astronomy.ua.edu/keel/agn/spectra.html.

1.3.3 The AGN family

Except of the radio galaxies divided into FR-I and FR-II, whose nature is described in section 1.3.1 we distinguish between the following AGN classes.

Quasars and QSO. Quasars belong among the most luminous AGN classes, with $\sim 5 - 10\%$ of sources being bright in the radio band, as the discovery of quasars occurred in the long wavelengths in late 1950s (QSR refers to *quasi-stellar radio source*). QSO is originally acronym for *quasi-stellar object* nowadays often referring to radio-quite quasars. Their host galaxies are outshined by the bright nuclei and are spatially unresolved, as quasars are typically star-like point sources found usually at higher redshifts. The broadband continuum emission of quasars as well as the spectral line profiles show to be highly variable with often unusually large flux in the UV band. Optical spectra are characterizable by strong emission lines with presence of broad line profiles.

Seyfert galaxies. Firstly described as a class of active galaxies by Seyfert, 1943. Seyferts are a lower-luminosity AGN with clearly detectable spiral host galaxies located in the local Universe. They evince strong emission lines based on which they are classified into two spectroscopic types, firstly discovered by Khachikian & Weedman, 1974. Type 1 Seyferts have two sets of emission lines, broad and narrow alongside, superposed on one another. In Seyfert type 2 only the narrow emission lines are present, as the BLR is obscured by the optically thick dusty torus. Additionally, an intermediate subclasses between type 1 and type 2 Seyferts were introduced by Osterbrock, 1981, based purely by the appearance of the optical emission-line spectrum.

Low Ionization Nuclear Emittion Regions (LINERs). LINERs are AGN with very low-ionization and low-luminosity nuclear regions identified by Heckman, 1980. They are characteristic by strong low-ionization narrow emission lines and spiral host galaxies. Spectroscopically LINERs resemble Seyfert 2 galaxies and are very common in the local Universe.

Blazars. The term blazars is used for the unification of so called Optically Violent Variables (OVV) and BL Lacertae (BL Lac) objects. Blazars are generally strong radio sources characterized by non-thermal and highly variable, relativistically beamed continuum emission. They are believed to be radio galaxies with their jet oriented in the line of sight towards the observer.

1.3.4 Unification

The unified model firstly proposed by Antonucci & Miller, 1985 and later developed by Antonucci, 1993; Urry & Padovani, 1995 is constructed in a way to show the AGN family in one single unified picture. The motivation for the unification scheme of AGN classes arises from the realization that projection effects might play a significant role in determining the observed AGN properties. In case of a dusty torus or a relativistically beamed jet present in the AGN a different inclination angle leads to distinct observed features and therefore change of orientation partially explains the existence of the AGN zoo.

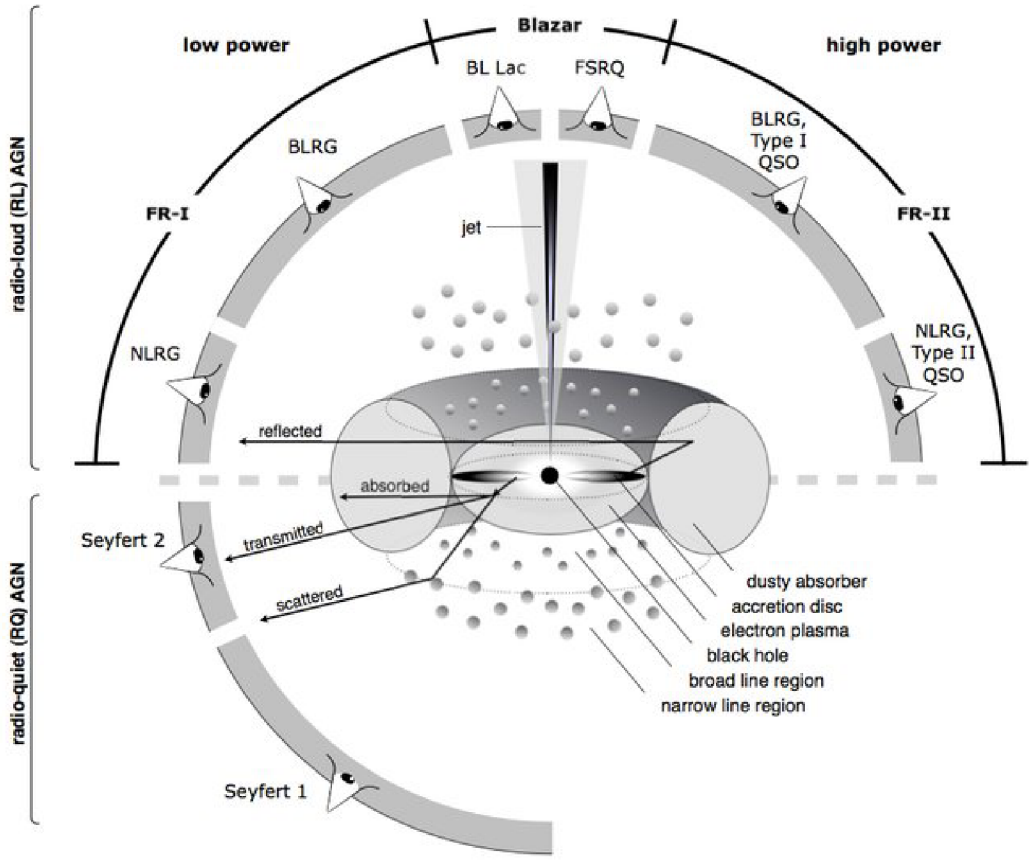

Figure 1.6: The unification scheme of AGN from Beckmann & Shrader, 2012

.

1.4 Obscured AGN

The very central parts of an AGN may be hidden by thick layer of gas and dust, that absorbs the emission from the vicinity of the SMBH and reproduces it at longer wavelengths. In general, the obscuration can happen anywhere along the line of sight between the central engine and observer. For majority of the obscured AGN the absorbing material is located in a torus within the gravitational influence of the central SMBH, but it can come from the host galaxy as well (Buchner et al., 2017; Buchner & Bauer, 2017). The active galaxies with nuclei obscured by the host galaxy tend to be observed rather inclined and edge-on with the absorbing material usually present in the dusty star-forming regions and interstellar clouds within the galactic plane. In the following sections only circum-nuclear obscuration in the vicinity of the central black hole will be discussed.

The zeroth order unified model (see section 1.3.4) suggests that the obscuration is mostly based on the inclination angle i (measured from the polar axis) as the distribution of the dense absorbing material is expected to be located mostly in the orbital plane of the system (Antonucci, 1993). Therefore the most obscured systems are usually seen under higher inclination angles. Besides that, the impact of the dense obscuring material on the detection of the nuclear emission depends heavily on the wavelength of the radiation. This is given by the optical depth τ_ν varying with the opacity χ_ν, mass density ρ of the material and the path length s (Rybicki & Lightman, 1979). The optical depth is defined as

$$\mathrm{d}\tau_\nu = -\rho\chi_\nu \,\mathrm{d}s. \tag{1.12}$$

As a consequence of the opacity being dependent on the frequency of the radiation ν, dust becomes the dominant source of the obscuration of the longer wavelengths in the UV to optical band whereas gas dominates the absorption in X-rays. The multi-wavelength constrains on the AGN obscurer geometry are visualized on figure 1.7.

In the optical waveband we distinguish between type 1 and type 2 AGN based on the presence of broad line region (BLR) in the optical spectrum, tracing the dusty environment in the line of sight. Sometimes the type 2 AGN class refers to obscured AGN in general, not limited to any energy band (Hickox & Alexander, 2018). Similarly in X-rays the obscuration classification is line of sight and geometry dependent and is based on the column density of neutral hydrogen of the obscuring circum-nuclear material around the SMBH (N_H [particles/cm^2]). We classify AGN into unobscured and obscured sources in the following way

unobscured AGN	$N_\mathrm{H} < 10^{22}$ cm^{-2}	Compton-thin	$N_\mathrm{H} \cong 10^{22} - 10^{24}$ cm^{-2}
obscured AGN	$N_\mathrm{H} \geqslant 10^{22}$ cm^{-2}	Compton-thick	$N_\mathrm{H} \geqslant 10^{24}$ cm^{-2}

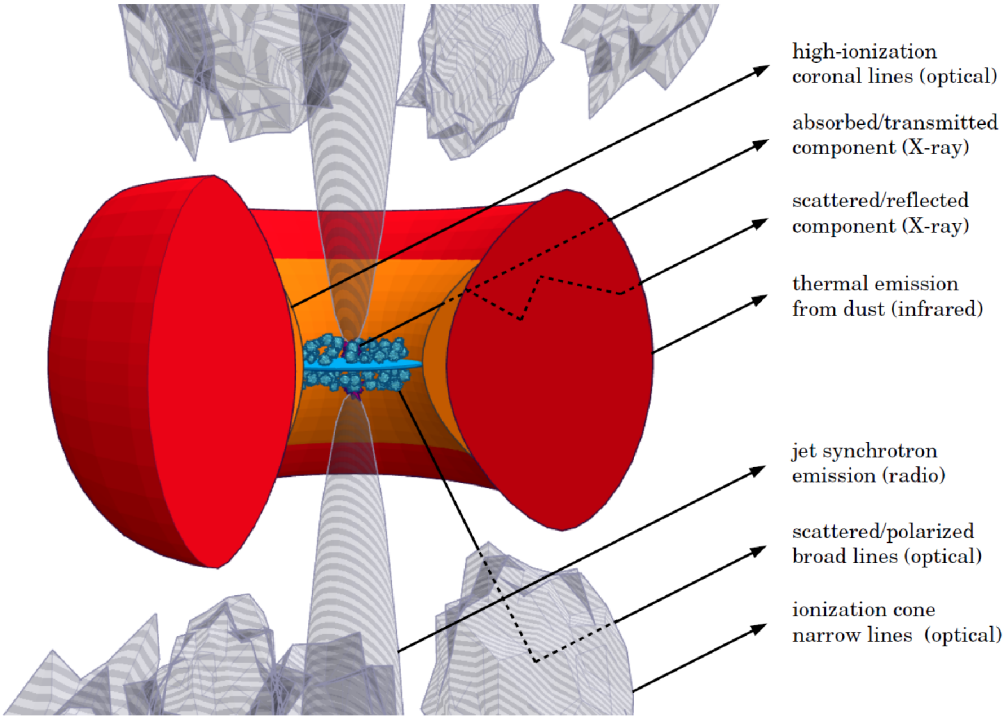

Figure 1.7: A visualization of a multi-wavelength spectral components of an radio-loud quasar IRAS 09104+4109 deeply buried in the optically-thick reprocessing material. The sketch is made by M. Baloković in the framework of the classical unified model of AGN. Adapted from Farrah et al., 2016. A more realistic distribution for the dust as a IR to radio emitter is in Hönig, 2019.

Furthermore we divide obscured AGN in Compthon-thin (CTN) sources with $N_{\rm H} \cong 10^{22} - 10^{24}$ cm^{-2}, and Compthon-thick (CTK) or heavily obscured sources, if $N_{\rm H} \geqslant 10^{24}$ cm^{-2}. In the following sections the AGN obscuration refers primarily to the absorption in X-ray band.

Spectral characteristics

Spectra of X-ray heavily obscured AGN are usually dominated by the reflection component as most of the primary emission can not be detected directly but only in its reprocessed form. For column densities $N_{\rm H} > 10^{25}$ cm^{-2} the direct emission can be no longer detected and the only detectable emission is the reprocessed one, as the photons are down scattered and below 10 keV absorbed in the cold gaseous torus. The ionization state of the relatively cold material here plays an important role in the absorption, even though the most obscured AGN can be assumed to be

neutral. The position of the Fe Kα line at 6.4 keV is a sign of a low-ionization state of the environment where the line is produced, as it shifts towards higher energies for higher ionizations (see the iron line description in section 1.2.1). Generally, the equivalent width of spectral lines increases with column density as it is measured against the absorbed continuum. For unobscured and CTN sources with column densities $N_{\rm H} < 10^{23}$ cm^{-2} the typical EW of Fe Kα is about 100 eV while its equivalent width can reach a few keV for the most obscured AGN. Intrinsically the Kα line is rather narrow, most probably produced in regions further away from the source of the primary emission in the cold gaseous torus, the BLR or an intermediate medium between the two (Ramos Almeida & Ricci, 2017).

Obscuring torus properties

The obscuring torus properties has become a focus of many X-ray obscured AGN studies in the past few years. It shapes and reprocesses the primary radiation into the emission that we detect by X-ray observatories, therefore the torus characteristics can be derived from broadband X-ray spectroscopy. Nevertheless the spectral resolution in the high energy bands is highly limited by the present X-ray detectors and the relatively small count rates of high energy photons. Despite that the X-ray band is essential in identifying heavily obscured AGN due to the requirement to constrain the absorbing column density (Hickox & Alexander, 2018). As the soft X-rays are suppressed and the direct emission is highly scattered in the line of sight, the broad spectrum gains a typical spectral shape of reprocessed light dependent on the torus geometry. As mentioned above, the most important parameter is the column density of neutral hydrogen $N_{\rm H}$ corresponding to the equivalent number of hydrogen atoms per unit cm^2 integrated along the line-of-sight column between the observer and the source. Even though the composition and ionization of the matter can change from source to source, for simplification in the torus models all the matter is approximated as neutral hydrogen. Increasing column density suppresses the detection of the primary emission.

The obscuring toroidal structure is often described as axis-symmetric as predicted by the unified model. This idea is supported the narrow Fe Kα line, produced in the torus or its immediate surrounding regions, being generally weaker in type 2 AGN compared to the type 1 sources (Ramos Almeida & Ricci, 2017). The inner region of the obscuring circumnuclear torus is rather compact with radius $\lesssim 1$ pc while the outer edge is naturally given by the gravitational sphere of influence of the SMBH, with radius typically ~ 10 pc (Hickox & Alexander, 2018) but can extend much further (García-Burillo, S. et al., 2021). The inner radius of the dusty material is given by the sublimation edge which is traceable by the high-resolution MIR observations and could be considered as the transition between the BLR and the torus. Nevertheless this transition and the structure of both BLR and the

obscuring torus is still a highly debated topic. As suggested by Gaskell et al., 2007, the BLR may form the inner part of the torus with both having similar geometries.

Theoretical studies predict that the structure of the dusty torus is in general clumpy (Krolik & Begelman, 1988; Rowan-Robinson, 1995; Nenkova et al., 2008a; Nenkova et al., 2008b) and high resolution MIR imaging is in agreement with this statement (Elitzur & Shlosman, 2006; Mor et al., 2009). The inhomogeneities can be found in both density, temperature and composition of the material. The clumpy structures are generally not static and exists in a complex environment of inflows and outflows (Hickox & Alexander, 2018). The movement of the optically-thick clouds illuminated from the central source of radiation gives rise to the obscuration variability, as the line of sight column density necessarily chances.

A key parameter describing the geometry of the obscuring circumnuclear material is the covering factor $C_{\mathrm{F,tor}}$ corresponding to the cosine of the opening angle $C_{\mathrm{F,tor}} = \cos\phi_{\mathrm{tor}}$. Covering factor represents the amount of sky as seen from the SMBH covered by the obscuring optically-thick material and can in principle be obtained from detailed modelling of X-ray spectrum Brightman & Nandra, 2011a. Therefore for higher covering factors it is statistically more likely for a source to appear as obscured, as a large amount of sky as seen from the central black hole is covered by dust. It has been found by many studies that the fraction of obscured sources decreases with the intrinsic AGN luminosity. This might indicate that for more luminous AGN the higher radiation pressure blows away the obscuring material, resulting in increasing opening angle and decreasing the covering factor. This scenario was proposed by Lawrence, 1991 and is referred to as the *receding torus model*. However, a recent studies (Stalevski et al., 2016; Mateos et al., 2017) indicate a much weaker covering factor - luminosity dependence, with the obscured AGN fraction remaining around 50% even for the most luminous AGN. This implies that with increasing luminosity the inner radius of the torus increases along with the sublimation edge, but the covering factor remains broadly constant. On the other hand it has been proposed that the actual parameter driving the evolution of the covering factor is the Eddington ratio $f_{\mathrm{Edd}} = L/L_{\mathrm{Edd}}$, where L_{Edd} is the Eddington luminosity, defined in the section 2.3.4. Ricci et al., 2017c showed that the hard X-ray luminosity dependence of the covering factor disappears when assuming different intervals of f_{Edd}. The strong relation between obscuration and the Eddington radio suggests that most of the obscuring material is indeed located in the toroidal structure within the gravitational sphere of influence of the SMBH (Hickox & Alexander, 2018).

Redshift dependency

Similarly, an increase in the obscured AGN fraction with redshift has been observed and studied by Ueda et al., 2014; Brightman et al., 2014; Buchner et al., 2015.

Relation of obscuration with redshift could indicate the increasing amount of gas in the high-z galaxies as well as with massive starburst activity that was more usual in the early Universe. The nuclear starbursts can lead to CTN obscuration on larger scales from the central engine (> 10 pc) and therefore significantly contribute to the obscured AGN population. The redshift dependency is also linked to the galaxy mergers that are more common at higher redshifts, as galaxies undergoing a late stage merger tend to exhibit CTK obscuration (Ricci et al., 2017a). However, the obscuration dependency on redshift is much weaker than the one with the Eddington luminosity ratio.

Obscured AGN fraction

The identification of obscured AGN has many implications in astrophysics, first of all in observational cosmology, but due to the heavy absorption they are not easy to find. The obscured and essentially CTK AGN fraction is still a matter of debate. Matt et al., 2000 assumes that obscured ($N_{\rm N} > 10^{23}$ cm^{-2}) Seyferts outnumber the unobscured ones by about an order of magnitude. Buchner et al., 2015 found that CTK AGN account for 38 % and obscured sources for 77 % of the number density of the AGN population averaged over the cosmic time. On the other hand Aird et al., 2015 found only $\sim$ 11 % of CTK AGN in the local Universe. Among the latest studies, with the new population synthesis model calculated using neural network Ananna et al., 2019 predicts 56% of AGN within $z \simeq 1.0$ to be Compton-thick. Even though the obscured AGN fraction estimates vary dramatically, heavily obscured accretion in galactic nuclei most likely plays a significant role in the history of the evolution of active galaxies and SMBHs.

Supermassive black hole growth

The complete consensus of AGN activity involving the both obscured and unobscured AGN identification is required in order to understand the history of the SMBH growth and galaxy formation. The question of black hole growth and its co-evolution with the host galaxy formation has been to a large extend one of the most studied problems in extragalactic astrophysics. Obscured AGN play an important role in disentangling the SMBH-galaxy mutual relationship, as the most rapid black hole growth occurs in systems deeply buried in layers of gas and dust with sufficient amount of fuel (Blecha et al., 2017). This precipitous phase of galaxy and SMBH growth may be triggered by galaxy mergers, interactions or violent instabilities (Hickox & Alexander, 2018). Ricci et al., 2017a showed that late stage galaxy mergers evince significantly higher obscuration of the nuclei by dust and gas that galaxies that are not undergoing an merger.

Missing AGN population

As mentioned above, the AGN obscuration shows enhancement at higher redshifts, even though this kind of obscuration might be rather connected to the gas content in the host galaxy (Carilli & Walter, 2013). Dedicated studies (Stern et al., 2014; Del Moro et al., 2016) showed that powerful distant ($z > 2$) quasars bright in the MIR band usually evince very weak detection in X-rays or remain undetected even in deep observations. Lower-luminosity AGN at higher redshifts are even more difficult to detect. The problem of *missing* AGN lies in insufficient amount of X-ray detected SMBH seeds at higher redshifts in order to produce the observed massive quasars at lower redshifts. The solution proposed by multiple population synthesis models of AGN predict a large fraction of accreting black holes to grow behind thick layers of gas and dust allowing the presence of many more growing SMBH below the detection thresholds (Novak, 2013).

Cosmic X-ray background

Perhaps the most reliable evidence predicting a large fraction of heavily obscured AGN in the Universe comes from the synthesis models of the cosmic X-ray background (hereafter CXB). The spectrum of CXB showed in figure 1.8 with shape of a broad hump is for the most part formed by integration of individual AGN spectra over cosmic time (Hickox & Markevitch, 2006; Brandt & Alexander, 2015). In the soft X-ray band around 80 % of CXB has already been resolved into discrete sources, while in the hard band > 10 keV a significant fraction of CXB still remains unresolved. Nevertheless, in order to successfully reproduce the prominent peak at ~ 30 keV, a large fraction of obscured AGN is needed (Gilli et al., 2007; Treister et al., 2009; Ballantyne et al., 2011; Akylas et al., 2012; Ueda et al., 2014; Aird et al., 2015). Even though many studies are in agreement with the necessity of significant fraction of CTK AGN in order to acceptably reproduce the CXB spectrum, they diverge in their estimates.

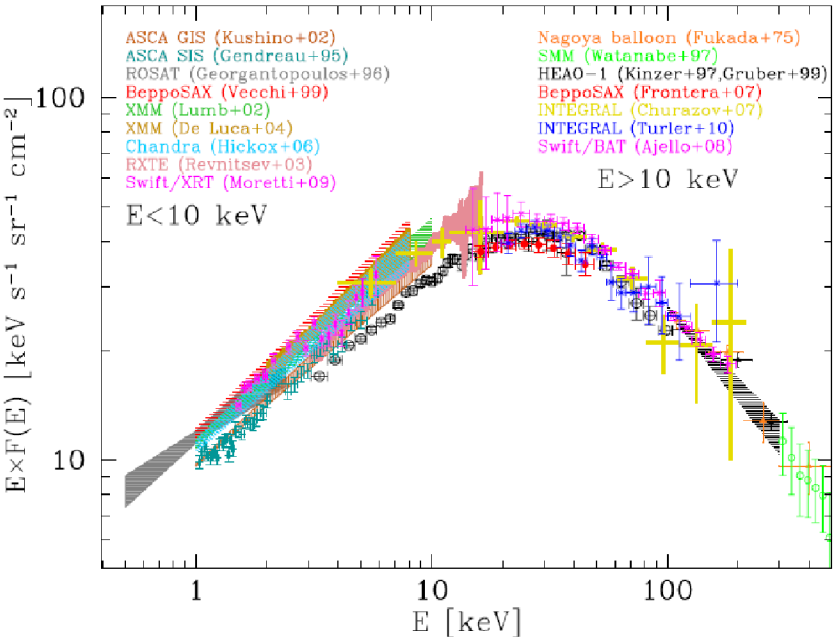

Figure 1.8: Spectrum of the Cosmic X-ray background adapted from Gilli, 2013.

2 Methodology

2.1 XMM-Newton observatory

The European Space Agency's (ESA) X-ray Multi-Mirror Mission (*XMM-Newton*) is a X-ray observatory orbiting Earth since December 10th 1999 when it was launched by Ariane 504. It is a high throughput X-ray spectroscopy mission with great capability to detect X-rays due to its sensitive detectors. It carries three co-aligned X-ray telescopes with 7.5 meter focal length, one optical monitor and two star-trackers. There are two reflection grating spectrometer readout cameras and three European Photon Imaging Cameras (EPIC), one EPIC PN and two EPIC MOS detectors located in the focal planes of the telescopes. Each EPIC MOS detector consists of an array of 7 CCDs which are made up of a matrix of 600×600 pixels, and EPIC-PN detector consists of an array of 12 CCDs made up of a matrix of 64×600 pixels. The bandpass of each detector is $0.15 - 12$ keV and their spectral resolution reaches ~70 eV and ~80 eV at 1 keV for MOS and PN detectors, respectively. The angular resolution reaches 6 arcsec FWHM and 15 arcsec HPD. The visualization of the *XMM-Newton* components is in the figure 2.1.

The Science Analysis Software (SAS, Gabriel et al., 2004) package was used for the *XMM-Newton* data reduction in order to reprocess the raw Observation Data Files (ODFs) and to generate calibrated and concatenated EPIC event lists. The EPIC event lists were consequently filtered for flaring particle background and finally scientific products such as X-ray images and source and background spectra were extracted for further spectral analysis. Binning of obtained spectra was achieved by using the `ftgrouppha` tool as described in section 2.3.2. The Current Calibration Files (CCF) were obtained from the CCF repositories.

[1] At https://www.cosmos.esa.int/web/xmm-newton/technical-details-spacecraft.

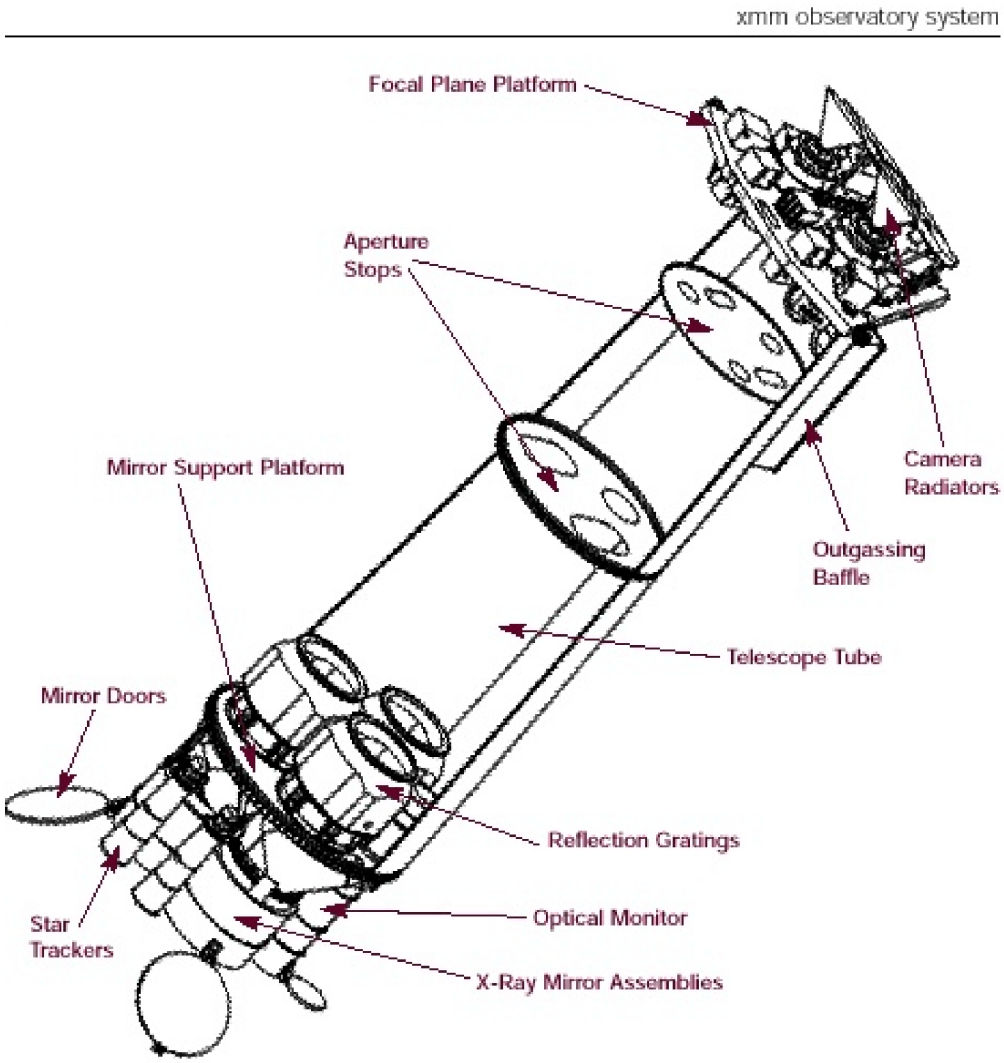

Figure 2.1: The schematic adapted from the ESA web page[1] shows the main four components of the *XMM-Newton* spacecraft: the focal plane assembly carrying the focal plane platform with the scientific instruments and the data handling and power distribution units for the cameras; the telescope tube composed of the upper and lower tube, while the upper tube includes two reversible venting and outgassing doors and supports the outgassing baffle; the mirror support platform carrying the three mirrors assemblies, the optical monitor and two star-trackers and the service module carrying the spacecraft subsystems and two solar-array wings, the Sun shield and two antennas.

2.2 NuSTAR observatory

The Nuclear Spectroscopic Telescope Array (*NuSTAR*) is the very first mission by the National Aeronautics and Space Administration (NASA) agency that had deployed a focusing telescope in the hight energy X-ray region (3 – 79 keV) of the electromagnetic spectrum. It was launched on June 13, 2012 by Pegasus XL Rocket to a low-Earth, near-equatorial orbit. The *NuSTAR* observatory consists of two co-aligned grazing incidence telescopes implementing a conical approximation to the Wolter-1 design (Harrison et al., 2013) of the X-ray optics with focal length of 10 meters. The optics consists of 133 concentric mirror shells coated with depth-graded multilayers in order to achieve a enhanced reflectivity up to 79 keV. There are two detector units located in the focal length of both telescopes, each comprised of four Cadmium-Zinc-Telluride (CZT) detectors. Each detector is gridded into 32 × 32 pixels and has energy resolution of 400 eV at 10 keV. The angular resolution of each telescope reaches 18 arcsec FWHM and 58 arcsec HPD. The focal plane with the detectors is separated from the X-ray optics by a unique 10 meter long deployable mast. Figure 2.2 shows a schematic of the *NuSTAR* telescopes.

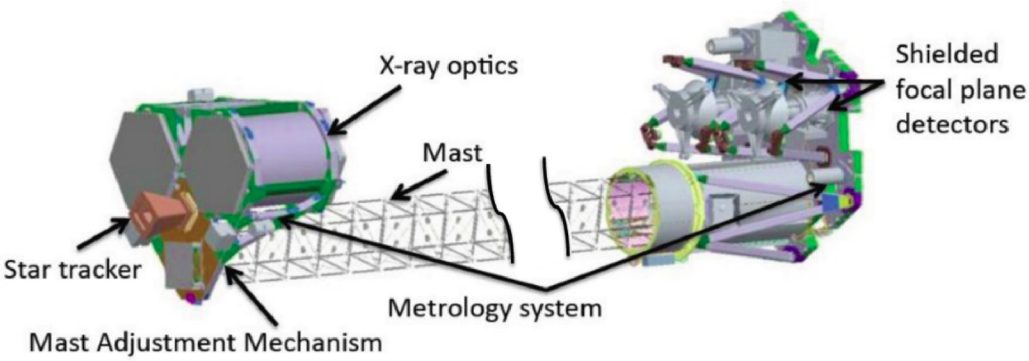

Figure 2.2: A design of the *NuSTAR* telescopes with two X-ray telescopes and a star tracker separated by a 10 meter long deployable mast (not to scale) from the focal plane detectors. Adapted from the *NuSTAR* observatory guide[2].

For the *NuSTAR* data reduction the NuSTARDAS software package was used, integrated and compatible with the HEASoft software package, in order to to produce cleaned and calibrated event list files and high-level scientific products from the FITS telemetry data. The data processing was done within three steps:

[2]Available online at https://heasarc.gsfc.nasa.gov/docs/nustar/NuSTAR_observatory_guide-v1.0.pdf.

calibration of the event files, the data screening corresponding to filtering of the calibrated event files and the extraction of the high-level scientific products such as sky images and energy spectra from cleaned event files. The calibration files are set via the Calibration Database (CALDB) of the High Energy Astrophysics Science Archive Research Center (HEASARC) retrieved by the software. The same binning was applied as for the *XMM-Newton* data.

2.3 X-ray spectral analysis

The photon count rate as a function of specific instrument channels $C(I)$ detected and measured by spectrometer can be given by the integration of the product of the actual spectrum of the source $f(E)$ and the instrumental response $R(I, E)$ giving the probability of an incoming photon of energy E detection in channel I (Arnaud et al., 2020).

$$C(I) = \int f(E)R(I, E)\mathrm{d}E. \tag{2.1}$$

To obtain the actual source spectrum, a model spectrum defined by complex set of parameters $f(E, p_1, p_2...)$ is used and predicted photon count rate $C_p(I)$ is calculated and subsequently compared to the observed data $C(I)$. This process of fitting the model to the data allows us to find the best-fit model parameters based on the fit statistic.

One of the most reliable classification methods for obscured AGN is to measure the column density by broadband X-ray modelling. To derive the posterior values for complex set of parameters defined by spectral models the Xspec X-ray spectral fitting package was used (Arnaud, 1996). The algorithm used by Xspec for minimizing the fit statistic is the Levenberg-Marquardt (Levenberg, 1944; Marquardt, 1963) algorithm described in Bevington, 1969. Due to the parameter estimation algorithm being rather local than global, one needs to pay attention so the fitting process would not get stuck in a local minimum.

2.3.1 C-statistic

There are two operations performed by the fitting package where the fit statistic is required, the parameter estimation for a given model and the parameter uncertainty estimation. Due to low luminosity of the studied source and limited number of counts per bin the Poisson based likelihood statistic was used. Using W statistic (Wachter et al., 1979 in Xspec labelled as `cstat`, which is a modified C statistic), we model the background spectrum simultaneously together with the source spectrum. The parameter estimation is derived using the maximum likelihood L with

the following definition for data with Poisson distribution (derived by Cash, 1979),

$$L = \prod_{i=1}^{N} \frac{(tm_i)^{S_i} e^{-tm_i}}{S_i!}. \tag{2.2}$$

Here the S_i are the observed counts in the exposure time t and m_i are the predicted count rates based on the current model and instrumental response. The maximum likelihood-based statistic for Poisson data C is given by

$$C = 2 \sum_{i=1}^{N} (tm_i) - S_i \ln(tm_i) + \ln(S_i!), \tag{2.3}$$

which can be overwritten in the following way using Stirling's formula

$$C = 2 \sum_{i=1}^{N} (tm_i) - S_i + S_i(\ln(S_i) - \ln(tm_i)). \tag{2.4}$$

The W statistic usually gives unbiased results for cases with large number of counts per bin but can generate a wrong best-fit for weak sources with a little or zero counts in the background spectrum. Such limitation can be solved by binning the data according to the background spectrum in a way, so every bin would contain enough counts. If the C-statistic accounting for the Poisson distribution is used for data with large number of counts it can be well approximated by the Gaussian distribution (or the χ^2) that is often used for detectors with hight counting rates. The χ^2 is often applied as an alternative to Poisson statistic with assumption that the data follow the Gaussian distribution. In most cases for X-ray data this is not fulfilled and in order to avoid biases and loss of information the Poisson distribution should be applied instead (Siemiginowska et al., 2011).

2.3.2 Binning methods

As the studied source is a low luminosity AGN with low count rate, the following binning was applied to the spectra. In order to set a minimum number of counts in each bin in the background file the `ftgrouppha` tool was applied. The tool provides several grouping type options, the most relevant are listed below.

bmin This grouping option allows us to bin the source spectrum so that there is defined a minimum number of counts per each bin in the background spectrum. The `groupscale` parameter is used to set the minimum number of counts per bin.

opt The binning is based on binning scheme by Kaastra & Bleeker, 2016.

constant A uniform binning by a factor given by the `groupscale` parameter.

Unless stated otherwise, the binning method applied to data in this work is the `bmin` with the `groupscale` parameter equal to 1 count per background bin, after XSPEC re-bins the background to match the source spectrum.

2.3.3 Spectral models

To model the broad X-ray spectra of the studied AGN, we use various spectral models all build up on different assumptions. In order to be able to compare this work with other works performed in the past decades, we apply a phenomenological model `pexrav` build in the XSPEC environment. Subsequent analysis is done using physically motivated table models presented by several different works in the past years. All empirically motivated spectral models are based on different and unique torus geometries and build on Monte Carlo radiative transfer simulation codes.

The Monte Carlo radiative transfer codes are based on tracking the individual simulated photons interacting with the matter. This approach allows us to calculate the output spectrum as expected from the Monte Carlo Radiative Transfer simulations of the circum-nuclear environment with complex matter distribution. At first, there is a X-ray generator producing the photons with desired energy distribution. Subsequently the photons are traced as they interact with the matter through the user-defined physical processes, until the photons die or exit the system. The photon participates in randomly selected physical process, for most of the models accounting for photoelectric absorption or Compton scattering, with probability proportional to the cross-section of the selected process at the current photon energy. In the case of absorption there is a chance of consecutive fluorescent photon emission with probability as described in section 1.2.1. The description of the surrounding reprocessing material is based on its geometrical shape, composition and hydrogen density. The output is made of the photon energy, location and direction of the escaped photons that produce the result spectrum.

The following spectral components are used to build up a complex broadband model set-ups used in this work.

apec This model component gives an emission spectrum from collisionally-ionized diffuse gas calculated using the APEC (Astrophysical Plasma Emission Code) from the AtomDB atomic database[3]. The parameters of the `apec` model component are: plasma temperature in keV; metal abundances set by the `abund` command, with the He abundance fixed at cosmic; redshift z and normalization K given as following

[3] www.atomdb.org

$$K = \frac{10^{-14}}{4\pi[D_{\rm A}(1+z)]^2} \int n_e n_{\rm H} {\rm d}V, \tag{2.5}$$

where $D_{\rm A}$ is the angular size distance to the source in cm, n_e in the electron density and $n_{\rm H}$ the hydrogen density both in cm^{-3}.

cabs The `cabs` model component gives the optically-thin non-relativistic Compton scattering with defined neutral hydrogen column density $N_{\rm H}$ in units of 10^{22} cm^{-2},

$$M(E) = \exp\left[-N_{\rm H}\,\sigma_{\rm T}(E)\right]. \tag{2.6}$$

where $\sigma_{\rm T}(E)$ is the Thomson cross-section allowing the Klein-Nishina approximation for high energies (Liu & Li, 2014).

phabs A model component giving the photoelectric absorption with the photoelectric cross-section $\sigma(E)$ that does not include Thomson cross-section. The $N_{\rm H}$ is again the hydrogen column density in units of 10^{22} cm^{-2}.

$$M(E) = \exp\left[-N_{\rm H}\,\sigma(E)\right] \tag{2.7}$$

zphabs A redshifted variant of the `phabs` model component.

tbabs As the observed target is and extragalactic object, the correction for the X-ray absorption by the interstellar medium (ISM) of our Galaxy is done by the Tübingen-Boulder ISM absorption model by (Wilms et al., 2000). The `tbabs` model calculates the cross-section $\sigma_{\rm ISM}$ for X-ray absorption by the gas, gains and molecules in the ISM of our Galaxy. In our set-up only the hydrogen abundances are taken into account. The total hydrogen column density $N_{\rm H}$ refers to hydrogen in molecular, neutral or ionized form.

$$M(E) = \exp\left[-N_{\rm H}\,\sigma_{\rm ISM}(E)\right] \tag{2.8}$$

ztbabs The modified Tübingen-Boulder ISM absorption model allowing the user to define the redshift z.

constant A simple `factor` multiplying the following spectral components.

cutoffpl A power law model with exponential high-energy cut-off given by the formula

$$M(E) = KE^{-\alpha} \exp\left(-\frac{E}{\beta}\right), \tag{2.9}$$

where α is the photon index, β is the e-folding cut-off energy and K is the normalization given in photons per keV/cm^2/s at 1 keV.

zpowerlw A power law model component with redshift z as a fixed parameter.

$$M(E) = K\,[E(1+z)]^{-\alpha}\,. \tag{2.10}$$

zgauss A redshifted Gaussian line profile given by the following formula

$$M(E) = K\frac{1}{(1+z)\,\sigma\,\sqrt{2\pi}} \exp\left[-\frac{[E(1+z)-E_{\mathrm{L}}]^2}{2\sigma^2}\right] \tag{2.11}$$

where E_{L} is the source frame line energy in keV, σ is the source frame line width in keV with redshift z and normalization K corresponding to total number of photons per cm^2/s in the line. For the line width $\sigma \leq 0$ it is treated as a delta function.

gsmooth A velocity broadening of an fluorescent emission lines is implemented with a `gsmooth` function corresponding to Gaussian smoothing with a variable width $\Sigma(E)$. The Gaussian width of the line at 6 keV σ is set by the first parameter while the second parameter α gives the power of energy for the sigma variation.

$$\begin{aligned} \Sigma(E) &= \sigma(E/6)^{\alpha}, \\ \mathrm{d}C(E) &= \frac{1}{\sqrt{2\pi\,\Sigma(E)^2}} \exp\left[-\frac{1}{2}\left(\frac{E-X}{\Sigma(E)}\right)^2\right] A(X)\mathrm{d}X. \end{aligned} \tag{2.12}$$

This model component is required in the MYTorus table model set-up.

The following reflection models were applied to the broadband X-ray spectrum of the studied obscured AGN.

PEXRAV

The phenomenological model `pexrav` (Magdziarz & Zdziarski, 1995) is based on exponentially cut-off power-law spectrum reflected from a neutral reprocessing material. The output spectrum is a sum of the primary X-ray emission following a power-law with an exponential high energy cut-off and the reprocessed reflection component. Pexrav was computed using analytical approximations of the Green's

functions derived from Monte Carlo simulations. It assumes that the reflector is a strictly optically-thick medium located in an semi-infinite plane geometry with the source of the primary emission located immediately on the top of the reflector (see figure 2.3). The implemented physical processes account for the photoelectric absorption and Compton scattering (Paltani & Ricci, 2017) with assumption of fully ionized hydrogen and helium.

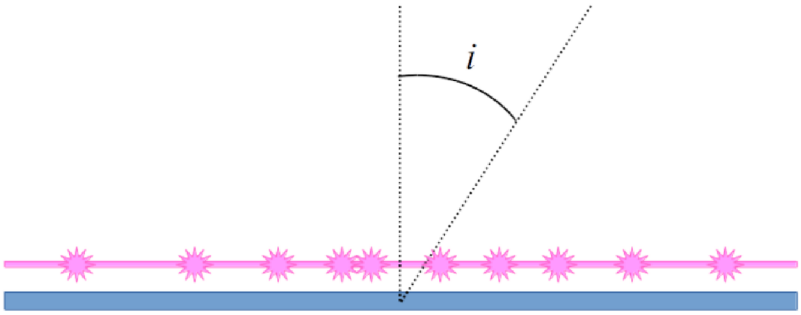

Figure 2.3: The geometry of PEXRAV with the blue plane representing the optically thick reflector and the source of X-ray photons in the magenta plane, parallel to the reflector. The inclination angle i is measured from the perpendicular to the planes to the line-of-sight pointing to the observer. The primary photons are emitted isotropically from the source plane. Figure adapted from Paltani & Ricci, 2017.

Semi-infinite slab geometry is not physically relevant for a obscuring torus structure as it does not account for transmission through the material and is usually associated with an accretion discs as PEXRAV is the standard reflection model implemented in the XSPEC environment. However, previously the PEXRAV was the only reflection model available and generally used and for the possibility of comparison we include it in our analysis. The model used was defined by the following expression

```
constant * tbabs (ztbabs * cabs * cutoffpl + apec + pexrav +
                constant * cutoffpl + zgauss).
```

The PEXRAV component has the following parameters: the power law photon index Γ, cut-off energy E_C, reflection scaling factor $rel_{\rm refl}$, redshift z, abundance of elements heavier than He with respect to the solar abundance and the iron abundance, cosine of the inclination angle i and normalization factor K that gives the photon flux at 1 keV. If $rel_{\rm refl} < 0$, the reflection component is obtained only and the actual reflection normalization is given by the $\mid rel_{\rm refl} \mid$. For $rel_{\rm refl} = 0$ there is no reflection component and only an equivalent `cutoffpl` component is produce.

BORUS02

BORUS02 is a physically-motivated obscuring torus model based on a Monte Carlo radiative transfer code BORUS by Baloković et al., 2018. The computation is done in a three dimensional space where the geometry of the reprocessing medium has shape of a uniform-density sphere with two conical polar cutouts, leaving the opening angle as a free parameter of the model. The uniform density simplification can be understood as a smoothed distribution of the individual clouds comprising the torus as represented on figure 2.4. The primary emission is given by the Green's functions for initial photons with energies from 1 keV up to 1 Mev that subsequently propagate through cold, neutral and static torus medium. The cross-sections for photoelectric absorption and Compton scattering are taken from NIST/XCOM[4] web database (Berger & Hubbell, 1987) with elemental abundances from Anders & Grevesse, 1989. In the case of the photoelectric absorption, the emission of fluorescence photons is based on the fluorescence yields for the Kα doublet and Kβ from Krause, 1979.

The model was defined by the following model sequence

```
constant * phabs (apec + atable{borus02_v170323a.fits} +
    zphabs * cabs * cutoffpl + constant * cutoffpl).
```

The `borus02_v170323a.fits` file shows the version of the table model that is loaded as an additive table model component (called by the `atable` command) in the model defining expression. The model consists of following parameters. The photon index Γ can acquire values in the range $1.4 - 2.6$. The high-energy cut-off $E_{\rm cut}$ is given in keV. The line-of-sight column density is given in logarithmic scale, $\log_{10}(N_{\rm H}/{\rm cm}^{-2}) = 22.0 - 25.5$. The covering factor as a free parameter is simply defined by the half-opening angle of the polar cutouts as $C_{\rm tor} = \cos\theta_{\rm tor}$. The half-opening angle is measured from the symmetry axis towards the equator and can acquire values from 0°(corresponding to the full covering) to 83°(corresponding to 10% disc-like covering). The torus geometry for 4 different opening angles is shown in figure 2.5. That corresponds to values of covering factor $0.1 - 1.0$. The element abundance is Sun-like except for the iron abundance, which is allowed to vary as $A_{\rm Fe}/A_{\rm Fe,\odot} = 0.01 - 10.0$. The cosine of inclination angle measured from the symmetry axis towards the equator can vary in range $\cos\theta_i = 0.05 - 0.95$ or $\theta_i/{\rm deg.} = 19 - 87$. The redshift z is set to a frozen value and the normalization of the intrinsic spectrum K given in photons/keV/cm^2/s at 1keV.

[4] https://www.nist.gov/pml/xcom-photon-cross-sections-database

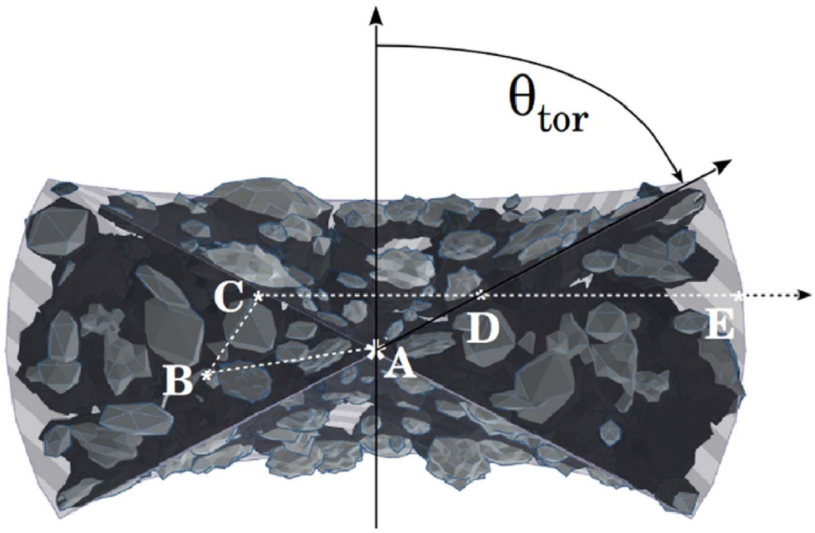

Figure 2.4: The cross section of the BORUS02 torus geometry as a physically reasonable clumpy structure. The approximation consists of smoothing the individual clouds into a uniform density within the torus. The opening angle of torus is labelled as $\theta_{\rm tor}$ measured from the symmetry axis towards the equator. The white dashed line traces an individual photon ray escaping the reprocessing material in point E. In case of clumpy structure the photon can escape the torus directly from point C without any further absorption or scattering if it passes between individual clouds. Figure adapted from Baloković et al., 2018.

MYTORUS

MYTORUS[5] is an empirically-motivated spectral model created by Murphy & Yaqoob, 2009. The Monte Carlo code-based model assumes a source of isotropic X-ray emission located in the origin of the coordinates. The reprocessing material is uniform and neutral, with geometry based on a tube-like azimuthally symmetric torus with a circular cross-section as visualized on figure 2.6, corresponding to the classical 'doughnut' type geometry. The half-opening angle is given by the fraction between the distance from the center of the torus to the center of the circular cross-section and the radius of the tube c/a and it is fixed to 60°or to $c/a = 2$. This corresponds to fixed value of the covering factor 0.5. The inclination angle $\theta_{\rm obs}$ is the angle between the symmetry axis and the observer's line-of-sight and acquires values from 0°up to 90°. System with $\theta_{\rm obs} = 0°$ would be seen face-on and therefore unobscured, while system with $\theta_{\rm obs} = 90°$ is obscured as seen edge-on. The equivalent hydrogen column density of the torus as defined by the model $N_{\rm H}$

[5]Availible at https://mytorus.com

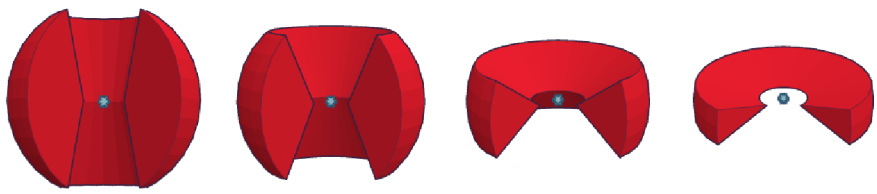

Figure 2.5: The `borus02` model geometry for 4 different opening angles. Figure adapted from https://sites.astro.caltech.edu/~mislavb.

corresponds to the global column density through the diameter of the tube of the torus. The actual column density as observed from the observer's line-of-sight is given as following

$$N_{\mathrm{H,los}} = N_{\mathrm{H}} \left[1 - \left(\frac{c}{a} \right)^2 \cos^2 \theta_{\mathrm{obs}} \right]^{1/2} . \tag{2.13}$$

The equatorial column density as a model parameter is given in the units of 10^{24} cm^{-2}. The photon index of the intrinsic power-law continuum Γ can acquire values in range 1.4 - 2.6.

The model consists of various components, each presented as a single table model. The zeroth-order continuum component

$$\mathrm{MYTZ}\,(z, N_{\mathrm{H}}, \theta_{\mathrm{obs}}, E)$$

is implemented in the form of an exponential table model using `etable`. It is comprised of the intrinsic continuum emission that escapes the system without any interaction with the reprocessing material. The unscattered continuum depends on the cosmological redshift of the source z, the equatorial column density N_{H}, the inclination angle θ_{obs} and the energy E. The scattered continuum component

$$\mathrm{MYTS}\,(z, A_{\mathrm{S}}, \Gamma, N_{\mathrm{H}}, \theta_{\mathrm{obs}}, E)$$

is in the form of additive table (`atable`). In addition to the already described parameters there is a normalization of the scattered continuum A_{S} in units of photons cm^{-2} s^{-1} keV^{-1}. If A_{S} is tied to the normalization of the incident power-law continuum component, the MYTS will be normalized for that power-law continuum that gives the photon flux at 1 keV. The third, line emission additive component

$$\mathrm{MYTL}\,(z, A_{\mathrm{L}}, \Gamma, N_{\mathrm{H}}, \theta_{\mathrm{obs}}, E)$$

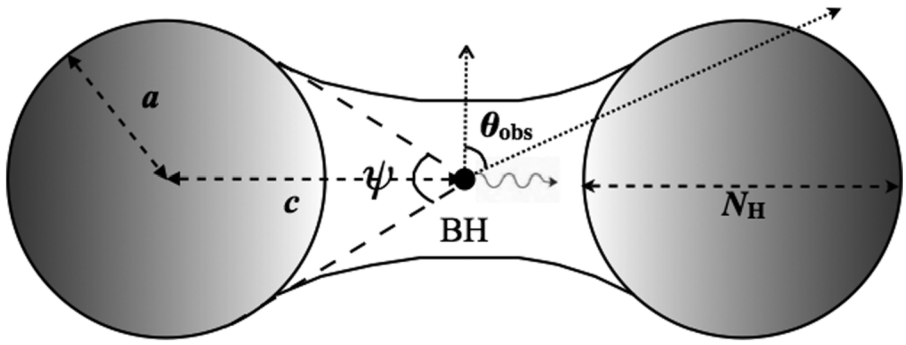

Figure 2.6: Cross-section of the 'doughnut' geometry of the MYTorus. The c is the distance from the center of the torus, where the central black hole (BH) lies in the origin of the coordinates, to the center of the tube (the center of the circular cross-section), while a is the radius of the tube. The inverse tangent of the fraction c/a gives the half-opening angle of the torus $[(\pi - \psi)/2]$ that is fixed to 60°. The inclination angle $\theta_{\rm obs}$ is measured from the symmetry axis towards the equator. The global column density is given as seen through the full diameter in the equatorial plane. Figure adapted from Murphy & Yaqoob, 2009.

combines the the zeroth-order and the scattered line emission including Fe Kα and Fe Kβ fluorescent lines. The normalization of the integrated flux for each fluorescent line is done by tying the $A_{\rm L}$ parameter to the normalization of the incident power-law continuum.

The high-energy cut-off of the intrinsic continuum in not a free parameter in the MYTorus model. The termination energy $E_{\rm T}$ can be chosen from a discrete set of values for which the individual model tables are created. In this work the value $E_{\rm T}$ = 300 keV was used for both scattered continuum and line emission components. Additionally, a Gaussian width of the fluorescent emission lines is given by the $\sigma_{\rm L}$ parameter within the `gsmooth` model component with the energy index α frozen at 1.0. The used model expression is as follows

```
constant * phabs (apec + constant * zpowerlw + zpowerlw *
etable{mytorus_Ezero_v00.fits} + constant *
atable{mytorus_scatteredH300_v00.fits} + constant * gsmooth *
atable{mytl_V000010nEp000H300_v00.fits}).
```

UxClumpy

The Unified X-ray Clumpy (UxClumpy[6]) torus model is based on a Monte Carlo X-ray radiative transfer simulation code XARS[7] (X-ray Absorption Re-emission Scattering) developed by Buchner et al., 2019. This physically-motivated table model assumes isotropically emitting point-source in the center of the obscurer geometry. The photoelectric absorption, Compton scattering and fluorescence line emission are simulated self-consistently as the photon rays propagate through the matter. The geometry of UxClumpy, as the name suggests, is based on a clumpy torus formed by $\mathcal{N}_{\rm tot} = 10^5$ spherical randomly distributed clouds. The angular size of individual blobs has an exponential distribution that is centred around $\theta_{\rm cloud} = 3°$, while their diameter is given as $D_{\rm cloud} = d \sin\theta_{\rm cloud}$ for a distance d. There is a diversity of the column density of individual clouds with a log-normal distribution $\log N_{\rm H,cloud}/{\rm cm}^{-2} = 23.5 \pm 1.0$.

The motivation behind the clumpy model is that the simple geometries with uniform density distribution of the reprocessing material cannot explain observed time-variations in the line-of-sight column density. Such variability in AGN is interpreted as the cloud eclipse events (Markowitz et al., 2014; Risaliti et al., 2002) with the only obscurer torus model capable of satisfying explanation is a clumpy one. The construction of a model geometry composed of large number of clumps has in principle infinite degrees of freedom. For simplicity a symmetry around one axis is assumed. The visualization of the model geometry is in the figure 2.7.

The obscurer column density is highest in the equatorial plane where the number of clouds along the line-of-sight for edge-on system is $\mathcal{N}_0$. The number of clouds seen along the radial line-of-sight $\mathcal{N}$ is axi-symmetric and decreases with the inclination angle β towards the poles according to a Gaussian function

$$\mathcal{N} = \mathcal{N}_0 \exp\left[-\left(\frac{\beta}{\sigma_{\rm TOR}}\right)^2\right], \tag{2.14}$$

where $\sigma_{\rm TOR}$ is the torus dispersion controlling the torus scale height.

An additional Compton-thick reflector component was added to the model as without it the model was not capable to reproduce the relative sharpness of the Compton hump of some local heavily obscured AGN. This new obscurer relatively near the hot corona is purely optional and is composed out of two rings of spherical Compton-thick clouds forming a thick doughnut. A free covering factor C determines the radius of the clouds and therefore the number of touching inner clouds used from three up to sixteen. Visualization of the additional inner ring is shown in figure 2.8.

[6] https://github.com/JohannesBuchner/xars/blob/master/doc/uxclumpy.rst
[7] Available at https://github.com/JohannesBuchner/xars.

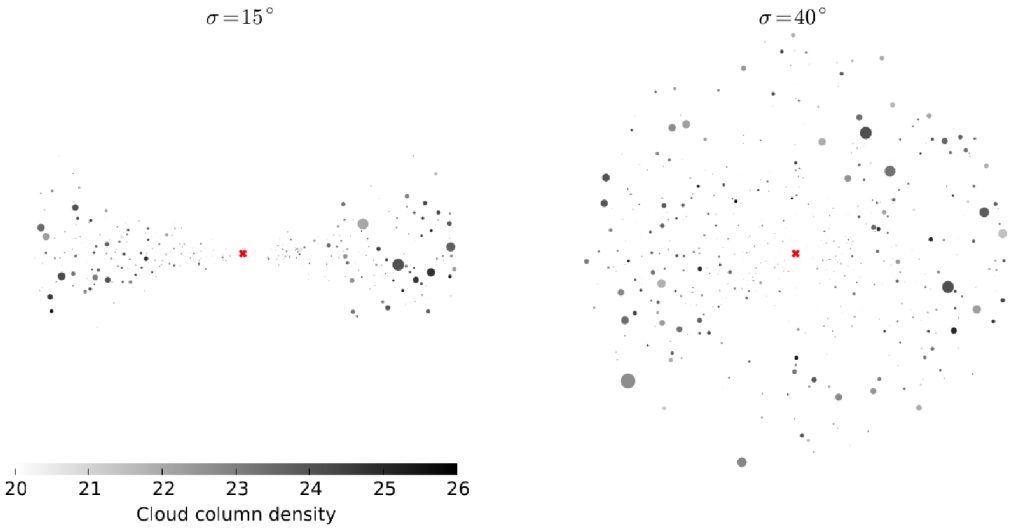

Figure 2.7: The cross-section of the UxClumpy geometry for two different vertical extends $\sigma_{\rm TOR}$. The red cross indicates the central point-source of the X-ray continuum located in the origin of the coordinates. The darkness of the clouds shows the column density of the individual blobs. A detailed fly-though video of the possible configurations is available online. Figure adapted from Buchner et al., 2014.

The model set-up is composed of three Xspec tables corresponding to three spectral components. The `transmit` and `reflect` tables include the transmitted and cold reflected components with fluorescent line emission while the `omni` table represents the warm mirror component. All components are additive table models and have the same parameters. The `TORsigma` is the dispersion of the cloud population and corresponds to the angular width $\sigma_{\rm TOR}$. `TORsigma` and can acquire values ranging from 6° up to 90°. The covering factor of the inner ring $C_{\rm CTK}$ is defined by the `CTKcover` parameter and can acquire values in range 0 - 0.6. The viewing or inclination angle $\theta_{\rm inc}$ spans in range 0°- 90°. Unlike so far described models the total column density $N_{\rm H,los}$ is not the equatorial column density, but the one in the line-of-sight. The model enables values of column density in the following range $10^{20} - 10^{26}$ cm^{-2}. The exponential high-energy cut-off is given by the $E_{\rm cut}$ parameter allowed to vary as 60 - 400 keV. The model defines the photon index Γ parameter with possible values in range 1 - 3, the normalization of the power-law K and the redshift z. The model set-up in Xspec is given by the following expression,

```
constant * tbabs (apec + atable{uxclumpy-cutoff-transmit.fits}
    + atable{uxclumpy-cutoff-reflect.fits} + constant *
            atable{uxclumpy-cutoff-omni.fits}).
```

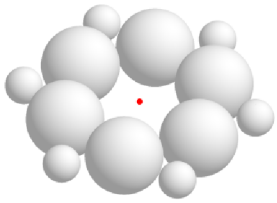

Figure 2.8: Compton-think inner ring composed of six touching clouds with additional six gap-filling clouds around the central point-source in *red*. The covering factor of this configuration is 30%. Adapted from Buchner et al., 2019.

In our model set-up the parameters of all table components are tied together.

RXTorus

The RXTorus physically-motivated model by Paltani & Ricci, 2017 is generated with ReflexX[8], a Monte Carlo code designed for tracking the individual X-ray photons. The ray-tracing simulation consists of four separate engines; photon creation, geometrical description, photon propagation and the definition of the physical processes. ReflexX simulation tool allows the user to define each. RXTorus is the first application of ReflexX, adapting the same source and absorber geometries as MYTorus but allowing the opening angle to vary, while the metallicity is set to solar. The composition is taken from Anders & Grevesse, 1989 for compatibility with MYTorus. For each simulation there are 5×10^8 photons generated with the primary X-ray spectrum assumed to be a power-law with maximum photon energy 300 keV. These photons are ray-traced until they die, down-scatter below the chosen termination energy or leave the system. Physical processes accounted for are the following. The Compton scattering as an inelastic interaction between a photon and a free electron is approximated by quasi-elastic Thompson scattering in the low-energy limit. The cross-section of the Compton scattering is given by the full Klein-Nishina relativistic differential cross-section (Liu & Li, 2014). The cross-section for photoelectric absorption by bound electrons was provided by Verner & Yakovlev, 1995, determined from the analytical fits for 30 elements. After photoionization, either Auger effect or fluorescence photon emission from K or L shell can occur.

There are several table model components. The `RXTorus_cont_M` is an exponential tabular model for the continuum absorption component where `M` denotes the metallicity (solar for `M` = 1). The transmitted continuum contains only photons

[8]Availible at https://www.astro.unige.ch/reflex

that did not undergo any physical processes and has two parameters; the redshift z and the hydrogen column density along the line of sight in units of 10^{22} cm^{-2} that can range from 10^{22} cm^{-2} up to 10^{25} cm^{-2}. The line-of-sight column density is given as following

$$N_{\mathrm{H,los}} = N_{\mathrm{H,eq}} \left(1 - \frac{R^2}{r^2} \cos^2 i\right)^{1/2} \quad \text{for } \cos i < \frac{r}{R}, \tag{2.15}$$

where $N_{\mathrm{H,eq}}$ is the equatorial column density, r is the radius of the tube and R is the distance from the center of the torus (origin of the coordinates and the location of the X-ray source), to the center of the tube. The inclination angle is labelled as i. For $\cos i < r/R$ the line-of-sight column density equals to zero. The line-of-sight column density was defined in the XSPEC session in the following way

```
Nh = NHeq*sqrt(max(0.0,1.0 - (cosd(Inclination)/(r/R))^2.0)).
```

The sketch of the cross-section of the torus model is in figure 2.9.

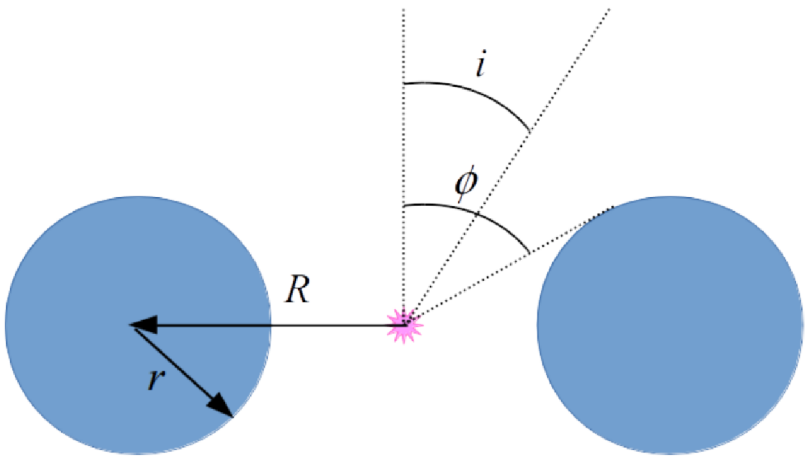

Figure 2.9: The RXTORUS model adapts the geometry from MYTORUS. The figure shows the cross-section of a toroidal reprocessing structure in *blue* with varying fraction r/R giving the covering factor C_{f}. In MYTORUS model the fraction R/r is frozen to value of 2. The ϕ angle is the opening angle defined as $\cos\phi = r/R$. Inclination or the viewing angle denoted as i is defined as the angle between the normal to the plane of the system and line of sight to the observer. X-ray source emitting isotropically is located in the origin of the coordinates and the center of the torus by *magenta* star. Figure adapted from Paltani & Ricci, 2017.

The reprocessed emission accounting for the scattered component and the fluorescent line emission is given by the additive table component `RXTorus_rprc_M_CCC`

where the metallicity is solar (M = 1) and CCC labels the high energy cut-off. In our case the $E_{\rm cut}$ = 200 keV, therefore CCC = 200. The reprocessed model component has following parameters. The photon index Γ is allowed to vary in range 1 – 3. The hydrogen column density is the equatorial column $N_{\rm H,eq}$ covering the range from 10^{22} cm^{-2} up to 10^{25} cm^{-2}. Inclination angle i can acquire values 0°– 90°. The fraction r/R gives the opening angle of the torus $\cos\phi = r/R$ corresponding to the torus covering factor $C_{\rm f} = r/R$. The ratio r/R varies from 1 (corresponding to torus without a central hole, a *horn* torus with $\phi = 0$), to 0.01. The redshift z can span across the range 0 – 5 and the normalization K is given in units of photons keV^{-1} cm^{-2}.

In our set-up the model was defined using the following expression:

```
constant * phabs (apec + constant * cutoffpl + constant *
    cutoffpl * etable{RXTorus_cont_1.mod} + constant *
            atable{RXTorus_rprc_1_200.mod}).
```

Different torus geometry has influence on the spectral shape of the broadband X-ray spectrum of an AGN and in particular on the Compton hump. The X-ray spectrum is shaped by the increasing column density of the reprocessing material with the absorption predominating in the soft band and the Compton scattering in the hard band. The intensity of the spectrum in the soft band decreases significantly with increasing column density up to certain value, where no more primary emission can reach the observer, while the Compton hump with the fluorescent iron line is becoming more dominant for higher columns. Figure 2.10 shows the changes in the spectral shapes for described empirically-motivated table models with increasing hydrogen column density. Each model acquires slightly different shapes of the Compton hump due to different and unique geometries and model built-ups. It is also notable the difference between the column density ranges that are allowed by individual models. Additionally, MYTorus model is defined only from 0.6 keV as seen in the figure 2.10.

2.3.4 Key parameters estimation

In this section the process of estimation of the key parameters is described.

Luminosity

The intrinsic X-ray luminosity of the studied AGN is computed in the energy range $E_{\rm low} - E_{\rm high}$ using the following equation

$$E_{\rm low} - E_{\rm high} = 4\pi r^2 F = 4\pi r^2 \times \int_{E_{\rm low}}^{E_{\rm high}} E \times M(E)\,{\rm d}E \qquad (2.16)$$

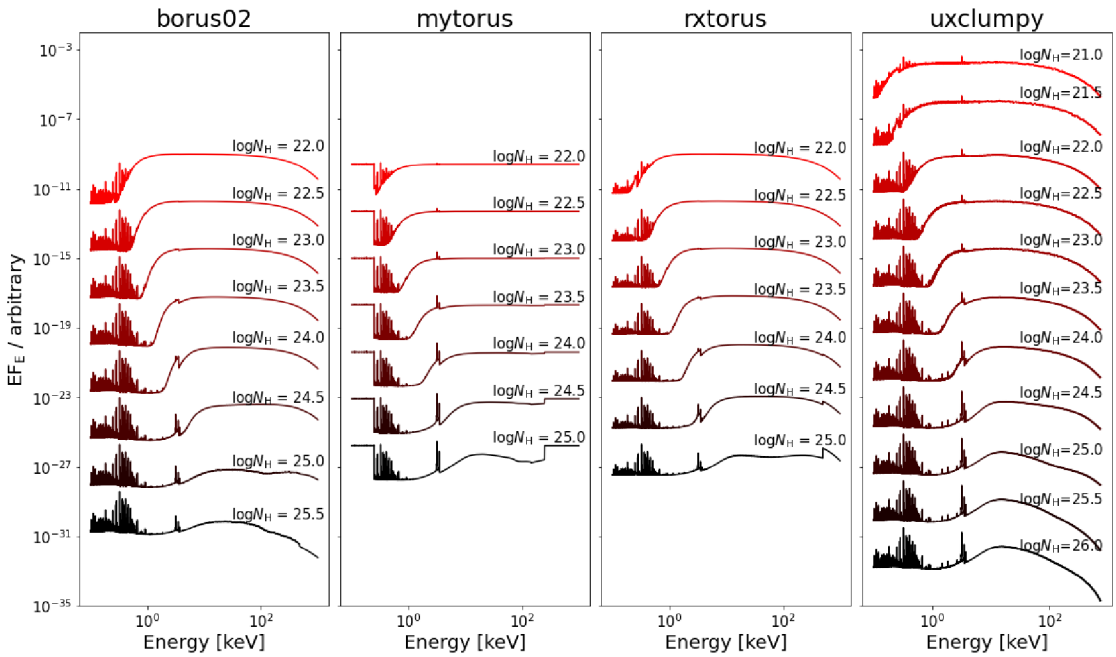

Figure 2.10: Broadband X-ray spectral shapes of physically-motivated obscurer models.

where $M(E)$ corresponds to a redshifted power-law model with exponential cut-off given by the expression

$$M(E) = K\,[E(1+z)]^{-\alpha}\exp\left(-\frac{E}{\beta}\right).$$

Here E is energy in keV, K is normalization in units photons/keV/cm^2/s, z is redshift, α is the dimensionless photon index and β is the energy of exponential cutoff in keV.

Eddington fraction

The Eddington fraction $\lambda_{\rm Edd}$ is given by the fraction between the bolometric luminosity $L_{\rm bol}$ of the studied AGN and its Eddington luminosity $L_{\rm Edd}$ as

$$\lambda_{\rm Edd} = \frac{L_{\rm bol}}{L_{\rm Edd}}. \tag{2.17}$$

The bolometric luminosity is calculated using the following formula

$$L_{\rm bol} = L_{2-10\,{\rm keV}} \times \kappa_{\rm bol}\,{\rm erg\,s^{-1}}, \tag{2.18}$$

where $\kappa_{\rm bol}$ is the X-ray correction bolometric factor. The Eddington luminosity of an AGN is given by formula

$$L_{\rm Edd} = \frac{4\pi G M_{\rm BH} m_{\rm p} c}{\sigma_{\rm T}} = 1.26 \times 10^{38} \left(\frac{M_{\rm BH}}{M_\odot}\right) {\rm erg\,s^{-1}}, \tag{2.19}$$

where $M_{\rm BH}$ is the mass of the SMBH given in the units of solar masses, $m_{\rm p}$ is the mass of a proton and $\sigma_{\rm T}$ is the Thompson cross-section (Ricci et al., 2017a).

Equivalent width

For pexrav model the equivalent width EW of Fe Kα line was calculated according to the following formula,

$$\mathrm{EW} = \frac{F_{\rm line}}{F_{\rm cont}}, \tag{2.20}$$

where $F_{\rm line}$ is the flux in the line given by the normalization parameter of the `zgauss` model component and $F_{\rm cont}$ is the flux of the continuum at the line energy given by the normalization multiplied by the line energy to the power of minus photon index. The EW calculated according to the formula 2.20 was compared to the value obtained by `eqwidth` command in the XSPEC environment.

2.4 Bayesian X-ray Analysis

The Bayesian X-ray Analysis (hereafter BXA) is a tool for X-ray spectral fitting with global parameter exploration. This robust fitting algorithm connects X-ray spectral analysis environments like XSPEC to Bayesian methodology such as nested sampling algorithms for Bayesian parameter estimation and model comparison with the Bayesian evidence (Buchner et al., 2014).

Bayesian inference methods are based on the Bayes' theorem stating that

$$P(\Theta\,|\mathrm{D}, H) = \frac{P(\Theta\,|H)\,P(\mathrm{D}|\,\Theta, H)}{P(\mathrm{D}|H)}, \tag{2.21}$$

where Θ is the set of parameters we want to estimate in a model or a hypothesis H and D represents the observed data. Here $P(\Theta\,|H) \equiv \pi(\Theta)$ is the *prior distribution* representing our knowledge prior to the observation of data D, $P(\mathrm{D}|\,\Theta, H) \equiv \mathcal{L}(\Theta)$ is the *likelihood* or the sampling distribution representing the likelihood of the data given the model parameters with $P(\Theta\,|\mathrm{D}, H)$ being the updated knowledge after observing the data D called the *posterior probability distribution*. Finally, $P(\mathrm{D}|H) \equiv \mathcal{Z}(\mathrm{D})$ is the Bayesian evidence representing the distribution of data D and acting like a normalization for the posterior distribution (van Dyk et al., 2001).

Bayesian analysis has many advantages in X-ray spectroscopy. First of all, it is a robust and unsupervised systematic fitting algorithm with only a minimal user input required for the initial parameter estimations. The parameter space is weighted by used-defined prior distributions consisting of all our knowledge about the model parameters, such as allowed parameter ranges, assuming Poisson distribution of the observed counts. The posterior distribution represents the probability distribution combining the information included in the prior and the data as it is a complete summary of of our information about the parameter. It is usually summarized by the posterior mean $\hat{\Theta} = E(\Theta|\mathrm{D}, H)$ and the variance $\mathrm{var}(\theta|\mathrm{D}, H)$ interpreted at the mean value of the parameter and its error. Secondly, BXA is capable to give informative constraints on the parameter confidence contours even in the very low count regime even when a source is not detected or for complex parameter spaces with strong degeneracies, making it a suitable tool for heavily obscured AGN and a low-luminosity source data analysis. Parameter estimation in BXA is done by identification of a sub-volume in the multidimensional parameter space constituting to the majority of the probability integral over the space. The optimisation and error estimation are realized simultaneously requiring an integration technique capable of performing the integration in high dimensionality (Buchner et al., 2014). Commonly employed integration methods for Bayesian parameter estimation are Monte Carlo integration techniques such as Markov chain Monte Carlo (MCMC) or nested sampling algorithms.

2.4.1 Nested Sampling

The problems of MCMC like the convergence, as it has a difficulty with finding and jumping between well-separated maxima while used as a local algorithm, have been avoided by development of nested sampling. Nested sampling (introduced by Skilling, 2004) is also a Monte Carlo technique used to efficiently evaluate the Bayesian evidence while producing the posterior probability distributions on model parameters. The Bayesian evidence, that can not be easily estimated by MCMC algorithms, can be furthermore used for model comparison. MultiNest Feroz et al., 2009, a ellipsoidal nested sampling technique applied in this work, scans the parameter space from the least probable areas to the most probable ones through a set of so called *live points*, each corresponding to a vector, sorted by their likelihood and drawn from the prior distributions using an ellipsoidal boundary. The multi-dimensional ellipsoid is determined from the covariance matrix of the current set of active live points. The algorithm than iteratively forms a likelihood contours and removes the least likely point followed by regeneration of a new ones with better likelihood until the sub-volume of the multidimensional parameter space with the highest likelihood remains. The algorithm terminates unsupervised once the remaining live points occupy a tiny prior volume whose contribution to

the integral is negligible. The Bayesian evidence can be consequently used for model comparison with the Bayes factor. Figures 2.11 and 2.12 are showing the likelihood contours and corresponding evidence integral for a two dimensional problem.

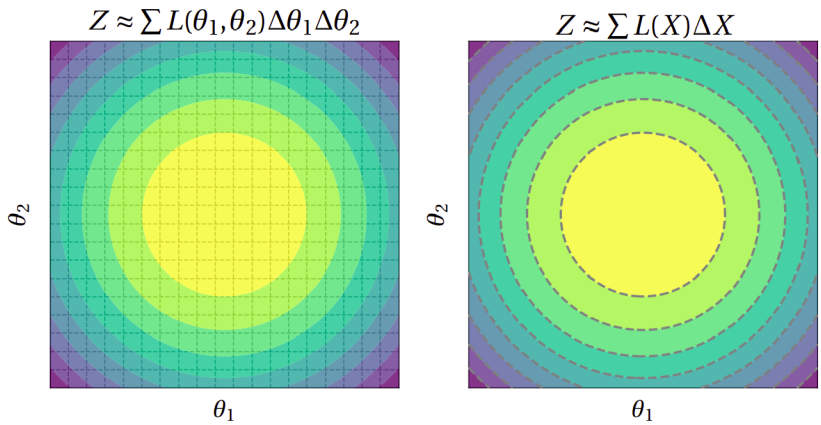

Figure 2.11: Nested sampling evidence identity adapted from Ashton et al., 2022. Each color represents a contour of a two dimensional likelihood function. Nested sampling sums over a region of combined cubes of similar likelihoods (*right*) rather than summing up over separate cubes (*left*).

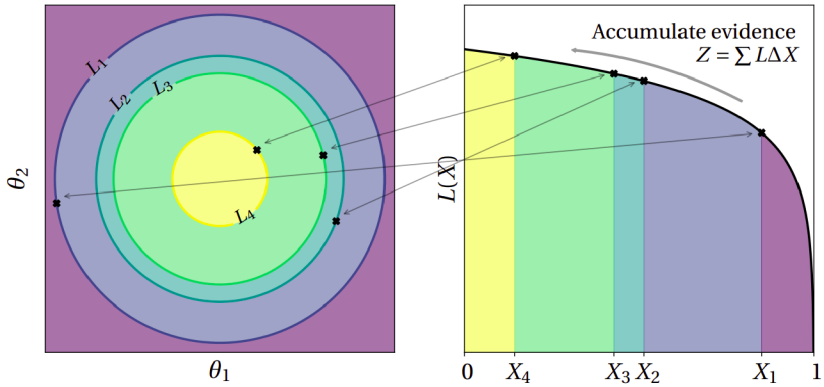

Figure 2.12: Nested sampling in a two dimensional problem adapted from Ashton et al., 2022. The so-called iso-likelihood contours corresponding to the individual points in two dimensional parameter space are shown *left* while the corresponding contributions to the evidence integral is *right*. The volumes X_i are estimated statistically in nested sampling algorithms.

Summarizing, the main advantages of BXA and nested sampling are:

- It is a robust, unsupervised global exploration of the parameter space requiring a minimal user input for the initial parameters.
- It is efficient in systematic analysis of large datasets.
- It provides the Bayes evidence that can be used for model comparison with the Bayes factor.
- It has a well-defined point of convergence.
- It is capable of estimating informative constraints for fitted parameters even for low count regimes with realistic models.

3 Spectral Analysis of NGC 3982

3.1 NGC 3982

NGC 3982 is a late-type Seyfert 2/1.9 galaxy located in our cosmic backyard with a median redshift-independent Hubble distance of 18.91 ± 1.33 Mpc[1]. The barred spiral galaxy harbours an low-luminosity AGN obscured by a circumnuclear torus within the sphere of influence of the SMBH rather than from the low-inclination host galaxy. Basic properties of NGC 3982 are listed in table 3.1 and optical and X-ray images of NGC 3982 are in the figure 3.1.

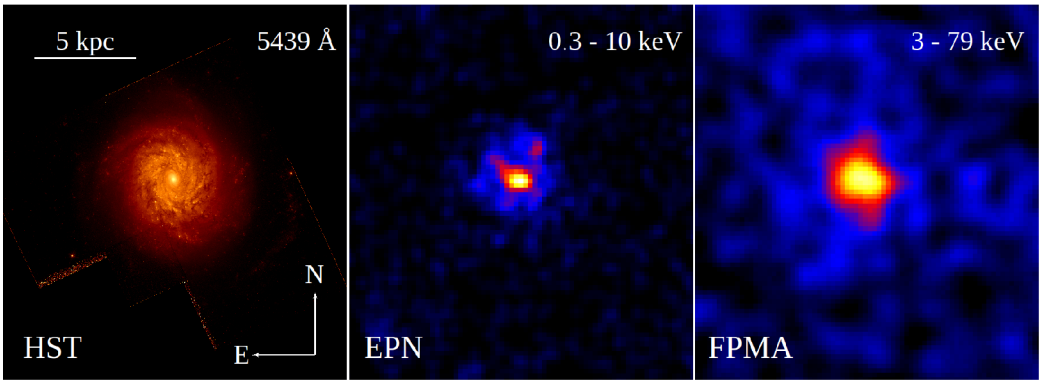

Figure 3.1: Optical image of NGC 3982 from *Hubble* Space Telescope[2] (*left*) is showing the spiral structure of the host galaxy seen under a low-inclination angle, yet the active galactic nucleus seems to be heavily obscured (Kammoun et al., 2020; Saade et al., 2022) as seen at higher inclination angles. X-ray images from EPIC PN instrument on board *XMM-Newton* in energy range 3 – 10 keV (*middle*) and FPMA instrument on board *NuSTAR* in energy range 3 – 78 keV (*right*) are matched with the optical one.

[1]Adapted form the NASA/IPAC Extragalactic Database (NED) at https://ned.ipac.caltech.edu/.
[2]Downloaded and adjusted from Hubble Legacy Archive at https://hla.stsci.edu/.

Table 3.1: Basic properties of NGC 3982.

	R.A. (J2000) [°]	Dec. (J2000) [°]	Redshift	Inclination [°]	Morphology
NGC 3982	179.117204	55.125238	0.00371	26.2 ± 5.2[a]	SAB(r)b

[a] From Li et al., 2021.

NGC 3982 has been studied by many previous works. First time it has been observed in X-ray band by *ASCA* (Moran et al., 2001). It was found to be a compact source with extended nuclear emission (Asmus et al., 2014) surrounded by a partial ring of star formation with an approximate radius of 500 pc (Brum et al., 2017). Rush & Malkan, 1996 and Ghosh et al., 2007 reported a very low hardness ratios of -0.8 ± 0.1 and -0.7 ± 0.1 from the *ROSAT* and *Chandra* observations respectively. A presence of extended emission in the *XMM-Newton* field was found by LaMassa et al., 2011 and Esparza-Arredondo et al., 2020 identified NGC 3982 as a fading AGN candidate.

NGC 3982 was classified as a type 1.9/2 by Quillen et al., 2001 and many following works are adopting or reporting the type 1.9 classification (Panessa et al., 2006, Akylas & Georgantopoulos, 2009, Saade et al., 2022). On the other hand, many other works classify NGC 3982 as a type 2 AGN (Guainazzi et al., 2005, Trippe et al., 2010, Balmaverde & Capetti, 2013). Trippe et al., 2010 claim that it always really had been a type 2 galaxy as there is no convincing evidence from the literature that it ever changed type, with *Spitzer* spectrum of NGC 3982 being a typical type 2 AGN spectrum and with no trace of broad Hα in SDSS observations (3800 – 9200 Å).

NGC 3982 was serendipitously observed with *Chandra* as part of the *Chandra* Deep Field North survey (Alexander et al., 2003) and by *XMM-Newton* observatory in 2004. Many studies analysing these observations together with the *ROSAT* data found it to be a CTK candidate (Guainazzi et al., 2005, Panessa et al., 2006, Ghosh et al., 2007, Cardamone et al., 2007, Shu et al., 2007, Akylas & Georgantopoulos, 2009, Trippe et al., 2010, Liu & Wang, 2010, Brightman & Nandra, 2011a, LaMassa et al., 2012, Balmaverde & Capetti, 2013). As Ghosh et al., 2007 studied NGC 3982 within a sample of true Seyfert 2 candidates (AGN lacking BLR region), they conclude that NGC 3982 is not a good true type 2 candidate, but it is rather an obscured source. Shu et al., 2007 classified NGC 3982 as a CTK source based on large Fe Kα EW (6 ± 3 keV) and small $F_{2-10\ \mathrm{keV}}/F_{\mathrm{OIII}}$ ratio (< 0.1).

The intrinsic column density and therefore the X-ray classification of an AGN is difficult to estimate only by studying the soft X-ray spectra. In December 2017 NGC 3982 was observed in the hard X-ray band by *NuSTAR* as part of the CfA Seyferts Extragalactic Legacy Survey. Kammoun et al., 2020 used *XMM-Newton*

PN data with *NuSTAR* observations for broadband X-ray modelling by PEXMON, MYTORUS coupled and MYTORUS decoupled models with one and two independent column density parameters. Their analysis using PEXMON and MYTORUS coupled models predicts CTN source while with MYTORUS decoupled they found NGC 3982 to be a CTK AGN. They also report log $M_{\rm BH}$ = 6.89 from velocity dispersion using SDSS data.

So far the most detailed X-ray study of NGC 3982 was done by Saade et al., 2022 analysing *Chandra* and *NuSTAR* observations, whom confirmed the CTK nature of NGC 3982. Their spectral model is based on two absorbed power-laws with thermal and BORUS02 component. Works analysing X-ray data of NGC 3982 and their main results regarding the column density, intrinsic X-ray luminosity in 2 – 10 keV band and EW of Fe Kα line are summarized in table 3.3. Figure 3.2 shows the X-ray images of NGC 3982 from three *XMM-Newtons* EPIC detectors and *NuSTAR* images from FPMA and FPMB detectors are in the figure 3.3.

Table 3.2 summarizes the observational information about the data used for our analysis. The archival data were obtained in the *XMM-Newton* data archive[3] while the *NuSTAR* observation was downloaded from the HEASARC database available online[4]. *XMM-Newton* observed NGC 3982 on 15th of Jun in 2004 while by *NuSTAR* observatory it was observed on 6th of December in 2017.

Table 3.2: Observational information.

observatory	obs. ID	detector	net exposure time [ks]
XMM-Newton	0204651201	MOS1	11.35
		MOS2	11.35
		PN	9.14
NuSTAR	60375001002	FPMA	33.41
		FPMB	33.34

detector	extraction regions	
	source	background
MOS1	179.1172674 55.1252362 49”	179.0745937 55.1465348 65”
MOS2	179.1172674 55.1252362 49”	179.1715501 55.1319591 65”
PN	179.1165397 55.1228749 45”	179.0717030 55.1297278 50”
FPMA	179.1172675 55.1252362 49”	179.1727511 55.1709819 150”
FPMB	179.1172675 55.1252362 49”	179.1727511 55.1709819 150”

[3]Availible online at http://nxsa.esac.esa.int/nxsa-web/#home.
[4]At web page https://heasarc.gsfc.nasa.gov/docs/archive.html.

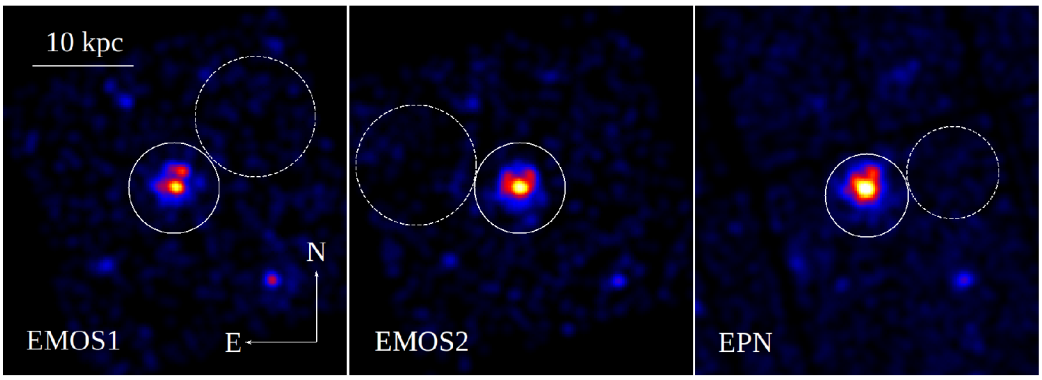

Figure 3.2: X-ray images of NGC 3982 from all three EPIC detectors on board *XMM-Newton* observatory: MOS1 (*left*), MOS2 (*middle*) and PN (*right*). The SAOImage DS9 visualization software version 8.3 was used to match the smoothed images together. The source extraction region for each detector is represented by the solid line circle with radius of 49 arcsec for MOS detectors and 45 arcsec for PN detector with small offset of ~ 9 arcsec due to the central readout node. The dashed line circles represent the background extraction regions individual for each detector, with radius of 65 arcsec for EPIC MOS and 50 arcsec for PN. For each detector the source-free background extraction region is located on the same chip as the source, for PN camera it is as close to the central readout node as the source extraction region due to reduction of instrumental noise (Smith & Guainazzi, 2022). All EPIC images show the X-ray emission in the energy $0.3 - 10.0$ keV with linear color scaling indicating the intensity.

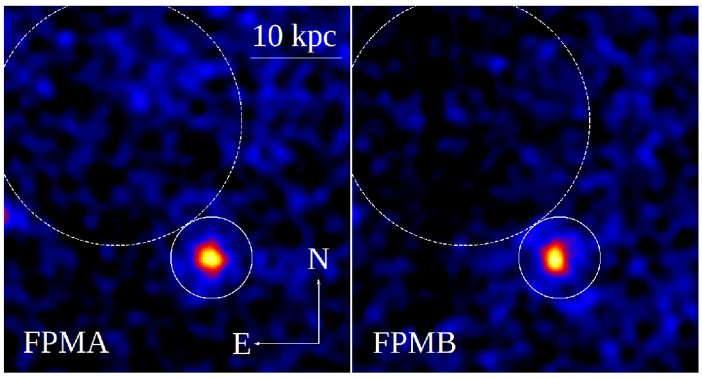

Figure 3.3: Same images of NGC 3982 as in the figure 3.2 but in the hard X-ray band as seen by two individual detectors on board *NuSTAR* observatory. The images from FPMA detector (*left*) and FPMB detector (*right*) are smoothed and matched in the SAOImage DS9 software. Source extraction regions for each detector are represented by solid line circles with radius of 49 arcsec centred at the source coordinates with source-free background extraction region represented by the dashed line circles with radius of 150 arcsec, same for each detector. The energy range visualized by both images is $3 - 78$ keV with intensity denoted by colors scaled linearly.

Table 3.3: Chosen studies on X-ray properties of NGC 3982. Column (2): the logarithm of the obscurer column density, column (3): the intrinsic X-ray luminosity, column (4): photon index, column (5): equivalent width of Kα line in keV.

Work (1)	$\log N_{\rm H}$ [cm^{-2}] (2)	$\log L_{2-10\ {\rm keV}}$ [erg/s] (3)	Γ (4)	EW (Fe Kα) [keV] (5)	note (6)
Rush & Malkan, 1996			2.12		with $N_{\rm H,gal}$
	$20.69^{+0.28}_{-0.96}$		3.40		with $N_{\rm H}$ free
Guainazzi et al., 2005	> 24.20		2.00	8 ± 5	local EW fits
				< 41	global EW fits
Panessa et al., 2006		41.18	1.80		
Ghosh et al., 2007	$21.36^{+0.14}_{-0.22}$		$3.70^{+0.90}_{-1.60}$		
Cardamone et al., 2007	23.38		1.70		
Shu et al., 2007	> 24.00		$3.74^{+1.80}_{-1.60}$	$6.31^{+3.50}_{-3.17}$	
Ho, 2009		38.76	1.80		
Akylas & Georgantopoulos, 2009	23.64 ± 0.22		$2.53^{+0.44}_{-0.42}$	$0.80^{+0.68}_{-0.42}$	
Trippe et al., 2010	$23.36^{+0.20}_{-0.16}$			0.94 ± 0.55	
Liu & Wang, 2010				< 1.18	
Brightman & Nandra, 2011a	23.34		1.83		
Brightman & Nandra, 2011b	23.34				
LaMassa et al., 2011	$21.71^{+0.08}_{-0.16}$	$38.77^{+0.04}_{-0.05}$	$0.57^{+1.14}_{-0.90}$		
LaMassa et al., 2012	$23.61^{+1.03}_{-0.23}$		$2.39^{+0.18}_{-0.15}$		
Kammoun et al., 2020	23.78	40.48	$1.97^{+0.35}_{-0.20}$		pexmon
	$23.99^{+0.07}_{-0.31}$	40.78	$2.22^{+0.17}_{-0.06}$		mytc-eq
	23.85				mytc-los
	$24.72^{+0.21}_{-0.42}$	40.00	$2.22^{+0.18}_{-0.06}$		mytd-1NH-los
	$24.72^{+0.21}_{-0.42}$	40.00	$2.22^{+0.18}_{-0.05}$		mytd-2NH-eq
	$24.65^{+0.23}_{-0.51}$				mytd-2NH-los
Esparza-Arredondo et al., 2020	$23.83^{+0.18}_{-0.20}$	41.12 ± 1.06	$3.06^{+1.27}_{-0.76}$		
Saade et al., 2022	> 25.30	$42.83^{+0.08}_{-0.13}$	$2.48^{+0.06}_{-0.29}$		

3.2 Local parameter estimation with XSPEC

For the spectral analysis the XSPEC package version 12.12.0g was used (Arnaud, 1996). The statistic used throughout this work is the modified C statistic called by `cstat` command. All datasets accounting for three *XMM-Newton* spectra and two *NuSTAR* spectra were modelled simultaneously with parameters of all datasets linked together. The fitting was performed in the energy range 0.3 – 10.0 keV for *XMM-Newton* spectra and in the energy range 3 – 78 keV for spectra observed by *NuSTAR* observatory, if not stated otherwise. The fixed parameters throughout the work are following. The multiplicative constant of the absorption component (`tbabs` or `phabs`) corresponding to a cross-calibration is frozen to value of 1 throughout the work as this value was found to be acceptable before freezing. The galactic column density for NGC 3982 is $N_{\mathrm{H,gal}} = 1 \times 10^{20}$ cm^{-2}, obtained by the `nh` command. Abundance was frozen at 1 corresponding to the Solar metallicity including the abundance of iron. Redshift of the studied source is well known with value of 0.00371. For the high energy cut-off the value of 300 keV was used and fixed or corresponding table model was applied (Baloković et al., 2021). The energy of the Fe Kα line was frozen to 6.4 keV.

The description and set-up for each model can be found in the section 2.3.3. Generally, the temperature kT and normalization in the `apec` component were modelled, together with the photon index and normalization of the corresponding power-law component. For table models having a normalization parameter, this was linked to the normalization of the power-law. For each model set-up the scattering fraction was set free with upper limit of 0.1 (corresponding to max 10% of scattered continuum).

For the PEXRAV model, the intrinsic column density of `ztbabs` model component was left free and linked to the column in the `cabs` component. The width of Fe Kα line was fixed to $\sigma = 1$ eV as well as the energy of the Fe Kα line with varying normalization. For the `pexrav` model component, the photon index and normalization were linked to the parameters defined by the power-law components but the cosine of the inclination angle was left free and the relative reflection `rel_refl` was limited to negative values in range (−100, −0.1) as the spectrum is assumed to be dominated by the reflection component. The best-fit values obtained in the modelling process are in the table 3.4 for better comparison with the results obtained from other models.

For photon index $\Gamma > 2$, the intensity decreases with energy as the source becomes more bright towards the shorter wavelengths. For the local modelling with XSPEC using PEXRAV model, the intrinsic column density was pegged to the hard upper limit corresponding to 9.99×10^{27} cm^{-2}. This is due to the poorly constrained transmitted component as the geometrical assumption of the obscurer

is not physically reasonable. As the reflection material is assumed to be located in semi-infinite geometrically thin slab, the line-of-sight column density of the reflector is not linked to the reflection strength. The value of $\cos i = 0.93$ corresponds to the inclination angle $i = 21.57°$.

For the BORUS02 model set-up the `phabs` component represents the Galactic absorption with the corresponding galactic column. In the coupled mode set-up the fitted parameters from the `borus02` component were the photon index Γ, the logarithm of the $N_{\rm H}$ of the torus, covering factor of the torus $CF_{\rm tor}$, cosine of the inclination angle $\cos\theta_{\rm inc}$ and the normalization K. The column density of the `zphabs` and `cabs` components were tied to the intrinsic column defined by `borus02` component and photon index with normalization of the `cutoffpl` were linked to the `borus02` as well. On the other hand, in the decoupled mode the column density of the `zphabs` and `cabs` components were tied together but varying independently from the column density defined by the `borus02` component. Also, for simplicity the inclination angle was frozen to a edge-on system with $\cos\theta_{\rm inc} = 0.05$ corresponding to 87.1°. Table 3.4 shows the best-fit values of varying parameters. For BORUS02 in the coupled mode the covering factor corresponds to large opening angle of 79.2°while the inclination angle is 81.4°, for the decoupled mode the covering factor corresponds to opening angle of 84.3°while the line-of-sight column density was pegged to the hard limit of 9.99×10^{27} cm^{-2}. This indicates that the fit favourites a low-covering dense obscurer possibly resembling a disc-like structure. Given the number of free parameters, this value is likely due to fit stuck in a local minimum.

The MYTORUS model was applied only in the coupled mode. The width of the Fe Kα line $\sigma_{\rm L}$ was frozen to 10^{-4} keV with energy index α fixed at value 1.0. The photon index, normalization of the power-law, column density and inclination angle of the scattered continuum MYTS and emission line MYTL table components are linked together to the varying parameters of the redshifted power-law and the zeroth-continuum MYTZ table component. Results in the table 3.4 show that the intrinsic column density was pegged to the hard upper limit 1×10^{25} cm^{-2} allowed by the model. The opening angle for MYTORUS model is fixed to value of 60°.

Regarding UXCLUMPY, the parameters of all three table components were tied together. The following torus characteristics were left varying: the line-of-sight column density in units of 10^{22} cm^{-2}, the torus dispersion labelled as the torus σ (`TORsigma`) and CTK covering factor (`CTKcover`) as $C_{\rm CTK}$. The inclination angle was frozen at 70°. Obtained CTK covering factor corresponds to opening angle of the inner ring of 80.3°.

For the last table model tested, RXTORUS, the line-of-sight column density as a parameter of the continuum component was defined as described in section 2.3.3 while the equatorial column density was left varying. Obtained fraction r/R corresponds to opening angle of the obscuring torus of 64.5°. The best-fit results

from the modelling by all models described above are summarized in the table 3.4 allowing to compare them.

Figure 3.4 shows the unfolded X-ray spectrum of NGC 3982 from both *XMM-Newton* and *NuSTAR* observatories. Different colors indicate different instrument, the *XMM-Newton* EPIC spectra for MOS1 in *black*, MOS2 in *red* and PN in *green* were used in the energy band 0.3 – 10.0 keV while *NuSTAR* FPMA (*blue*) and FPMB spectra (*purple*) were used in 3 – 78 keV energy band. Only for MYTorus modelling the energy band of soft X-ray data was limited to 0.6 – 10.0 keV due to the model limitations. The best-fit model is shown only for borus02 model with corresponding residuals in the sub-plot below the spectrum. For every other model only the residuals are shown, as the differences between the best-fit models were unrecognisable by eye.

3.3 Bayesian X-ray Analysis

For the Bayesian analysis of the broadband X-ray spectrum of NGC 3982 the BXA algorithm version 2.9 with MultiNest nested sampling algorithm was used. The analysis was performed in the PyXspec interface applying PyMultiNest. To produce the plots in the appendix A the `multinest_marginals_fancy.py` script was used, downloaded from github of Johannes Buchner.

In the BXA analysis the models were applied in the same set-ups as for the modelling in the Xspec environment, as described in the section 2.3.3 with the same values of all the fixed parameters as described in section 3.2. For *XMM-Newton* data the used energy range is 0.3 – 10.0 keV if not stated otherwise while for *NuSTAR* data it is 3 – 78 keV applicable throughout the entire work. Generally the defined priors of the fitted parameters were described either as a Jeffreys prior corresponding to a loguniform prior, a uniform prior or the photon index was defined using the Gaussian prior with mean value of 2 and standard deviation of 0.1 (as justified by Ricci et al., 2017b). The rest of fitted parameters was defined in the following way: Jeffreys or logarithmic prior was used for the `apec` temperature kT and normalization, column density if not stated otherwise, normalization of the power-law, fraction of the reflection component and for the pexrav model also for the normalization of the Gaussian line of `zgauss` component. Additionally, as the relative reflection parameter `rel_refl` in the pexrav model was assumed to acquire only negative values, a new prior needed to be defined. This was chosen to be a negative Jeffreys prior corresponding to a loguniform prior with an additional sign-inversion transformation. Finally, a uniform prior was applied for cosine of the inclination angle.

As the column density in the borus02 model is already defined in the logarithmic form, a uniform prior was used for this parameter as well as for the covering

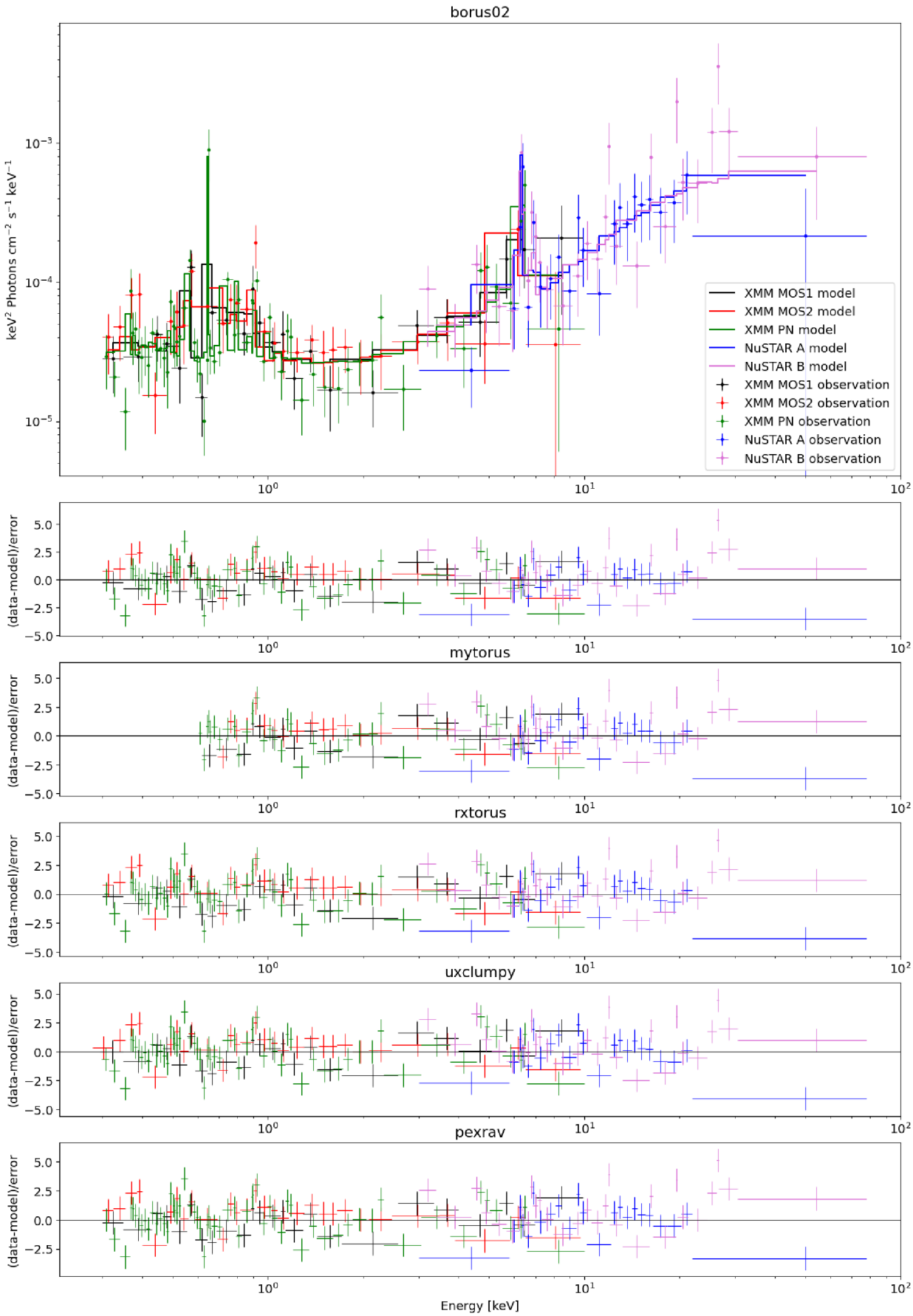

Figure 3.4: Unfolded X-ray spectrum of NGC 3982 as fitted by different spectral models with corresponding residuals.

Table 3.4: All best-fit parameters from the XSPEC manual modelling. Displayed parameters are following: column (1): name of the model and corresponding set-up, borus02 c. stands for the coupled mode while borus02 d. stands for decoupled mode; column (2): temperature of the collisionally-ionized diffuse gas of the `apec` component; column (3): normalization of the `apec` component; column (4): photon index of the power-law; column (5): normalization of the power-law; column (6): equatorial column density of the obscurer; column (7): line-of-sight column density of the obscurer; column (8): relative reflection forced to the negative values; column (9): cosine of the inclination angle; column (10): covering factor of the obscurer, for UXCLUMPY it corresponds to the torus σ (`TORsigma`) parameter while for MYTORUS and RXTORUS it corresponds to fraction r/R; column (11): CTK covering factor (`CTKcover`) for the UXCLUMPY model; column (12): fraction of the scattering emission and column (13): normalization of the Kα line of the `zgauss` model component used in the PEXRAV set-up. The values labelled with [a] are pegged to the upper hard limit while parameters labelled with [b] were frozen for the fitting or are fixed for the model such as the covering factor given by r/R for MYTORUS.

model (1)	kT [keV] (2)	$K_{\rm apec}$ [keV/cm^2/s] (3)	Γ (4)	$K_{\rm pl}$ [keV/cm^2/s] (5)	$\log N_{\rm H,eq}$ [cm^{-2}] (6)	$\log N_{\rm H,los}$ [cm^{-2}] (7)	R_{rel} (8)	$\cos i$ (9)	$f_{\rm C}$ (10)	$C_{\rm CTK}$ (11)	$f_{\rm scat}$ (12)	$K_{\rm Fe\ K\alpha}$ [keV/cm^2/s] (13)
pexrav	0.28	2.66×10^{-5}	2.03	2.32×10^{-4}	27.00[a]		-3.05	0.93			1.00×10^{-1}	2.30×10^{-6}
borus02 c.	0.27	2.63×10^{-5}	1.95	2.56×10^{-2}	25.50			0.15	0.19		9.76×10^{-4}	
borus02 d.	0.28	2.49×10^{-5}	2.00	2.63×10^{-1}	25.50	27.00[a]		0.05[b]	0.10		9.89×10^{-5}	
mytorus	0.38	1.55×10^{-5}	2.25	4.53×10^{-3}	25.00[a]			0.45	0.50[b]		5.36×10^{-3}	
uxclumpy	0.26	2.67×10^{-5}	2.00	6.39×10^{-3}		25.85		0.34	0.98	0.17	8.33×10^{-3}	
rxtorus	0.28	2.65×10^{-5}	2.30	3.90×10^{-3}	25.00[a]	24.82		0.32	0.43		5.83×10^{-3}	

[a] Pegged to the upper limit.
[b] Fixed for the fitting.

factor of the torus and cosine of the inclination angle. In the decoupled mode a Jeffreys prior was defined for column density of the `zphabs` component. Regarding that MYTorus model is defined only from 0.6 keV above, the *XMM-Newton* data were used in the energy range 0.6 – 10.0 keV unlike the rest of tested models that were used in both 0.3 – 10.0 keV and 0.6 – 10.0 keV bands. Also a new cosine prior needed to be user-defined for the inclination angle in both MYTorus, UxClumpy and RXTorus models as well as for the `TORsigma` parameter. A uniform prior was used for the CTK covering factor (`CTKcover`, C_{CTK}) in the UxClumpy model and for the covering factor given by the fraction r/R in the RXTorus model.

The inferred estimates of the posterior mean values and their errors for all fitted parameters and all models are summarized in the table 3.6. The model posterior realizations are visualized in figures 3.5 and 3.6. Intrinsic luminosity estimates are in the table 3.5. The total C value against the number of degrees of freedom for the local modelling with Xspec and the log-likelihood for the best fit from BXA for all models are displayed in the table 3.7. The posterior distributions are plotted in the appendix A.

model (1)	$\log L_{2-10\ \mathrm{keV}}$ [erg s^{-1}] (2)	$\log \lambda_{\mathrm{Edd}}$ (3)
pexrav	$41.46^{+0.86}_{-0.73}$	$-2.10^{+0.87}_{-0.72}$
borus02 c.	$40.91^{+0.16}_{-0.11}$	$-2.63^{+0.20}_{-0.17}$
borus02 d.	$42.07^{+0.25}_{-0.19}$	$-1.47^{+0.26}_{-0.26}$
mytorus	$41.29^{+0.10}_{-0.08}$	$-2.26^{+0.15}_{-0.15}$
uxclumpy	$41.40^{+0.12}_{-0.11}$	$-2.14^{+0.16}_{-0.16}$
rxtorus	$41.57^{+0.16}_{-0.15}$	$-1.97^{+0.20}_{-0.18}$

Table 3.5: Column (2) shows the inferred 50th quantile of the intrinsic luminosity in the 2 – 10 keV band. Column (3) shows the 50th quantile of the inferred Eddington ratio. Column (4) shows the equivalent width of the Fe Kα line in electron-volts. All uncertainties indicate the 16th and 86th quantile.

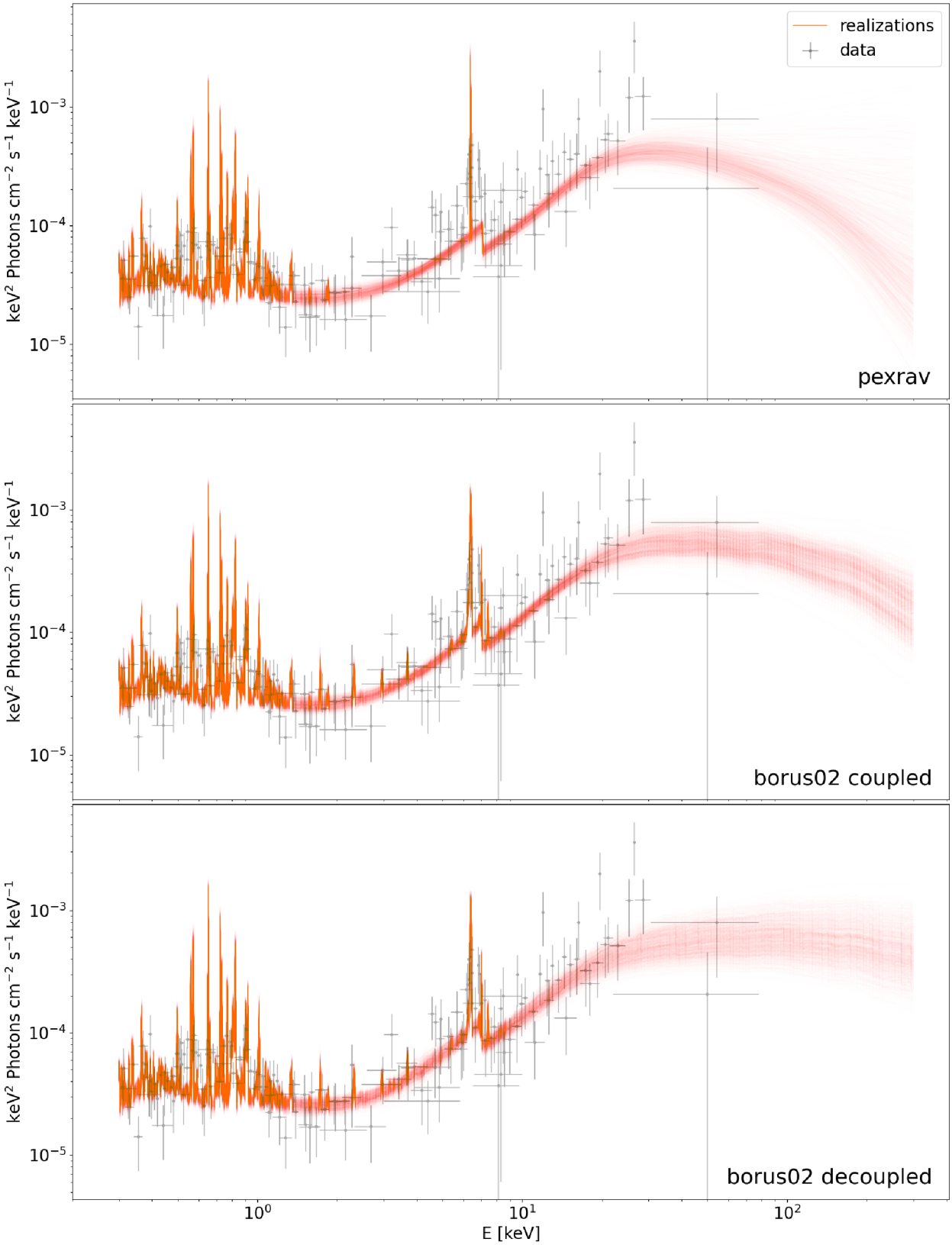

Figure 3.5: Model realizations for PEXRAV and BORUS02 both coupled and decoupled modes unfolded with simple power-law.

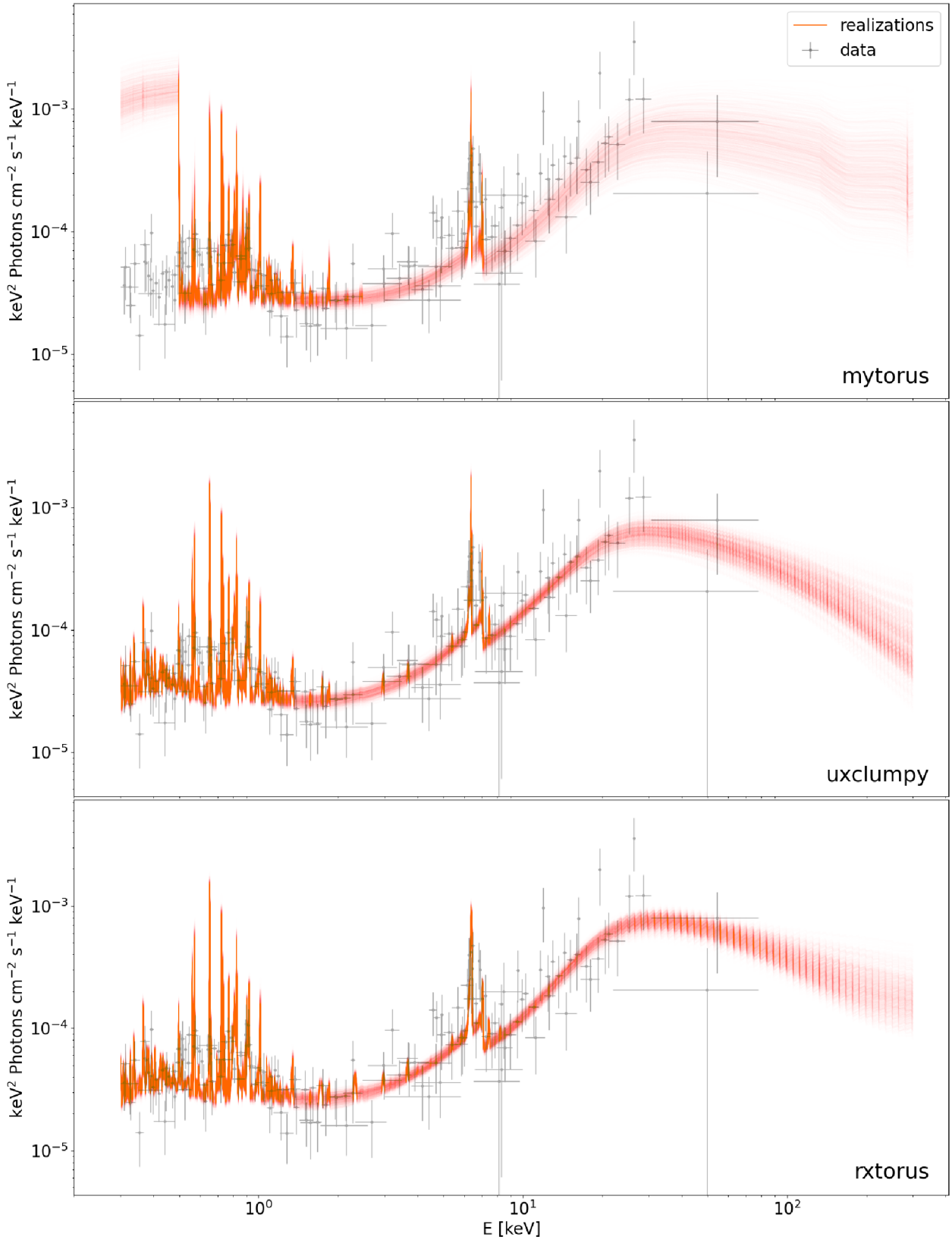

Figure 3.6: Model realizations for MYTorus, UxClumpy and RXTorus models unfolded with simple power-law.

Table 3.6: The posterior mean values for the fitted parameters obtained from BXA modelling. The columns representation is the same as for the table 3.4, the borus02 c. corresponds to the coupled model while borus02d to the decoupled mode. Values labelled with [a] have the corresponding uncertainty labelled with [u] unconstrained as the parameter is pegged to the hard limit and [b] means that the parameter was fixed during the modelling. The uncertainties correspond to 95% (2σ) confidence range. The line-of-sight column density for the RXTorus model was calculated according to the relation 2.15.

model (1)	$\log kT$ [keV] (2)	$\log K_{\rm apec}$ [keV/cm^2/s] (3)	Γ (4)	$\log K_{\rm pl}$ [keV/cm^2/s] (5)	$\log N_{\rm H,eq}$ [cm^{-2}] (6)	$\log N_{\rm H,los}$ [cm^{-2}] (7)	$-\log R_{rel}$ (8)	$\cos i$ (9)	$f_{\rm C}$ (10)	$C_{\rm CTK}$ (11)	$\log f_{\rm scat}$ (12)	$\log K_{\rm Fe\ K\alpha}$ [keV/cm^2/s] (13)
pexrav	$-0.55^{+0.05}_{-0.04}$	$-4.35^{+0.07}_{-0.09}$	$1.96^{+0.17}_{-0.15}$	$-2.61^{+1.26}_{-1.01}$	$25.24^{+0.72}_{-0.93}$		$-0.73^{+1.07}_{-1.20}$	$0.73^{+0.25}_{-0.46}$			$-2.06^{+1.01}_{-1.26}$	$-5.66^{+0.15}_{-0.20}$
borus02 c.	$-0.55^{+0.04}_{-0.04}$	$-4.37^{+0.08}_{-0.10}$	$1.95^{+0.16}_{-0.14}$	$-3.15^{+0.39}_{-0.25}$	$25.06^{+0.42}_{-0.70}$			$0.76^{+0.18}_{-0.38}$	$0.51^{+0.30}_{-0.33}$		$-1.48^{+0.26}_{-0.40}$	
borus02 d.	$-0.55^{+0.05}_{-0.04}$	$-4.37^{+0.08}_{-0.10}$	$1.98^{+0.16}_{-0.16}$	$-1.98^{+0.47}_{-0.89}$	$24.96^{+0.51}_{-1.84}$	$24.79^{+0.20}_{-0.41}$		0.05^{b}	$0.14^{+0.37}_{-u}$		$-2.66^{+0.90}_{-0.46}$	
mytorus	$-0.44^{+0.18}_{-0.08}$	$-4.54^{+0.12}_{-0.17}$	$1.89^{+0.18}_{-0.16}$	$-2.82^{+0.19}_{-0.13}$	$24.97^{+u}_{-0.11}$			$0.40^{+0.06}_{-0.10}$	0.5^{b}		$-1.81^{+0.15}_{-0.20}$	
uxclumpy	$-0.55^{+0.05}_{-0.04}$	$-4.37^{+0.08}_{-0.10}$	$2.03^{+0.15}_{-0.15}$	$-2.61^{+0.29}_{-0.28}$		$25.35^{+0.61}_{-0.70}$		$0.51^{+0.46}_{-0.48}$	$0.49^{+0.39}_{-0.34}$	$0.24^{+0.22}_{-0.13}$	$-1.10^{+0.49}_{-0.46}$	
rxtorus	$-0.55^{+0.05}_{-0.04}$	$-4.38^{+0.07}_{-0.09}$	$2.00^{+0.02}_{-0.02}$	$-2.47^{+0.32}_{-0.27}$	$24.95^{+u}_{-0.15}$	24.79		$0.34^{+0.26}_{-0.19}$	$0.47^{+0.23}_{-0.24}$		$-2.18^{+0.29}_{-0.32}$	

[b] Fixed for the modelling.

[u] Uncertainty unconstrained as the fit is pegged to the hard limit.

model (1)	C/d.o.f. (2)	log-likelihood (3)
pexrav	2336.17/2852	-1167.68
borus02 c.	2333.64/2852	-1166.20
borus02 d.	2335.38/2852	-1166.05
mytorus	2242.65/2783	-1124.04
uxclumpy	2283.30/2806	-1166.57
rxtorus	2333.95/2852	-1166.53

Table 3.7: For all the models listed in column (1), the column (2) shows the C-value over the number of degrees of freedom for the local modelling done in XSPEC while the column (3) displays the maximum negative log likelihood for the best-fit performed by BXA.

3.3.1 Model dependent degeneracies

The BXA model posterior distributions were used for the visualization of the model dependent degeneracies and key parameter estimations. The model dependent degeneracies are showing the differences between the distributions of parameters between the individual models. As the models assume different and unique geometries, the model dependent degeneracies are a good estimates of a geometry dependent degeneracies.

At first the intrinsic X-ray luminosity was estimated in the $2-10$ keV band from the posterior distributions using the equation 2.16. Figures 3.7 and 3.8 are showing the model dependent degeneracies of X-ray luminosity as a function of the column density of the torus. For comparison the estimated X-ray luminosities of the AGN in NGC 3982 from the optical and MIR observations are plotted as a horizontal regions representing the 16th and 84th quantile of the distributions. The relation between MIR and X-ray luminosity of an ANG is well known (Elvis et al., 1978; Glass et al., 1982; Krabbe et al., 2001; Lutz, D. et al., 2004; Ramos Almeida et al., 2007) and is given as follows

$$\log \nu L_{12\mu\mathrm{m}} = \alpha \log L_{2-10\ \mathrm{keV}} + \beta. \tag{3.1}$$

The $2-10$ keV band luminosity traces the accretion disk while the 12μm luminosity is linked to the emission of the dusty torus. Gandhi et al., 2009 reported the values of the parameters $\alpha = 1.11 \pm 0.07$ and $\beta = -4.37 \pm 3.08$ using a sample of 42 AGN, with a median $z = 0.1$ and a range of MIR luminosities of $\log \nu L_{12\mu\mathrm{m}} = 41.4 - 44.6$.

In this work we adopted the relation from Asmus et al., 2015 who reported the following MIR-versus-X-ray luminosity correlation

$$\log\left(\frac{L_{12\mu\mathrm{m}}}{10^{43}\ \mathrm{erg\ s^{-1}}}\right) = (0.97 \pm 0.03)\log\left(\frac{L_{2-10\ \mathrm{keV}}}{10^{43}\ \mathrm{erg\ s^{-1}}}\right) + (0.33 \pm 0.04). \tag{3.2}$$

The value of the nuclear MIR luminosity of NGC 3982, $\log L_{12\mu\mathrm{m}} = 41.56 \pm 0.06$, was also taken from Asmus et al., 2015 and the estimated X-ray luminosity from the MIR-versus-X-ray luminosity correlation is

$$\log L_{2-10\ \mathrm{keV}} = 41.17^{+0.09}_{-0.10}\ \mathrm{erg\ s^{-1}}.$$

The relation X-ray-versus-[O III] λ5007 luminosity is also well explored and shows the connection between the accretion disc emission and the emission of the partially ionized NLR up to kiloparsec scales (Ward et al., 1988; Panessa et al., 2006; González-Martín et al., 2009). The correlation is given by the formula

$$\log L_{2-10\ \mathrm{keV}} = \alpha \log L_{[\mathrm{O\ III}]} + \beta. \tag{3.3}$$

The values of $\alpha = 1.23 \pm 0.05$ and offset of $\beta = -12 \pm 2$ were adopted from Berney et al., 2015 while the [O III] λ5007 luminosity of NGC 3982 $\log L_{[\mathrm{O\ III}]} = 40.50$ corrected for Galactic absorption and NLR extinction was adopted from Panessa et al., 2006. From the given X-ray-versus-[O III] λ5007 luminosity the derived $2-10$ keV luminosity is

$$\log L_{2-10\ \mathrm{keV}} = 42.67^{+2.41}_{-2.29}\ \mathrm{erg\ s^{-1}}.$$

Further the bolometric luminosity and Eddington luminosity of NGC 3982 were calculated for the Eddington ratio estimation following the relations 2.17, 2.18 and 2.19. For the bolometric luminosity calculation the X-ray bolometric correction factor $\kappa_{\mathrm{bol}} = 1.44 \pm 0.12$ was adopted from Brightman et al., 2017. For the Eddington luminosity calculation the central SMBH mass $\log M_{\mathrm{BH}} = 6.89\ M_{\odot}$ was adopted from Kammoun et al., 2020 and an uncertainty of 0.5 dex was applied for the Eddington luminosity estimation. Figure 3.9 shows the 2D contour between the Eddington ratio and the column density of torus. A prominent boundary is notable showing that for higher Eddington ratios the column density needs to be above a certain level. This is consistent to strong radiation pressure in case of higher Eddington ratios that can blow away the material in the torus. However, for higher column density the torus is thicker and denser and can survive even in systems with higher Eddington ratios because it is more difficult to blow it away.

Figures 3.10 and 3.11 are showing the Eddington ratio dependency of the covering factor and the scattering fraction as a function with the covering factor,

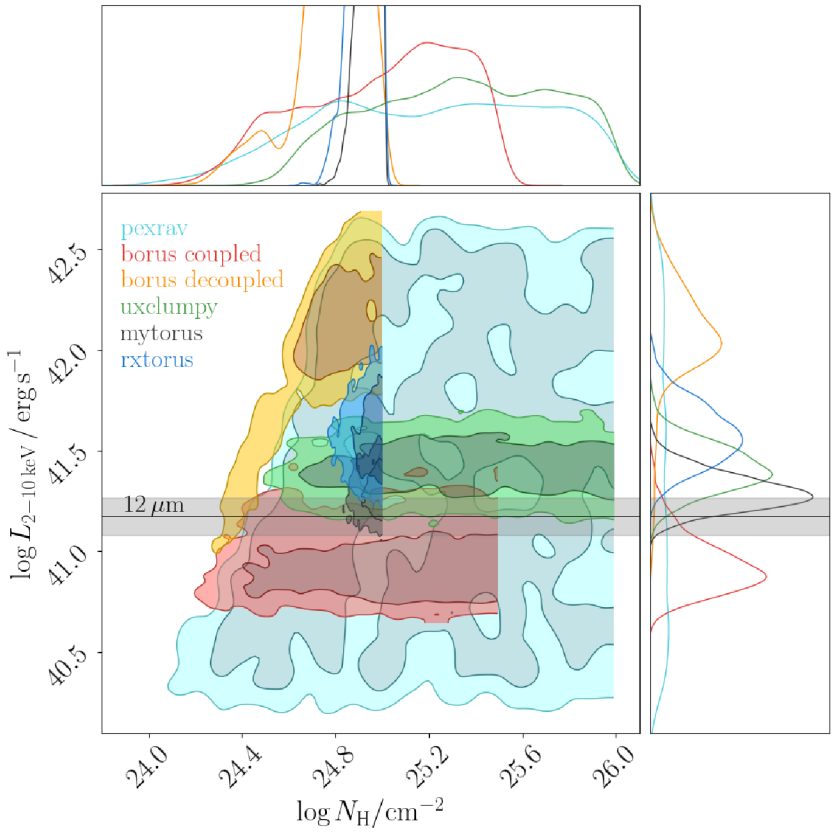

Figure 3.7: Corner plot showing the relation between the X-ray luminosity in the $2-10$ keV band in ergs per second and the logarithm of the column density of the obscurer for all models applied, drew by different colors. The contours correspond to 1σ and 2σ uncertainty estimates. Black solid line shows the 50th quantile of the X-ray luminosity of NGC 3982 as calculated from the relation between the MIR and X-ray luminosity of an AGN (relation 3.2) using MIR luminosity from Asmus et al., 2015. The shaded region shows the 16th and 84th quantiles.

respectively. The red dashed line in figure 3.10 represents the effective Eddington limit for a dusty gas with $N_{\mathrm{H}} = 10^{22}$ cm^{-2} (Ricci et al., 2017c). Above this limit the clouds of dusty gas cannot survive in the system in the long terms, as they are blown away by strong radiation pressure. Generally, increasing radiation pressure with the increasing Eddington ratio in dusty gas systems results in decreasing covering factor of the torus. Material at higher angles from the orbital plane is easier blown away than the denser and thicker environment in the orbital plane of the system. Thus for high Eddington ratios even above the Eddington limit for a dusty gas shown by the red dashed line the torus covering factor necessarily decreases. Figure

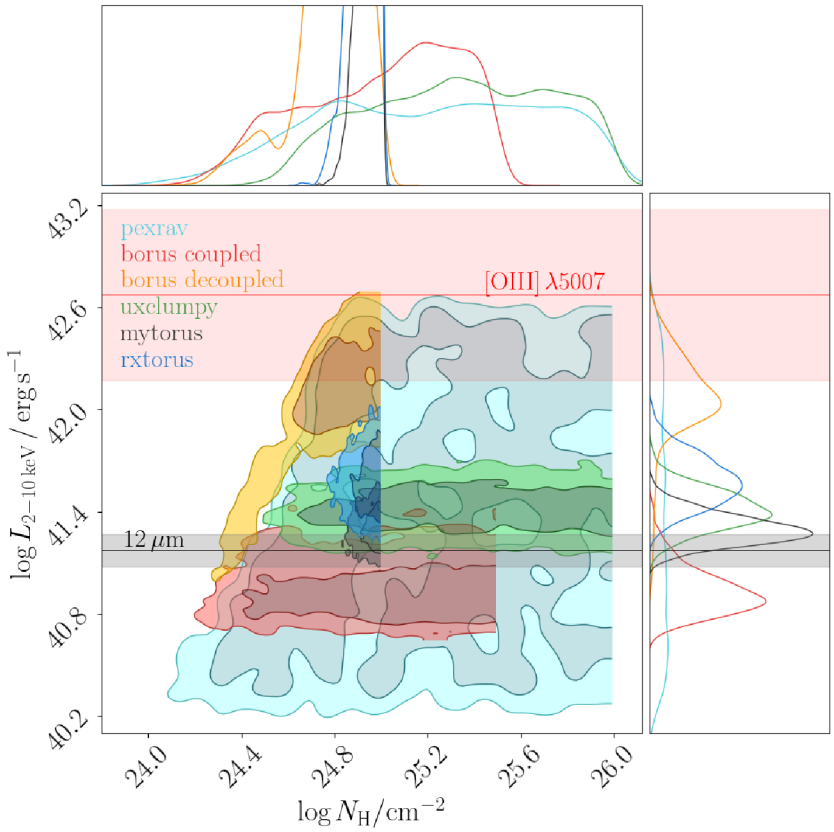

Figure 3.8: Equivalent corner plot as in the figure 3.7 but showing the X-ray luminosity of NGC 3982 as derived from relation 3.3 between the X-ray luminosity in the 2 – 10 keV band and the optical one corresponding to emission of [O III] λ5007 line tracing the NLR. The [O III] luminosity corrected for Galactic absorption and NLR extinction was adopted from Panessa et al., 2006. Red solid line shows the 50th quantile while the red-ish shaded region corresponds to the 16th and 84th quantile of the distribution.

3.10 proves this relation especially with the BORUS02 decoupled model distribution showing very small covering factors for high Eddington ratios. A weak relation is notable also from the contours of other models that have covering factor as a free parameter as well as from the high covering factor tail of BORUS02 decoupled distribution, with covering factor slightly decreasing for increasing Eddington ratios.

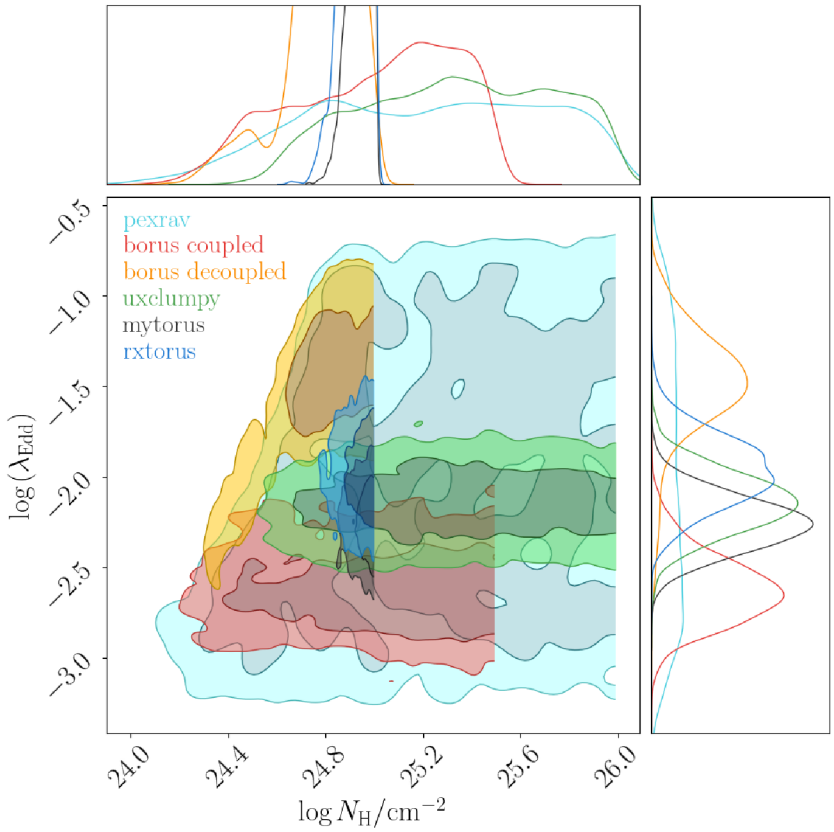

Figure 3.9: A corner plot showing the relation between the logarithm of Eddington ratio and the logarithm of the column density. Each model is drew by different color with contours showing the 1σ and 2σ estimates.

3.3.2 Model comparison

One of the advantages of BXA is that it can be used for model comparison with the Bayesian evidence. For the model comparison all models needed to be fitted in the same energy range. As MYTorus model is defined from 0.6 keV, all the remaining models were fitted in the energy range 0.6 – 78.0 keV. Script `model_compare.py` was adopted from github of Johannes Buchner. The Bayesian evidence $\log \mathcal{Z}$ is normalized to the highest value corresponding to the best performing and most likely model. It shows the probability of the likelihood of each model relative to the other are shown in the table 3.8. The model with the highest evidence is the most probable one, while the probability of the worse performing models is $\mathcal{Z}$ times less likely than the first-best model. In order to compare models in the full energy range a second comparison was performed without MYTorus model, with

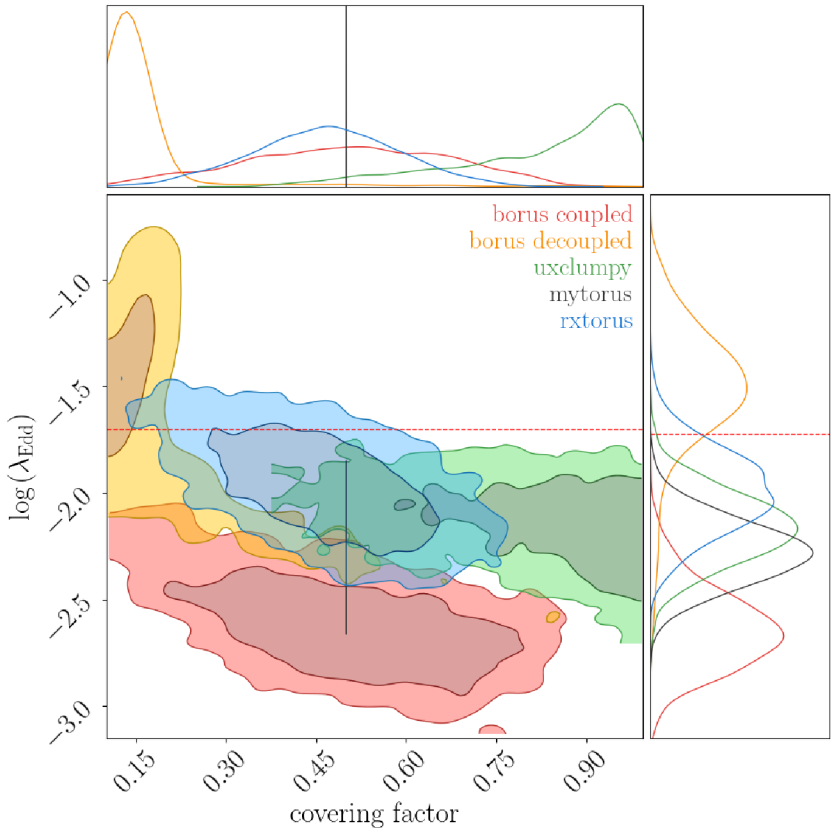

Figure 3.10: A corner plot showing the logarithm of the Eddinton ratio versus the covering factor of the obscurer. It can be seen that the covering factor is rather poorly estimated for most of the used models. The MYTorus model has covering factor fixed, so the distribution is shown as a vertical line indicating only the corresponding range of Eddington ratios. The red dashed line represents the effective Eddington limit for a dusty gas.

lower energy limit 0.3 keV. The comparison is in the table 3.8.

MYTorus model shows to be least likely among all applied models, however, it was used with the least number of free parameters as it was applied in the coupled mode. As a consequence, the possible spectral shapes reproducible by this model is decreased and the model performance is worse. On the other hand, the pexrav was found to be the third-best model with 0.06 times less likely than the best performing UxClumpy model. As the reflection component in not linked to the obscurer in pexrav, the model is efficiently capable of reproducing any spectral shapes even though the parameter estimates might not be reasonable as the reprocessor assumption is not physical. The best performing model was found to be

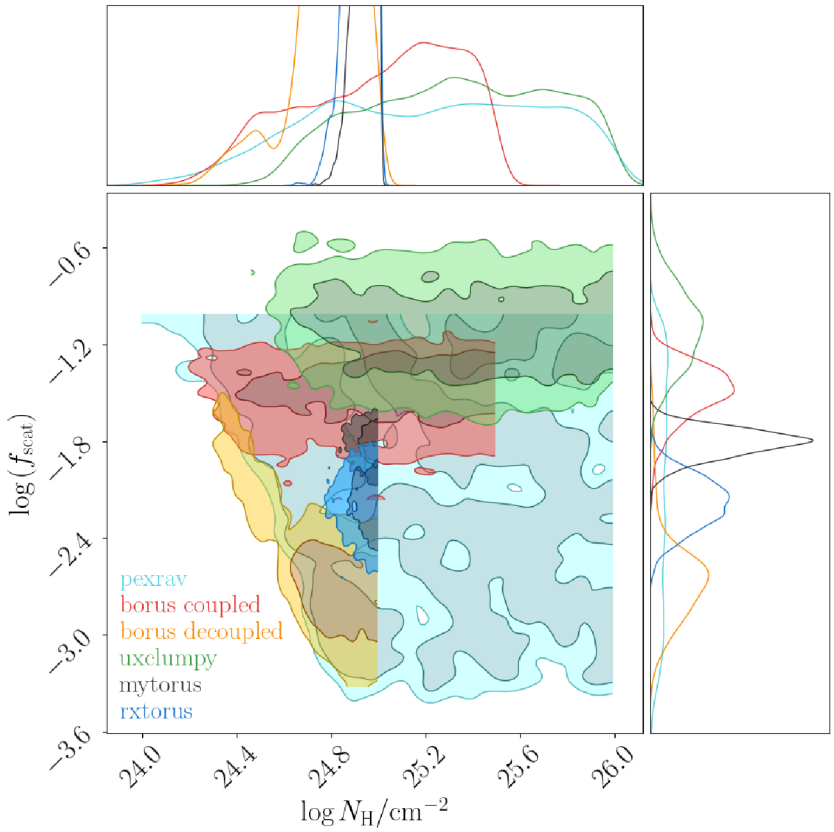

Figure 3.11: A corner plot showing the scattering fraction vs. the column density.

Table 3.8: Comparison of the models applied to the broadband spectrum of NGC 3982 with MYTorus in energy range 0.6 – 78.0 keV (*left*) and without MYTorus in energy range 0.3 – 78.0 keV (*right*).

model	log $\mathcal{Z}$
mytorus	−4.5
borus02 decoupled	−2.1
rxtorus	−1.3
pexrav	−1.2
borus02 coupled	−0.1
uxclumpy	0.0

model	log $\mathcal{Z}$
borus02 decoupled	−2.1
pexrav	−1.5
rxtorus	−1.2
borus02 coupled	−0.3
uxclumpy	0.0

UxClumpy. This model not only assumes the most reasonable physical geometry of the obscurer, which is clumpy, but also with two separate reflectors is very efficient in reproducing the studied spectral shape.

4 Discussion and Future prospects

4.1 Modelling method comparison

As the modelling of the broad X-ray spectrum of NGC 3982 was approached by two distinct methods; locally with Xspec spectral fitting package using Levenberg-Marquardt algorithm and by using BXA connecting the spectral fitting package to nested sampling algorithms, the comparison of these methods is convenient. For this purpose, the following approach was selected.

The BXA posterior distribution of each model was used for the initial guess of the parameter values for further modelling. This was done in two different ways.

1. A range from 99% quantile of the posterior distributions for each fitted parameter were defined. A random value within the specified ranges was selected for the initial guess of the fitted parameters, for each parameter separately. The spectrum was consequently fitted while the randomly chosen values were saved along with the final best-fit values and Poisson likelihoods. The process was repeated in a loop for the same amount of times as there are posterior samples in the BXA output file for each model.

2. Each posterior sample (corresponding to a row in the output files of BXA) was used for the initial guess of the parameter values and consequently fitted. The initial values for each fitting loop are forming a set of best-fit values for each parameter and are coming directly from the Bayesian analysis as the parameter estimates. The final best-fit values are saved in each loop.

Consequently the parameter estimates from the Bayesian analysis were compared to the best-fit values from the local modelling in Xspec. As from Xspec local modelling only the most probable value can be estimated and not a complex distribution, such comparison is only a rough approximation. Parameter uncertainties were not estimated for computational efficiency. Figure 4.1 shows the EW of Kα line distribution comparison between the applied methods. Consequently, figures 4.2 to 4.7 show the distribution of the intrinsic X-ray luminosity in the $2-10$ keV band. The left-hand sub-figure always shows the first comparison method when the initial

guess of the parameter for the local modelling with XSPEC was chosen randomly from the posterior distributions using 99% BXA quantiles. The right-hand side sub-figure shows the second comparison method when each row of the BXA output file corresponding to a posterior sample was used as the initial parameter guess for the modelling in XSPEC.

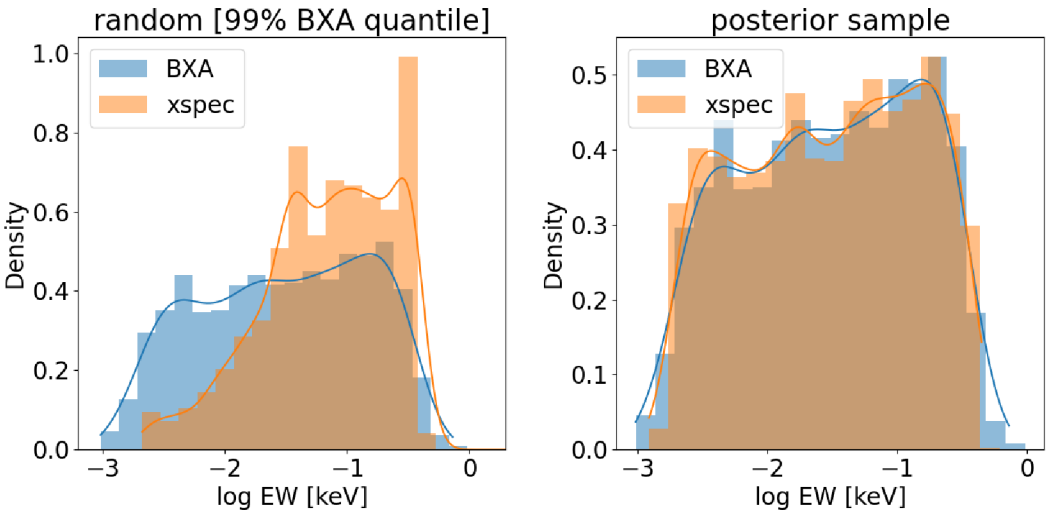

Figure 4.1: The equivalent width of Kα line distribution for PEXRAV model. The initial parameter guess for the local modelling in XSPEC was drawn randomly from the 99% quantile distribution obtained by BXA (*left*) before the EW was derived. The enhancement is visible when the initial guess for all the parameters was drawn from the posterior sample directly (*right*).

It is clearly visible that choosing a posterior sample for the initial value estimates in the local modelling with XSPEC leads to similar and almost identical distributions of the estimated X-ray luminosities. In some cases (as for BORUS02 decoupled, UXCLUMPY or RXTORUS) the obtained parameter estimates from local modelling in XSPEC are evincing much more extended tails of the best-fit parameter distributions if the initial parameters are drawn randomly from the 99% BXA quantiles but are eliminated once the posterior samples are used for the initial parameter guesses. On the other hand, for MYTORUS the luminosity distribution from local modelling does not correspond to the distribution obtained from BXA even for the second modelling comparison and most probably is due to a local minima.

The comparison of the posterior distributions derived by BXA to the best-fit values obtained by local modelling with XSPEC for each parameter separately is shown in the appendix B. Red solid line shows the 99% quantile distribution of the initial parameter values for the XSPEC fitting.

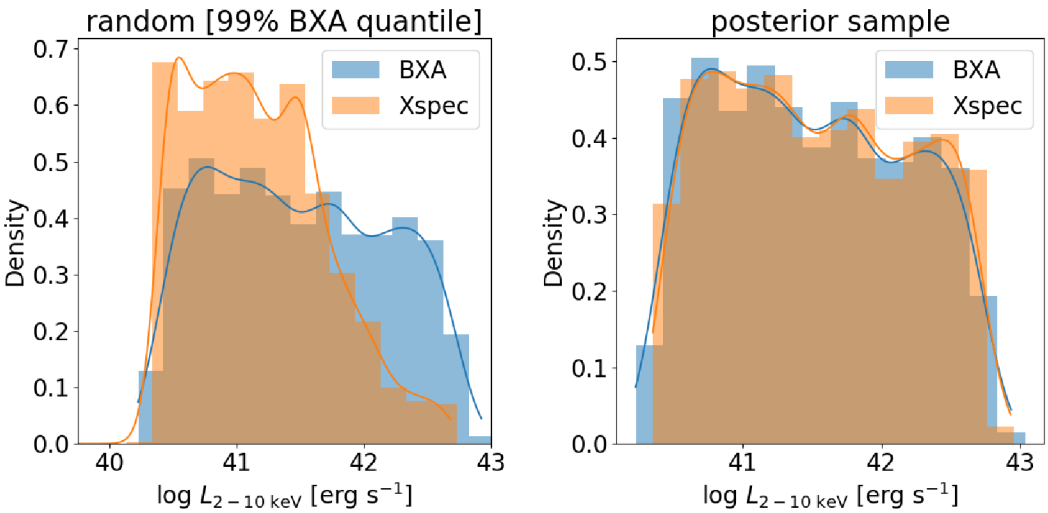

Figure 4.2: Distribution of the X-ray luminosity in 2 – 10 keV band for PEXRAV model and both modelling methods. For the fist comparison (*left*) accounts for randomly selected initial parameters for the local modelling in XSPEC while for the second comparison (*right*) the complex posterior samples were used for the initial parameters guess.

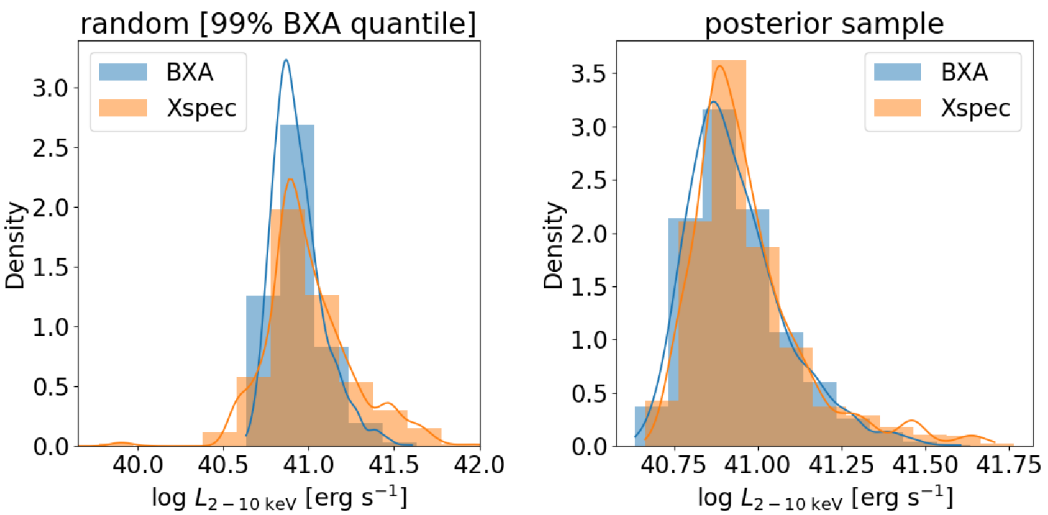

Figure 4.3: The same histogram as in the figure 4.2 but for BORUS02 model in the coupled mode.

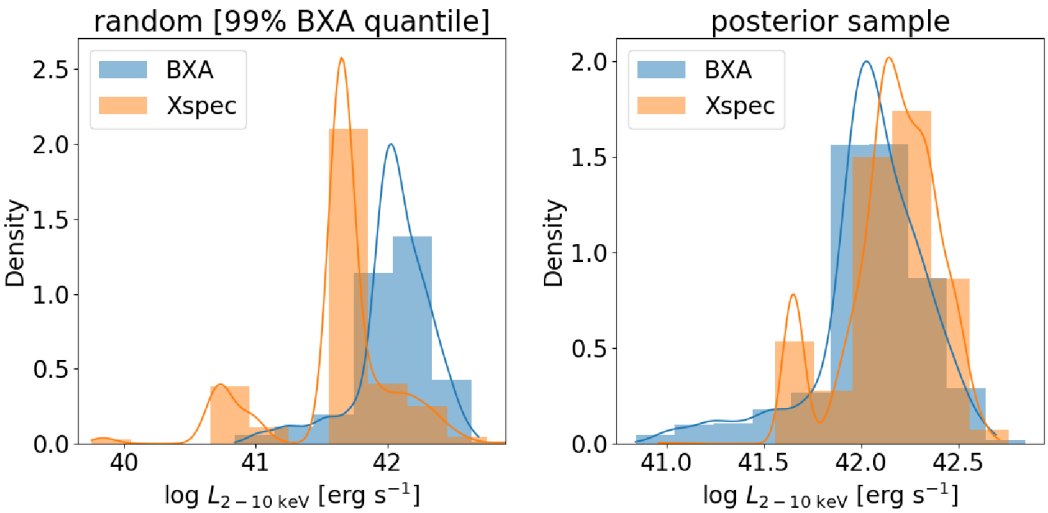

Figure 4.4: The same histogram as in the figure 4.2 but for BORUS02 model in the decoupled mode. The XSPEC distributions evince bimodal distribution due coming from a weak bimodality of both the photon index and the power-law normalization.

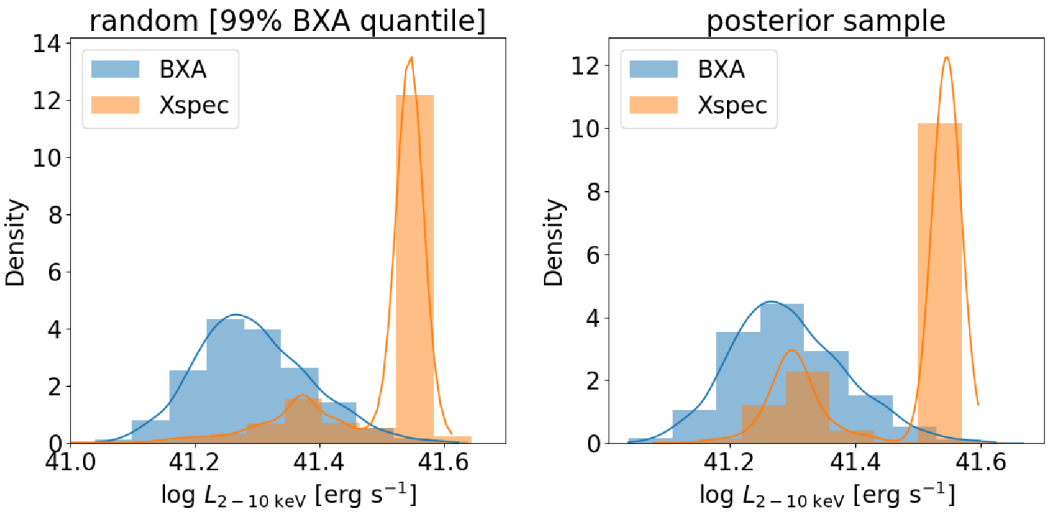

Figure 4.5: The same histogram as in the figure 4.2 but for MYTORUS model in the coupled mode. The bimodal distribution for XSPEC best-fit values comes from the fact, that both the power-law normalization and photon index evince such distributions, but stronger than in the BORUS02 decoupled model.

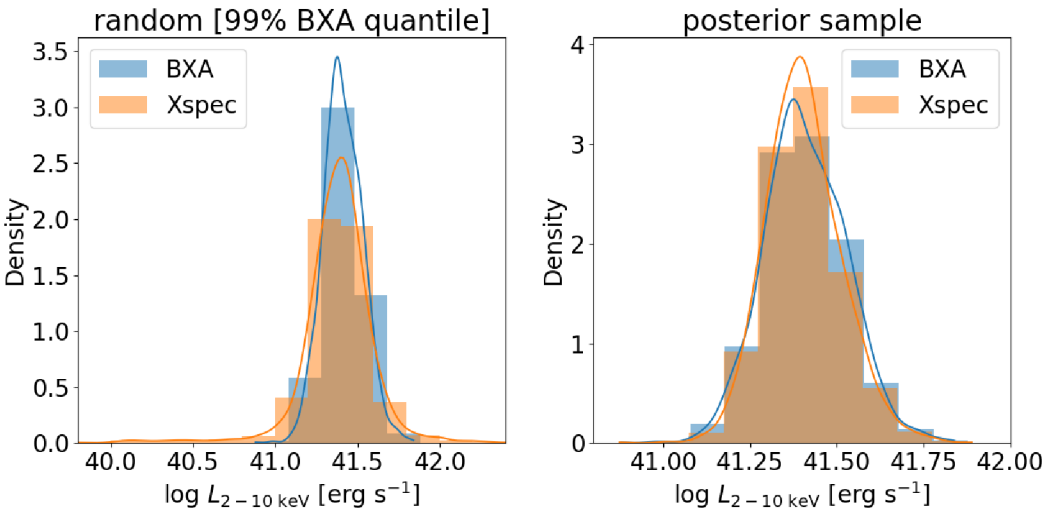

Figure 4.6: The same histogram as in the figure 4.2 but for UxClumpy model in the coupled mode. Notice how are the extended tails of the local modelling eliminated in the second comparison method.

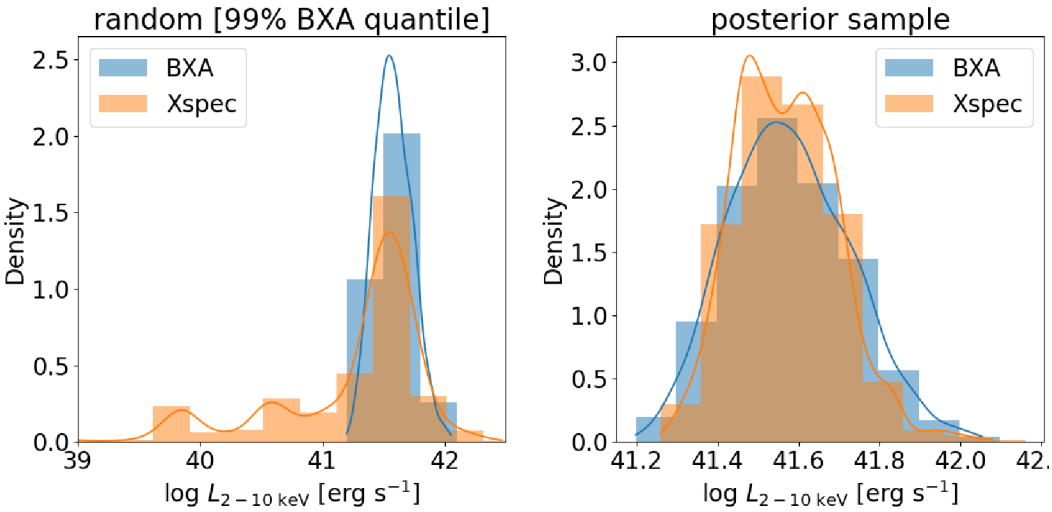

Figure 4.7: The same histogram as in the figure 4.2 but for RXTorus model in the coupled mode.

4.2 Different models

As multiple different models were fitted to the data the model comparison with Bayesian evidence was performed as described in the section 3.3.2. Due to different free parameter and different number of fitted parameters each model has different capability of reproducing the complex spectral shape and necessarily occupies different areas in the parameter spaces as shown in section 3.3.1. For the model comparison all models need to be fitted in the same energy range. As MYTorus model can be used only from 0.6 keV, all the models were used in energy range 0.6 – 78.0 keV.

The MYTorus model was used only in coupled mode with seven free parameters, one parameter less than in the rest of models. Moreover, the covering factor in this model is fixed to value 0.5 corresponding to half-opening angle of 60°, while the inclination angle was found to be slightly higher, 66°. Model realizations in figure 3.5 show a large dispersion between individual posterior realizations for the Compton hump and at higher energies but otherwise the model fits the observed data points adequately. It might be down to this dispersion and a fewer fitted parameters that MYTorus model was found to be as the least probable model. Regarding the `apec` component, table 3.6 shows that MYTorus is the only model with notably different values obtained for the `apec` temperature and normalization which is related to the fact that MYTorus is only applicable from 0.6 keV. The global column density was pegged to the upper hard limit of the parameter as showed by the corresponding corner plot in appendix A with the lowest found value of the photon index, $\Gamma = 1.89 \pm 0.2$.

The decoupled version of MYTorus model allows to model the line-of-sight and global column densities separately with the reflection component dependent on the inclination angle. This model set-up remains to be applied in the future work. Instead, for this work, the UxClumpy model assuming a clumpy geometry was applied, as it accounts for the line-of-sight column density and two different covering factors decoupled from each other. Unlike MYTorus, UxClumpy was found to be the best performing model according to both sub-tables in table 3.8. UxClumpy was modelled with nine free parameters with the highest photon index found among all models ($\Gamma = 2.03 \pm 0.15$), `TORsigma` parameter of 0.5 that would correspond to half-opening angle of 30° if approximated to covering factor, a inclination angle of 59° and the CTK covering factor of 0.24.

The same geometry as for MYTorus is assumed by the RXTorus model but with covering factor allowed to vary. Eight fitted parameters result in much better performance of RXTorus model with the used set-up compared to MYTorus. Unlike other models, RXTorus fits the global column density with the line-of-sight column dependent on inclination and the covering factor as given by the relation

2.15. The value of the covering factor obtained by BXA corresponds to half-opening angle of 62° with inclination angle 70°. Figure 3.6 shows how the shape of the Compton hump is much better constrained for RXTorus and UxClumpy if compared to MYTorus even despite notable differences.

The coupled version of the borus02 model has line-of-sight column density linked to the global one. This model set-up was found to be only slightly worse performing than the UxClumpy model, being the second-most likely model. With covering factor corresponding to half-opening angle of 59° it is the only model to find inclination angle smaller, 40°. This would suggest an unobscured source, however, in borus02 the line-of-sight component does not have any inclination dependence and high column obtained by BXA (10^{25} cm^{-2}) shows high absorption. Inclination angle smaller than the covering factor suggests that the spectrum is dominated by the reflection component even though it is unphysical due to how is the model built. In the decoupled mode the inclination angle was fixed to 87° for simplicity as the line-of-sight column density of the `zphabs*cabs` component was fitted. It is important to state that the column density of these components has no inclination dependence. However, the performance of the decoupled version of the model is worse than the coupled mode as notable also from the realizations in the figure 3.5 as the constrains on the shape of the Compton hump are worse for the decoupled borus02 model and by the model comparison it was found to be one of the worst performing models.

For pexrav model it is important to say that the reflection component is decoupled from the column density, but with nine free parameters the model is successful in reproducing the spectral shape of the studied broadband spectrum.

4.3 Future work

High spectral resolution data probing the polar dust

This work analyses the broad X-ray spectrum of an heavily obscured AGN with assumption of a circumnuclear obscurer as the source of the X-ray absorption and reprocessed emission of the central radiation emerging from the very central parts of the system in hot corona. The torus in obscured AGN also absorbs and reprocesses the optical/UV emission produced in the accretion disc and re-emits it in the IR wavelengths, being bright more particularly in the MIR part of the electromagnetic spectrum. However, recent studies have shown an extended dusty structures perpendicular to the torus plane in the polar regions at scales from tens to hundreds of parsecs, bright in MIR and present especially in obscured AGN (Hönig et al., 2012; Tristram et al., 2014). Such observations indicate that the torus is not the only structure acting as a reprocessor, even though most studies on

reprocessed X-ray radiation in AGN do not assume any polar component (McKaig et al., 2022). The origin of the polar gas/dust is still unknown, but it has been suggested that it could be a result of radiation pressure on the dust grains from strong UV emission from the accretion disc in the polar direction causing a dusty wind (Ricci et al., 2017a; Leftley et al., 2019; Hönig, 2019; Venanzi et al., 2020). The polar dusty gas is most likely optically thin, thus has a significant effect on the soft part of the X-ray spectrum, leading to increase of EW of fluorescent lines in 0.3 – 5.0 keV band (McKaig et al., 2022). As suggested by Liu et al., 2019, adding a polar component in the study of the scattered X-ray emission in the soft band can help us understand the kinematics of the polar gas and thus its origin. The polar component is also needed in order to explain the observed MIR properties of obscured AGN.

To include a polar component to our analysis, a high spectral resolution soft X-ray data would be needed. Future observations of NGC 3982 by *XRISM* mission (XRISM Science Team, 2020) would be very advantageous for further work.

Machine Learning for big data analysis

The analysis done in this work studies only one obscured AGN in details, focusing on the confirmation of its CTK nature. The search for heavily obscured sources is often difficult due to heavy absorption in X-rays, the one energy band crucial for CTK AGN identification. A Machine Learning (ML) project should be realized to determine multi-wavelength identifiers of obscured AGN. Such project would require a large sample of known obscured and unobscured AGN observed across the electromagnetic spectrum, in order to find specific spectral features characteristic for heavily obscured sources.

Goodness-of-fit

As the statistic used in this work assumes Poisson distribution, unlike for χ^2 using Gaussian distribution, the goodness of each fit cannot be determined directly. A Monte Carlo method for the goodness-of-fit estimation would be needed to be able to quantify the goodness-of-fit for any fit performed by BXA or locally in the Xspec environment. The approach would by based on simulation of a large amount of spectra with `fakeit` command in the PyXspec environment using the best fit model parameter values. Consequent fitting of the simulated spectra with the best fit model would be computationally and time-consuming, but could be performed on machines with larger amount of cores. In order to save computing time and space, it is possible to save only the output likelihoods (C-values) and the number of degrees of freedom from the comparison of the best-fit model to the simulated spectra. C-values can be consequently compared to the likelihood of the modelled

real spectrum. Such comparison would allow us to quantify the goodness-of-fit performed with statistic based on the Poisson likelihoods.

4.3.1 *HEX-P* simulations

High Energy X-ray Probe (*HEX-P*) is a next generation X-ray observatory concept with bandpass from 0.1 keV up to 150 keV proposed by Madsen et al., 2019. *HEX-P* will follow-up on heritage of *NuSTAR* but improving its sensibility 40 times in the 10 – 80 keV band and ~100 times improving the sensitivity of current capabilities in 80 – 150 keV band. With spatial resolution smaller than 10 arcsec FWHM and a large effective area *HEX-P* would become a unique astrophysical tool for the study of the hot Universe.

Publicly available[1] response files version 1 for two high energy telescopes (HET) on-board *HEX-P* were used for simulation of NGC 3982 spectra. The simulations were based on the best-fit model parameters of UxClumpy, as this physically-motivated model allows the varying of two different parameters describing the geometry of the obscurer. Three different values were applied for each of the parameters describing the geometry, `CTKcover` and `TORsigma` in order to make a grid of 9 spectra covering the full range of allowed geometries. For `TORsigma` a values of 7, 28 and 84°were used and for `CTKcover` were selected values 0.0, 0.3 and 0.6. An exposure of 100 ks for each HET detector was assumed, making the total exposure of 200 ks. The inclination angle was fixed to 70°.

In order to compare *NuSTAR* and *HEX-P* spectra of NGC 3982, a set of 9 *NuSTAR* spectra was simulated with identical initial parameters as for the simulation of *HEX-P* spectra. Figure 4.8 shows the comparison between the *NuSTAR* and *HEX-P* simulated spectra. The spectra were normalized to unity at 7.1 keV to show that for *HEX-P* an additional parameter needs to be accounted for to reproduce the variations in the spectral shape while for *NuSTAR* the changes can be achieved by varying the normalization of the primary component. Additionally, a sufficient sensitivity it the hard X-rays is needed in order to identify differences in the shape of the Compton hump.

Observatories such as the proposed *HEX-P* could bring a new light upon low-luminosity CTK AGN as NGC 3982. Figure 4.8 shows how powerful the instrument on board *HEX-P* would be, allowing us not only to study heavily obscured AGN in order to determine their column densities and intrinsic luminosities but also to much more precisely determine the physical properties of the circumnuclear obscurers.

[1] At https://hexp.org/.

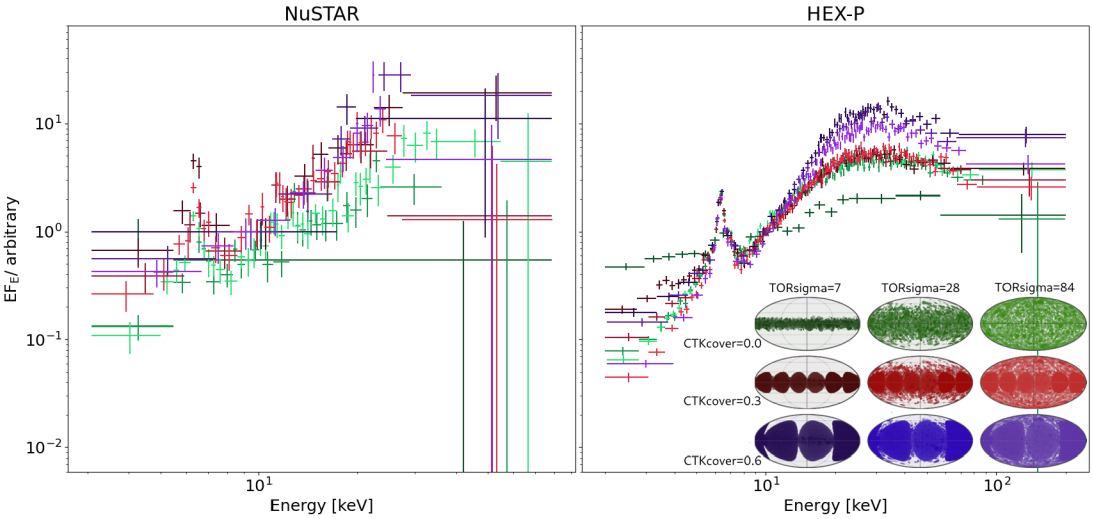

Figure 4.8: *NuSTAR* spectra simulated from the UxClumpy best-fit for NGC 3982 (*left*) using 100 ks per FPM but for three different combinations of `TORsigma` and `CTKcover` factor drew by different colors. Clearly the iron line and Compton-hump are well reproduced for each, but the effect with varying geometry is more difficult to constrain. Equivalent simulations for *HEX-P* (*right*) illustrate its potential for sensitive studies of the obscurer geometry in the lower- luminosity AGN population. The illustration on the bottom right demonstrates the UxClumpy geometry of the 9 simulated spectra for different combination of the `TORsigma` and `CTKcover` parameters.

Conclusion

This work gives a detailed analysis of the broadband X-ray spectra of an Seyfert 2 AGN NGC 3982 obtained by *XMM-Newton* and *NuSTAR* observatories in the soft and hard X-ray bands, respectively. Data analysis was pursued by two different approaches, at first the spectrum was modelled locally with the Xspec X-ray spectral fitting package where the initial parameter guess needs to be specified by the user. Secondly, a Bayesian X-ray Analysis (BXA), connecting the spectral fitting software like Xspec to nested sampling algorithms was used for the data analysis.

Several different physically-motivated state-of-art AGN obscurer models were used for the spectra modelling assuming different and unique geometries of the obscuring torus. borus02 model assuming a spherical geometry with polar cutouts defined by the covering factor parameter with uniform density was used in coupled and decoupled mode, both finding equatorial column density $\sim 10^{25}$ cm^{-2} but about an order higher X-ray luminosity and Eddington ratio for the decoupled mode. MYTorus and RXTorus assume toroidal geometry of the obscurer with uniform density of the material while RXTorus allows covering factor to vary unlike MYTorus model. The coupled MYTorus was found to be the least probable model but with the smaller number of fitted parameters, finding the second lowest value for both intrinsic luminosity and Eddington ratio. On the other hand, RXTorus predicts the second highest values for both parameters. The most probable model was found to be a model with complex clumpy geometry, UxClumpy, build up with a large number of clouds with different column densities distributed in a geometry given by two different parameters. UxClumpy predicts the intrinsic luminosity to be $10^{41.4}$ erg/s and Eddington ratio of 0.7%. It also confirms the CTK nature of NGC 3982 with line-of-sight column density of $10^{25.4}$ cm^{-2}. The empirically-motivated models were compared to a phenomenological reflection model largely used before the physical table models were available, pexrav.

The problem of the fit getting stuck in the local minima during the modelling in the Xspec was avoided by using BXA. These two methods were compared and the initial guess for the local fitting in Xspec was improved by starting within the global minimum. However, even when using posterior samples for the initial

parameters guess, the fit using the traditional Levenberg-Marquadt algorithm can still get stuck in local minimum. As various different models were applied and the key parameter estimates were compared, I show how distinct the results can be for the models and therefore one should be cautious in inferring parameter estimates while using only a single torus model.

By simulating *HEX-P* spectra of NGC 3982 I show the strengths of this future probe mission. Thanks to the combination of simultaneously observed broadband spectra it will be capable to disentangle multiple spectral components as well as it will have high sensitivity above 10 keV. Thanks to this, *HEX-P* will help us to constrain the geometrical and physical properties of the circumnuclear obscuring material even for low-luminosity population of obscured AGN.

Bibliography

Aird, J.; Coil, A. L.; Georgakakis, A.; Nandra, K.; Barro, G., et al., 2015. The evolution of the X-ray luminosity functions of unabsorbed and absorbed AGNs out to z~ 5. *Monthly Notices of the Royal Astronomical Society*. Vol. 451, no. 2, pp. 1892–1927. Available from doi: 10.1093/mnras/stv1062.

Akylas, A.; Georgakakis, A.; Georgantopoulos, I.; Brightman, M.; Nandra, K., 2012. Constraining the fraction of Compton-thick AGN in the Universe by modelling the diffuse X-ray background spectrum. *Astronomy & Astrophysics*. Vol. 546, A98. Available from doi: 10.1051/0004-6361/201219387.

Akylas, A.; Georgantopoulos, I., 2009. XMM-Newton observations of Seyfert galaxies from the Palomar spectroscopic survey: the X-ray absorption distribution. *Astronomy & Astrophysics*. Vol. 500, no. 3, pp. 999–1012. Available from doi: 10.1051/0004-6361/200811371.

Alexander, D. M.; Bauer, F. E.; Brandt, W. N.; Schneider, D. P.; Hornschemeier, A. E., et al., 2003. The Chandra Deep Field North Survey. XIII. 2 Ms Point-Source Catalogs. *The Astronomical Journal*. Vol. 126, no. 2, pp. 539–574. Available from doi: 10.1086/376473.

Ananna, Tonima Tasnim; Treister, Ezequiel; Urry, C. Megan; Ricci, C.; Kirkpatrick, Allison, et al., 2019. The Accretion History of AGNs. I. Supermassive Black Hole Population Synthesis Model. *The Astrophysical Journal*. Vol. 871, no. 2, p. 240. Available from doi: 10.3847/1538-4357/aafb77.

Anders, E.; Grevesse, N., 1989. Abundances of the elements: Meteoritic and solar. *Geochimica et Cosmochimica Acta*. Vol. 53, no. 1, pp. 197–214. Available from doi: 10.1016/0016-7037(89)90286-X.

Antonucci, R. R. J.; Miller, J. S., 1985. Spectropolarimetry and the nature of NGC 1068. *The Astrophysical Journal*. Vol. 297, pp. 621–632. Available from doi: 10.1086/163559.

Antonucci, Robert, 1993. Unified models for active galactic nuclei and quasars. *Annual Review of Astronomy and Astrophysics*. Vol. 31, pp. 473–521. Available from doi: 10.1146/annurev.aa.31.090193.002353.

Arnaud, K. A., 1996. XSPEC: The First Ten Years. In: Jacoby, George H.; Barnes, Jeannette (eds.). *Astronomical Data Analysis Software and Systems V*. Vol. 101, p. 17. Astronomical Society of the Pacific Conference Series.

Ashton, Greg; Bernstein, Noam; Buchner, Johannes; Chen, Xi; Csányi, Gábor, et al., 2022. Nested sampling for physical scientists. *arXiv e-prints*, arXiv:2205.15570. Available from arXiv: 2205.15570 [stat.CO].

Asmus, D.; Gandhi, P.; Hönig, S. F.; Smette, A.; Duschl, W. J., 2015. The subarcsecond mid-infrared view of local active galactic nuclei – II. The mid-infrared–X-ray correlation. *Monthly Notices of the Royal Astronomical Society*. Vol. 454, no. 1, pp. 766–803. issn 0035-8711. Available from doi: 10.1093/mnras/stv1950.

Asmus, D.; Greenwell, C. L.; Gandhi, P.; Boorman, P. G.; Aird, J., et al., 2020. Local AGN survey (LASr): I. Galaxy sample, infrared colour selection, and predictions for AGN within 100 Mpc. *Monthly Notices of the Royal Astronomical Society*. Vol. 494, no. 2, pp. 1784–1816. Available from doi: 10.1093/mnras/staa766.

Asmus, D.; Hönig, S. F.; Gandhi, P.; Smette, A.; Duschl, W. J., 2014. The subarcsecond mid-infrared view of local active galactic nuclei - I. The N- and Q-band imaging atlas. *Monthly Notices of the Royal Astronomical Society*. Vol. 439, no. 2, pp. 1648–1679. Available from doi: 10.1093/mnras/stu041.

Baldwin, J. A.; Phillips, M. M.; Terlevich, R., 1981. Classification parameters for the emission-line spectra of extragalactic objects. *Publications of the Astronomical Society of the Pacific*. Vol. 93, pp. 5–19. Available from doi: 10.1086/130766.

Ballantyne, D. R.; Draper, A. R.; Madsen, K. K.; Rigby, J. R.; Treister, E., 2011. Lifting the Veil on Obscured Accretion: Active Galactic Nuclei Number Counts and Survey Strategies for Imaging Hard X-Ray Missions. *The Astrophysical Journal*. Vol. 736, no. 1, p. 56. Available from doi: 10.1088/0004-637X/736/1/56.

Ballantyne, D. R.; Everett, J. E.; Murray, N., 2006. Connecting Galaxy Evolution, Star Formation, and the Cosmic X-Ray Background. *The Astrophysical Journal*. Vol. 639, no. 2, pp. 740–752. Available from doi: 10.1086/499558.

Balmaverde, B.; Capetti, A., 2013. Multi-band constraints on the nature of emission line galaxies. *Astronomy & Astrophysics*. Vol. 549, A144. Available from doi: 10.1051/0004-6361/201219426.

Baloković, M.; Brightman, M.; Harrison, F. A.; Comastri, A.; Ricci, C., et al., 2018. New Spectral Model for Constraining Torus Covering Factors from Broadband X-Ray Spectra of Active Galactic Nuclei. *The Astrophysical Journal*. Vol. 854, no. 1, p. 42. Available from doi: 10.3847/1538-4357/aaa7eb.

Baloković, M.; Cabral, S. E.; Brenneman, L.; Urry, C. M., 2021. Properties of the Obscuring Torus in NGC 1052 from Multiepoch Broadband X-Ray Spectroscopy. *The Astrophysical Journal*. Vol. 916, no. 2, p. 90. Available from doi: 10.3847/1538-4357/abff4d.

Bambi, Cosimo, 2017. *Black Holes: A Laboratory for Testing Strong Gravity*. Available from doi: 10.1007/978-981-10-4524-0.

Bambi, Cosimo, 2021. Testing General Relativity with Black Hole X-Ray Data. *Astronomy Reports*. Vol. 65, no. 10, pp. 902–905. Available from doi: 10.1134/S1063772921100024.

Beckmann, Volker; Shrader, Chris R., 2012. *Active Galactic Nuclei*.

Berger, M J; Hubbell, J H, 1987. XCOM: Photon cross sections on a personal computer. Available from doi: 10.2172/6016002.

Berney, Simon; Koss, Michael; Trakhtenbrot, Benny; Ricci, Claudio; Lamperti, Isabella, et al., 2015. BAT AGN spectroscopic survey–II. X-ray emission and high-ionization optical emission lines. *Monthly Notices of the Royal Astronomical Society*. Vol. 454, no. 4, pp. 3622–3634. issn 0035-8711. Available from doi: 10.1093/mnras/stv2181.

Bevington, Philip R., 1969. *Data reduction and error analysis for the physical sciences*.

Bianchi, S.; Guainazzi, M.; Chiaberge, M., 2006. The soft X-ray/NLR connection: a single photoionized medium? *Astronomy & Astrophysics*. Vol. 448, no. 2, pp. 499–511. Available from doi: 10.1051/0004-6361:20054091.

Blecha, Laura; Snyder, Gregory F; Satyapal, Shobita; Ellison, Sara L, 2017. The power of infrared AGN selection in mergers: a theoretical study. *Monthly Notices of the Royal Astronomical Society*. Vol. 478, no. 3, pp. 3056–3071. Available from doi: 10.1093/mnras/sty1274.

Boorman, Peter G.; Gandhi, Poshak; Baloković, Mislav; Brightman, Murray; Harrison, Fiona, et al., 2018. An Iwasawa-Taniguchi effect for Compton-thick active galactic nuclei. *Monthly Notices of the Royal Astronomical Society*. Vol. 477, no. 3, pp. 3775–3790. Available from doi: 10.1093/mnras/sty861.

Brandt, W. N.; Alexander, D. M., 2015. Cosmic X-ray surveys of distant active galaxies. The demographics, physics, and ecology of growing supermassive black holes. *Astronomy & Astrophysics Review*. Vol. 23, p. 1. Available from doi: 10.1007/s00159-014-0081-z.

Brightman, M.; Baloković, M.; Ballantyne, D. R.; Bauer, F. E.; Boorman, P., et al., 2017. X-Ray Bolometric Corrections for Compton-thick Active Galactic Nuclei. *The Astrophysical Journal*. Vol. 844, no. 1, p. 10. Available from doi: 10.3847/1538-4357/aa75c9.

Brightman, Murray; Nandra, Kirpal, 2011a. An XMM-Newton spectral survey of 12 μm selected galaxies - I. X-ray data. *Monthly Notices of the Royal Astronomical Society*. Vol. 413, no. 2, pp. 1206–1235. Available from doi: 10.1111/j.1365-2966.2011.18207.x.

Brightman, Murray; Nandra, Kirpal, 2011b. An XMM-Newton spectral survey of 12 μm selected galaxies - II. Implications for AGN selection and unification. *Monthly Notices of the Royal Astronomical Society*. Vol. 414, no. 4, pp. 3084–3104. Available from doi: 10.1111/j.1365-2966.2011.18612.x.

Brightman, Murray; Nandra, Kirpal; Salvato, Mara; Hsu, Li-Ting; Aird, James, et al., 2014. Compton thick active galactic nuclei in Chandra surveys. *Monthly Notices of the Royal Astronomical Society*. Vol. 443, no. 3, pp. 1999–2017. Available from doi: 10.1093/mnras/stu1175.

Brightman, Murray; Ueda, Yoshihiro, 2012. The evolution of the Compton thick fraction and the nature of obscuration for active galactic nuclei in the Chandra Deep Field South. *Monthly Notices of the Royal Astronomical Society*. Vol. 423, no. 1, pp. 702–717. Available from doi: 10.1111/j.1365-2966.2012.20908.x.

Brum, Carine; Riffel, Rogemar A.; Storchi-Bergmann, Thaisa; Robinson, Andrew; Schnorr Müller, Allan, et al., 2017. Dusty spirals versus gas kinematics in the inner kiloparsec of four low-luminosity active galactic nuclei. *Monthly Notices of the Royal Astronomical Society*. Vol. 469, no. 3, pp. 3405–3423. Available from doi: 10.1093/mnras/stx964.

Buchner, J.; Georgakakis, A.; Nandra, K.; Hsu, L.; Rangel, C., et al., 2014. X-ray spectral modelling of the AGN obscuring region in the CDFS: Bayesian model selection and catalogue. *Astronomy & Astrophysics*. Vol. 564, A125. Available from doi: 10.1051/0004-6361/201322971.

Buchner, Johannes; Bauer, Franz E., 2017. Galaxy gas as obscurer - II. Separating the galaxy-scale and nuclear obscurers of active galactic nuclei. *Monthly Notices of the Royal Astronomical Society*. Vol. 465, no. 4, pp. 4348–4362. Available from doi: 10.1093/mnras/stw2955.

Buchner, Johannes; Brightman, Murray; Nandra, Kirpal; Nikutta, Robert; Bauer, Franz E., 2019. X-ray spectral and eclipsing model of the clumpy obscurer in active galactic nuclei. *Astronomy & Astrophysics*. Vol. 629, A16. Available from doi: 10.1051/0004-6361/201834771.

Buchner, Johannes; Georgakakis, Antonis; Nandra, Kirpal; Brightman, Murray; Menzel, Marie-Luise, et al., 2015. Obscuration-dependent Evolution of Active Galactic Nuclei. *The Astrophysical Journal*. Vol. 802, no. 2, p. 89. Available from doi: 10.1088/0004-637X/802/2/89.

Buchner, Johannes; Schulze, Steve; Bauer, Franz E., 2017. Galaxy gas as obscurer - I. GRBs x-ray galaxies and find an $N_H{}^3\propto$ M_{star} relation. *Monthly Notices of the Royal Astronomical Society*. Vol. 464, no. 4, pp. 4545–4566. Available from doi: 10.1093/mnras/stw2423.

Cardamone, Carolin N.; Moran, Edward C.; Kay, Laura E., 2007. "Hidden" Seyfert 2 Galaxies in the Chandra Deep Field North. *The Astronomical Journal*. Vol. 134, no. 3, pp. 1263–1275. Available from doi: 10.1086/520801.

Carilli, C. L.; Walter, F., 2013. Cool Gas in High-Redshift Galaxies. *Annual Review of Astronomy and Astrophysics*. Vol. 51, no. 1, pp. 105–161. Available from doi: 10.1146/annurev-astro-082812-140953.

Cash, W., 1979. Parameter estimation in astronomy through application of the likelihood ratio. *The Astrophysical Journal*. Vol. 228, pp. 939–947. Available from doi: 10.1086/156922.

Comastri, A.; Gilli, R.; Marconi, A.; Risaliti, G.; Salvati, M., 2015. Mass without radiation: Heavily obscured AGNs, the X-ray background, and the black hole mass density. *Astronomy & Astrophysics*. Vol. 574, p. L10. Available from doi: 10.1051/0004-6361/201425496.

Comastri, A.; Setti, G.; Zamorani, G.; Hasinger, G., 1995. The contribution of AGNs to the X-ray background. *Astronomy & Astrophysics*. Vol. 296, p. 1. Available from arXiv: astro-ph/9409067 [astro-ph].

Comastri, Andrea, 2004. Compton-Thick AGN: The Dark Side of the X-Ray Background. In: *Supermassive Black Holes in the Distant Universe*. Ed. by Barger, Amy J. Dordrecht: Springer Netherlands, pp. 245–272. Available from doi: 10.1007/978-1-4020-2471-9_8.

Del Moro, A.; Alexander, D. M.; Bauer, F. E.; Daddi, E.; Kocevski, D. D., et al., 2016. Mid-infrared luminous quasars in the GOODS-Herschel fields: a large population of heavily obscured, Compton-thick quasars at z ≈ 2. *Monthly Notices of the Royal Astronomical Society*. Vol. 456, no. 2, pp. 2105–2125. Available from doi: 10.1093/mnras/stv2748.

Elitzur, Moshe; Shlosman, Isaac, 2006. The AGN-obscuring Torus: The End of the "Doughnut" Paradigm? *The Astrophysical Journal Letters*. Vol. 648, no. 2, pp. L101–L104. Available from doi: 10.1086/508158.

Elvis, Martin; Maccacaro, Tommaso; Wilson, A. S.; Ward, M. J.; Penston, M. V., et al., 1978. Seyfert galaxies as X-ray sources. *Monthly Notices of the Royal Astronomical Society*. Vol. 183, no. 2, pp. 129–157. Available from doi: 10.1093/mnras/183.2.129.

Esparza-Arredondo, Donaji; Osorio-Clavijo, Natalia; González-Martín, Omaira; Victoria-Ceballos, César; Haro-Corzo, Sinhué A. R., et al., 2020. Active Galactic Nucleus Ghosts: A Systematic Search for Faded Nuclei. *The Astrophysical Journal*. Vol. 905, no. 1, p. 29. Available from doi: 10.3847/1538-4357/abc425.

Fabian, A. C., 2006. A short introduction to broad and variable iron lines around black holes. *Astronomische Nachrichten*. Vol. 327, no. 10, p. 943. Available from doi: 10.1002/asna.200610669.

Fabian, A. C.; Iwasawa, K.; Reynolds, C. S.; Young, A. J., 2000. Broad Iron Lines in Active Galactic Nuclei. *The Publications of the Astronomical Society of the Pacific*. Vol. 112, no. 775, pp. 1145–1161. Available from doi: 10.1086/316610.

Fanaroff, B. L.; Riley, J. M., 1974. The Morphology of Extragalactic Radio Sources of High and Low Luminosity. *Monthly Notices of the Royal Astronomical Society*. Vol. 167, no. 1, 31P–36P. issn 0035-8711. Available from doi: 10.1093/mnras/167.1.31P.

Farrah, Duncan; Baloković, Mislav; Stern, Daniel; Harris, Kathryn; Kunimoto, Michelle, et al., 2016. The Geometry of the Infrared and X-Ray Obscurer in a Dusty Hyperluminous Quasar. *The Astrophysical Journal*. Vol. 831, no. 1, p. 76. Available from doi: 10.3847/0004-637X/831/1/76.

Feroz, F.; Hobson, M. P.; Bridges, M., 2009. MultiNest: an efficient and robust Bayesian inference tool for cosmology and particle physics. *Monthly Notices of the Royal Astronomical Society*. Vol. 398, no. 4, pp. 1601–1614. Available from doi: 10.1111/j.1365-2966.2009.14548.x.

Fiore, F.; Antonelli, L. A.; Ciliegi, P.; Comastri, A.; Giommi, P., et al., 2001. The BeppoSAX hellas survey: On the nature of faint hard X-ray selected sources. In: White, Nicholas E.; Malaguti, Giuseppe; Palumbo, Giorgio G. C. (eds.). *X-ray Astronomy: Stellar Endpoints, AGN, and the Diffuse X-ray Background*. Vol. 599, pp. 111–119. American Institute of Physics Conference Series. Available from doi: 10.1063/1.1434624.

Fiore, F.; La Franca, F.; Giommi, P.; Elvis, M.; Matt, G., et al., 1999. The contribution of faint active galactic nuclei to the hard X-ray background. *Monthly Notices of the Royal Astronomical Society*. Vol. 306, no. 4, pp. L55–L60. Available from doi: 10.1046/j.1365-8711.1999.02795.x.

Gabriel, C.; Denby, M.; Fyfe, D. J.; Hoar, J.; Ibarra, A., et al., 2004. The XMM-Newton SAS - Distributed Development and Maintenance of a Large Science Analysis System: A Critical Analysis. In: Ochsenbein, Francois; Allen, Mark G.; Egret, Daniel (eds.). *Astronomical Data Analysis Software and Systems (ADASS) XIII*. Vol. 314, p. 759. Astronomical Society of the Pacific Conference Series.

Gandhi, P.; Fabian, A. C.; Suebsuwong, T.; Malzac, J.; Miniutti, G., et al., 2007. Constraints on light bending and reflection from the hard X-ray background. *Monthly Notices of the Royal Astronomical Society*. Vol. 382, no. 3, pp. 1005–1018. Available from doi: 10.1111/j.1365-2966.2007.12462.x.

Gandhi, P.; Horst, H.; Smette, A.; Hönig, S.; Comastri, A., et al., 2009. Resolving the mid-infrared cores of local Seyferts. *Astronomy & Astrophysics*. Vol. 502, no. 2, pp. 457–472. Available from doi: 10.1051/0004-6361/200811368.

García-Burillo, S.; Alonso-Herrero, A.; Ramos Almeida, C.; González-Martín, O.; Combes, F., et al., 2021. The Galaxy Activity, Torus, and Outflow Survey (GATOS) - I. ALMA images of dusty molecular tori in Seyfert galaxies. *Astronomy & Astrophysics*. Vol. 652, A98. Available from doi: 10.1051/0004-6361/202141075.

Gaskell, C. Martin; Klimek, E. S.; Nazarova, L. S., 2007. The Structure of the Torus and Broad-line Region Of AGNs. In: *American Astronomical Society Meeting Abstracts*. Vol. 211, p. 118.02. American Astronomical Society Meeting Abstracts.

Ghosh, Himel; Pogge, Richard W.; Mathur, Smita; Martini, Paul; Shields, Joseph C., 2007. Chandra Observations of Candidate "True" Seyfert 2 Nuclei. *The Astrophysical Journal*. Vol. 656, no. 1, pp. 105–115. Available from doi: 10.1086/510421.

Giacconi, Riccardo; Gursky, Herbert; Paolini, Frank R.; Rossi, Bruno B., 1962. Evidence for x Rays From Sources Outside the Solar System. *Physical Review Letters*. Vol. 9, no. 11, pp. 439–443. Available from doi: 10.1103/PhysRevLett.9.439.

Gilli, R., 2013. The cosmic X-ray background: abundance and evolution of hidden black holes. *Memorie della Societa Astronomica Italiana*. Vol. 84, p. 647. Available from arXiv: 1304.3665 [astro-ph.CO].

Gilli, R.; Comastri, A.; Hasinger, G., 2007. The synthesis of the cosmic X-ray background in the Chandra and XMM-Newton era. *Astronomy & Astrophysics*. Vol. 463, no. 1, pp. 79–96. Available from doi: 10.1051/0004-6361:20066334.

Glass, I. S.; Moorwood, A. F. M.; Eichendorf, W., 1982. Mid-infrared observations of Seyfert 1 and narrow-line X-ray galaxies. *Astronomy & Astrophysics*. Vol. 107, pp. 276–282.

González-Martín, O.; Masegosa, J.; Márquez, I.; Guainazzi, M., 2009. FITTING LINER NUCLEI WITHIN THE ACTIVE GALACTIC NUCLEUS FAMILY: A MATTER OF OBSCURATION? *The Astrophysical Journal*. Vol. 704, no. 2, p. 1570. Available from doi: 10.1088/0004-637X/704/2/1570.

Guainazzi, M.; Matt, G.; Perola, G. C., 2005. X-ray obscuration and obscured AGN in the local universe. *Astronomy & Astrophysics*. Vol. 444, no. 1, pp. 119–132. Available from doi: 10.1051/0004-6361:20053643.

Guainazzi, Matteo; Bianchi, Stefano, 2007. On the origin of soft X-rays in obscured AGN: answers from high-resolution spectroscopy with XMM-Newton. *Monthly Notices of the Royal Astronomical Society*. Vol. 374, no. 4, pp. 1290–1302. Available from doi: 10.1111/j.1365-2966.2006.11229.x.

Harrison, Fiona A.; Craig, William W.; Christensen, Finn E.; Hailey, Charles J.; Zhang, William W., et al., 2013. The Nuclear Spectroscopic Telescope Array (NuSTAR) High-energy X-Ray Mission. *The Astrophysical Journal*. Vol. 770, no. 2, p. 103. Available from doi: 10.1088/0004-637X/770/2/103.

Hasinger, G.; Burg, R.; Giacconi, R.; Hartner, G.; Schmidt, M., et al., 1993. A deep X-ray survey in the Lockman hole and the soft X-ray log N-log S. *Astronomy & Astrophysics*. Vol. 275, pp. 1–15.

Heckman, T. M., 1980. An Optical and Radio Survey of the Nuclei of Bright Galaxies - Activity in the Normal Galactic Nuclei. *Astronomy & Astrophysics*. Vol. 87, p. 152.

Hickox, Ryan C.; Alexander, David M., 2018. Obscured Active Galactic Nuclei. *Annual Review of Astronomy and Astrophysics*. Vol. 56, no. 1, pp. 625–671. Available from doi: 10.1146/annurev-astro-081817-051803.

Hickox, Ryan C.; Markevitch, Maxim, 2006. Absolute Measurement of the Unresolved Cosmic X-Ray Background in the 0.5-8 keV Band with Chandra. *The Astrophysical Journal*. Vol. 645, no. 1, pp. 95–114. Available from doi: 10.1086/504070.

Ho, Luis C., 2009. RADIATIVELY INEFFICIENT ACCRETION IN NEARBY GALAXIES. *The Astrophysical Journal*. Vol. 699, no. 1, p. 626. Available from DOI: 10.1088/0004-637X/699/1/626.

Hönig, S. F.; Kishimoto, M.; Antonucci, R.; Marconi, A.; Prieto, M. A., et al., 2012. Parsec-scale Dust Emission from the Polar Region in the Type 2 Nucleus of NGC 424. *The Astrophysical Journal*. Vol. 755, no. 2, p. 149. Available from DOI: 10.1088/0004-637X/755/2/149.

Hönig, Sebastian F., 2019. Redefining the Torus: A Unifying View of AGNs in the Infrared and Submillimeter. *The Astrophysical Journal*. Vol. 884, no. 2, p. 171. Available from DOI: 10.3847/1538-4357/ab4591.

Huang, Shuang-an; Zhou, You-yuan; Wang, Ting-gui, 2000. In the big blue bump in active galactic nuclei peaked around 1050 Å ? *Chinese Astronomy and Astrophysics*. Vol. 24, no. 4, pp. 405–412. ISSN 0275-1062. Available from DOI: https://doi.org/10.1016/S0275-1062(00)00071-0.

Iwasawa, K.; Sanders, D. B.; Teng, S. H.; U, Vivian; Armus, L., et al., 2011. C-GOALS: Chandra observations of a complete sample of luminous infrared galaxies from the IRAS Revised Bright Galaxy Survey. *Astronomy & Astrophysics*. Vol. 529, A106. Available from DOI: 10.1051/0004-6361/201015264.

Iwasawa, Kazushi; Taniguchi, Yoshiaki, 1993. The X-Ray Baldwin Effect. *The Astrophysical Journal Letters*. Vol. 413, p. L15. Available from DOI: 10.1086/186948.

Kaastra, J. S.; Bleeker, J. A. M., 2016. Optimal binning of X-ray spectra and response matrix design. *Astronomy & Astrophysics*. Vol. 587, A151. Available from DOI: 10.1051/0004-6361/201527395.

Kammoun, E. S.; Miller, J. M.; Koss, M.; Oh, K.; Zoghbi, A., et al., 2020. A Hard Look at Local, Optically Selected, Obscured Seyfert Galaxies. *The Astrophysical Journal*. Vol. 901, no. 2, p. 161. Available from DOI: 10.3847/1538-4357/abb29f.

Kellermann, K. I.; Sramek, R.; Schmidt, M.; Shaffer, D. B.; Green, R., 1989. VLA Observations of Objects in the Palomar Bright Quasar Survey. *Astronomical Journal*. Vol. 98, p. 1195. Available from DOI: 10.1086/115207.

Khachikian, E. Y.; Weedman, D. W., 1974. An atlas of Seyfert galaxies. *The Astrophysical Journal*. Vol. 192, pp. 581–589. Available from DOI: 10.1086/153093.

Koratkar, Anuradha; Blaes, Omer, 1999. The Ultraviolet and Optical Continuum Emission in Active Galactic Nuclei: The Status of Accretion Disks. *The Publications of the Astronomical Society of the Pacific*. Vol. 111, no. 755, pp. 1–30. Available from DOI: 10.1086/316294.

Krabbe, Alfred; Böker, Torsten; Maiolino, Roberto, 2001. N-Band Imaging of Seyfert Nuclei and the Mid-Infrared-X-Ray Correlation. *The Astrophysical Journal*. Vol. 557, no. 2, p. 626. Available from DOI: 10.1086/321679.

Krause, M. O., 1979. Atomic radiative and radiationless yields for K and L shells. *Journal of Physical and Chemical Reference Data*. Vol. 8, no. 2, pp. 307–327. Available from doi: 10.1063/1.555594.

Krolik, Julian H., 1999. *From the Central Black Hole to the Galactic Environment*. Princeton: Princeton University Press. isbn 9780691227474. Available from doi: doi:10.1515/9780691227474.

Krolik, Julian H.; Begelman, Mitchell C., 1988. Molecular Tori in Seyfert Galaxies: Feeding the Monster and Hiding It. *The Astrophysical Journal*. Vol. 329, p. 702. Available from doi: 10.1086/166414.

Kuraszkiewicz, Joanna; Wilkes, Belinda J.; Atanas, Adam; Buchner, Johannes; McDowell, Jonathan C., et al., 2021. Beyond Simple AGN Unification with Chandra-observed 3CRR Sources at 0.5 < z < 1. *The Astrophysical Journal*. Vol. 913, no. 2, p. 134. Available from doi: 10.3847/1538-4357/abf3c0.

LaMassa, Stephanie M.; Heckman, T. M.; Ptak, A., 2012. DISENTANGLING AGN AND STAR FORMATION IN SOFT X-RAYS. *The Astrophysical Journal*. Vol. 758, no. 2, p. 82. Available from doi: 10.1088/0004-637X/758/2/82.

LaMassa, Stephanie M.; Heckman, T. M.; Ptak, A.; Martins, L.; Wild, V., et al., 2011. Uncovering Obscured Active Galactic Nuclei in Homogeneously Selected Samples of Seyfert 2 Galaxies. *The Astrophysical Journal*. Vol. 729, no. 1, p. 52. Available from doi: 10.1088/0004-637X/729/1/52.

Lawrence, A., 1991. The relative frequency of broad-lined and narrow-lined active galactic nuclei : implications for unified schemes. *Monthly Notices of the Royal Astronomical Society*. Vol. 252, p. 586. Available from doi: 10.1093/mnras/252.4.586.

Leftley, James H.; Hönig, Sebastian F.; Asmus, Daniel; Tristram, Konrad R. W.; Gandhi, Poshak, et al., 2019. Parsec-scale Dusty Winds in Active Galactic Nuclei: Evidence for Radiation Pressure Driving. *The Astrophysical Journal*. Vol. 886, no. 1, p. 55. Available from doi: 10.3847/1538-4357/ab4a0b.

Lehmann, I.; Hasinger, G.; Schmidt, M.; Gunn, J. E.; Schneider, D. P., et al., 2000. The ROSAT Deep Survey. III. Optical spectral properties of X-ray sources in the Lockman Hole. *Astronomy & Astrophysics*. Vol. 354, pp. 35–54. Available from arXiv: astro-ph/9911484 [astro-ph].

Levenberg, Kenneth, 1944. A METHOD FOR THE SOLUTION OF CERTAIN NON-LINEAR PROBLEMS IN LEAST SQUARES. *Quarterly of Applied Mathematics* [online]. Vol. 2, no. 2, pp. 164–168 [visited on 2022-12-06]. issn 0033569X, issn 15524485. Available from: http://www.jstor.org/stable/43633451.

Li, Anqi; Marasco, Antonino; Fraternali, Filippo; Trager, Scott; Verheijen, Marc A W, 2021. A kinematic analysis of ionized extraplanar gas in the spiral galaxies NGC 3982 and NGC 4152. *Monthly Notices of the Royal Astronomical Society*. Vol. 504, no. 2, pp. 3013–3028. issn 0035-8711. Available from doi: 10.1093/mnras/stab1043.

Liu, Jiren; Hönig, Sebastian F.; Ricci, Claudio; Paltani, Stéphane, 2019. X-ray signatures of the polar dusty gas in AGN. *Monthly Notices of the Royal Astronomical Society*. Vol. 490, no. 3, pp. 4344–4352. Available from doi: 10.1093/mnras/stz2908.

Liu, Teng; Wang, Jun-Xian, 2010. The Difference in Narrow Fe Kα Line Emission Between Seyfert 1 and Seyfert 2 Galaxies. *The Astrophysical Journal*. Vol. 725, no. 2, pp. 2381–2391. Available from doi: 10.1088/0004-637X/725/2/2381.

Liu, Yuan; Li, Xiaobo, 2014. An X-Ray Spectral Model for Clumpy Tori in Active Galactic Nuclei. *The Astrophysical Journal*. Vol. 787, no. 1, p. 52. Available from doi: 10.1088/0004-637X/787/1/52.

Longair, Malcolm S., 2011. *High Energy Astrophysics*.

Lutz, D.; Maiolino, R.; Spoon, H. W. W.; Moorwood, A. F. M., 2004. The relation between AGN hard X-ray emission and mid-infrared continuum from ISO spectra: Scatter and unification aspects ***. *A&A*. Vol. 418, no. 2, pp. 465–473. Available from doi: 10.1051/0004-6361:20035838.

Madsen, Kristin; Hickox, Ryan; Bachetti, Matteo; Stern, Daniel; Gellert, Nis C., et al., 2019. HEX-P: The High-Energy X-ray Probe. *Bulletin of the AAS*. Vol. 51, no. 7. https://baas.aas.org/pub/2020n7i166.

Magdziarz, Pawel; Zdziarski, Andrzej A., 1995. Angle-dependent Compton reflection of X-rays and gamma-rays. *Monthly Notices of the Royal Astronomical Society*. Vol. 273, no. 3, pp. 837–848. Available from doi: 10.1093/mnras/273.3.837.

Markowitz, A. G.; Krumpe, M.; Nikutta, R., 2014. First X-ray-based statistical tests for clumpy-torus models: eclipse events from 230 years of monitoring of Seyfert AGN. *Monthly Notices of the Royal Astronomical Society*. Vol. 439, no. 2, pp. 1403–1458. Available from doi: 10.1093/mnras/stt2492.

Marquardt, Donald W., 1963. An Algorithm for Least-Squares Estimation of Nonlinear Parameters. *Journal of the Society for Industrial and Applied Mathematics* [online]. Vol. 11, no. 2, pp. 431–441 [visited on 2022-12-06]. issn 03684245. Available from: http://www.jstor.org/stable/2098941.

Mateos, S.; Carrera, F. J.; Barcons, X.; Alonso-Herrero, A.; Hernán-Caballero, A., et al., 2017. Survival of the Obscuring Torus in the Most Powerful Active Galactic Nuclei. *The Astrophysical Journal Letters*. Vol. 841, no. 2, p. L18. Available from doi: 10.3847/2041-8213/aa7268.

Matt, G.; Fabian, A. C.; Guainazzi, M.; Iwasawa, K.; Bassani, L., et al., 2000. The X-ray spectra of Compton-thick Seyfert 2 galaxies as seen by BeppoSAX. *Monthly Notices of the Royal Astronomical Society*. Vol. 318, no. 1, pp. 173–179. Available from doi: 10.1046/j.1365-8711.2000.03721.x.

McKaig, Jeffrey; Ricci, Claudio; Paltani, Stéphane; Satyapal, Shobita, 2022. X-ray simulations of polar gas in accreting supermassive black holes. *Monthly Notices of the Royal Astronomical Society*. Vol. 512, no. 2, pp. 2961–2971. Available from doi: 10.1093/mnras/stab3178.

Mor, Rivay; Netzer, Hagai; Elitzur, Moshe, 2009. Dusty Structure Around Type-I Active Galactic Nuclei: Clumpy Torus Narrow-line Region and Near-nucleus Hot Dust. *The Astrophysical Journal*. Vol. 705, no. 1, pp. 298–313. Available from doi: 10.1088/0004-637X/705/1/298.

Moran, Edward C.; Kay, Laura E.; Davis, Marc; Filippenko, Alexei V.; Barth, Aaron J., 2001. A Composite Seyfert 2 X-Ray Spectrum: Implications for the Origin of the Cosmic X-Ray Background. *The Astrophysical Journal*. Vol. 556, no. 2, p. L75. Available from doi: 10.1086/322991.

Murphy, Kendrah D.; Yaqoob, Tahir, 2009. An X-ray spectral model for Compton-thick toroidal reprocessors. *Monthly Notices of the Royal Astronomical Society*. Vol. 397, no. 3, pp. 1549–1562. Available from doi: 10.1111/j.1365-2966.2009.15025.x.

Mushotzky, R. F.; Cowie, L. L.; Barger, A. J.; Arnaud, K. A., 2000. Resolving the extragalactic hard X-ray background. *Nature*. Vol. 404, no. 6777, pp. 459–464. Available from doi: 10.1038/35006564.

Nenkova, Maia; Sirocky, Matthew M.; Ivezić, Željko; Elitzur, Moshe, 2008a. AGN Dusty Tori. I. Handling of Clumpy Media. *The Astrophysical Journal*. Vol. 685, no. 1, pp. 147–159. Available from doi: 10.1086/590482.

Nenkova, Maia; Sirocky, Matthew M.; Nikutta, Robert; Ivezić, Željko; Elitzur, Moshe, 2008b. AGN Dusty Tori. II. Observational Implications of Clumpiness. *The Astrophysical Journal*. Vol. 685, no. 1, pp. 160–180. Available from doi: 10.1086/590483.

Netzer, H., 1990. AGN emission lines. In: Blandford, R. D.; Netzer, H.; Woltjer, L.; Courvoisier, T. J. -L.; Mayor, M. (eds.). *Active Galactic Nuclei*, pp. 57–160.

Novak, Gregory S., 2013. Local Black Hole Scaling Relations Imply Compton Thick or Super Eddington Accretion. *arXiv e-prints*, arXiv:1310.3833. Available from arXiv: 1310.3833 [astro-ph.CO].

Odaka, Hirokazu; Yoneda, Hiroki; Takahashi, Tadayuki; Fabian, Andrew, 2016. Sensitivity of the Fe Kα Compton shoulder to the geometry and variability of the X-ray illumination of cosmic objects. *Monthly Notices of the Royal Astronomical Society*. Vol. 462, no. 3, pp. 2366–2381. Available from doi: 10.1093/mnras/stw1764.

Osterbrock, D. E., 1981. Seyfert galaxies with weak broad H alpha emission lines. *The Astrophysical Journal*. Vol. 249, pp. 462–470. Available from doi: 10.1086/159306.

Paltani, S.; Ricci, C., 2017. RefleX: X-ray absorption and reflection in active galactic nuclei for arbitrary geometries. *Astronomy & Astrophysics*. Vol. 607, A31. Available from doi: 10.1051/0004-6361/201629623.

Panessa, F.; Bassani, L.; Cappi, M.; Dadina, M.; Barcons, X., et al., 2006. On the X-ray, optical emission line and black hole mass properties of local Seyfert galaxies. *Astronomy & Astrophysics*. Vol. 455, no. 1, pp. 173–185. Available from doi: 10.1051/0004-6361:20064894.

Penzias, A. A.; Wilson, R. W., 1965. A Measurement of Excess Antenna Temperature at 4080 Mc/s. *The Astrophysical Journal*. Vol. 142, pp. 419–421. Available from doi: 10.1086/148307.

Peterson, Bradley M., 1997. *An Introduction to Active Galactic Nuclei*. Cambridge University Press. Available from doi: 10.1017/CBO9781139170901.

Quillen, A. C.; McDonald, Colleen; Alonso-Herrero, A.; Lee, Ariane; Shaked, Shanna, et al., 2001. The Multitude of Unresolved Continuum Sources at 1.6 Microns in Hubble Space Telescope Images of Seyfert Galaxies. *The Astrophysical Journal*. Vol. 547, no. 1, p. 129. Available from doi: 10.1086/318328.

Ramos Almeida, C.; García, A. M. Pérez; Acosta-Pulido, J. A.; Espinosa, J. M. Rodríguez, 2007. The Mid-Infrared Emission of Seyfert Galaxies: A New Analysis of ISOCAM Data*. *The Astronomical Journal*. Vol. 134, no. 5, p. 2006. Available from doi: 10.1086/522625.

Ramos Almeida, Cristina; Ricci, Claudio, 2017. Nuclear obscuration in active galactic nuclei. *Nature Astronomy*. Vol. 1, pp. 679–689. Available from doi: 10.1038/s41550-017-0232-z.

Ricci, C.; Bauer, F. E.; Treister, E.; Schawinski, K.; Privon, G. C., et al., 2017a. Growing supermassive black holes in the late stages of galaxy mergers are heavily obscured. *Monthly Notices of the Royal Astronomical Society*. Vol. 468, no. 2, pp. 1273–1299. Available from doi: 10.1093/mnras/stx173.

Ricci, C.; Trakhtenbrot, B.; Koss, M. J.; Ueda, Y.; Del Vecchio, I., et al., 2017b. BAT AGN Spectroscopic Survey. V. X-Ray Properties of the Swift/BAT 70-month AGN Catalog. *The Astrophysical Journal Supplement Series*. Vol. 233, no. 2, p. 17. Available from doi: 10.3847/1538-4365/aa96ad.

Ricci, C.; Ueda, Y.; Koss, M. J.; Trakhtenbrot, B.; Bauer, F. E., et al., 2015. Compton-thick Accretion in the Local Universe. *The Astrophysical Journal Letters*. Vol. 815, no. 1, p. L13. Available from doi: 10.1088/2041-8205/815/1/L13.

Ricci, C.; Ueda, Y.; Paltani, S.; Ichikawa, K.; Gandhi, P., et al., 2014. Iron Kα emission in type-I and type-II active galactic nuclei. *Monthly Notices of the Royal Astronomical Society*. Vol. 441, no. 4, pp. 3622–3633. issn 0035-8711. Available from doi: 10.1093/mnras/stu735.

Ricci, Claudio, 2011. *Active galactic nuclei at hard X-ray energies: absorption, reflection and the unified model*. PhD thesis. University of Geneva, Switzerland.

Ricci, Claudio; Trakhtenbrot, Benny; Koss, Michael J.; Ueda, Yoshihiro; Schawinski, Kevin, et al., 2017c. The close environments of accreting massive black holes are shaped by radiative feedback. *Nature*. Vol. 549, no. 7673, pp. 488–491. Available from doi: 10.1038/nature23906.

Risaliti, G.; Elvis, M.; Nicastro, F., 2002. Ubiquitous Variability of X-Ray-absorbing Column Densities in Seyfert 2 Galaxies. *The Astrophysical Journal*. Vol. 571, no. 1, pp. 234–246. Available from doi: 10.1086/324146.

Rowan-Robinson, Michael, 1995. A new model for the infrared emission of quasars. *Monthly Notices of the Royal Astronomical Society*. Vol. 272, no. 4, pp. 737–748. Available from doi: 10.1093/mnras/272.4.737.

Rush, Brian; Malkan, Matthew A., 1996. The Soft X-Ray Spectral Shape of X-Ray–weak Seyfert Galaxies. *The Astrophysical Journal*. Vol. 456, p. 466. Available from doi: 10.1086/176672.

Rybicki, G. B.; Lightman, A. P., 1979. Book-Review - Radiative Processes in Astrophysics. *Astronomy Quarterly*. Vol. 3, p. 199.

Saade, M. Lynne; Brightman, Murray; Stern, Daniel; Malkan, Matthew A.; García, Javier A., 2022. NuSTAR Observations of AGNs with Low Observed X-Ray to [O III] Luminosity Ratios: Heavily Obscured AGNs or Turned-off AGNs? *The Astrophysical Journal*. Vol. 936, no. 2, p. 162. Available from doi: 10.3847/1538-4357/ac88cf.

Setti, G.; Woltjer, L., 1989. Active galactic nuclei and the spectrum of the X-ray background. *Astronomy & Astrophysics*. Vol. 224, pp. L21–L23.

Seyfert, Carl K., 1943. Nuclear Emission in Spiral Nebulae. *The Astrophysical Journal*. Vol. 97, p. 28. Available from doi: 10.1086/144488.

Shu, X. W.; Wang, J. X.; Jiang, P.; Fan, L. L.; Wang, T. G., 2007. Investigating the Nuclear Obscuration in Two Types of Seyfert 2 Galaxies. *The Astrophysical Journal*. Vol. 657, no. 1, pp. 167–176. Available from doi: 10.1086/510579.

Siemiginowska, A.; Kashyap, V.; Refsdal, B.; van Dyk, D.; Connors, A., et al., 2011. pyblocxs: Bayesian Low-Counts X-ray Spectral Analysis in Sherpa. In: Evans, I. N.; Accomazzi, A.; Mink, D. J.; Rots, A. H. (eds.). *Astronomical Data Analysis Software and Systems XX*. Vol. 442, p. 439. Astronomical Society of the Pacific Conference Series.

Skilling, John, 2004. Nested Sampling. In: Fischer, Rainer; Preuss, Roland; Toussaint, Udo Von (eds.). *Bayesian Inference and Maximum Entropy Methods in Science and Engineering: 24th International Workshop on Bayesian Inference and Maximum Entropy Methods in Science and Engineering*. Vol. 735, pp. 395–405. American Institute of Physics Conference Series. Available from doi: 10.1063/1.1835238.

Smith, M.J.S.; Guainazzi, M., 2022. *EPIC Status of Calibration and Data Analysis*. Tech. rep. EPIC Consortium.

Stalevski, Marko; Ricci, Claudio; Ueda, Yoshihiro; Lira, Paulina; Fritz, Jacopo, et al., 2016. The dust covering factor in active galactic nuclei. *Monthly Notices of the Royal Astronomical Society*. Vol. 458, no. 3, pp. 2288–2302. Available from doi: 10.1093/mnras/stw444.

Stern, D.; Lansbury, G. B.; Assef, R. J.; Brandt, W. N.; Alexander, D. M., et al., 2014. NuSTAR and XMM-Newton Observations of Luminous, Heavily Obscured, WISE-selected Quasars at z ∼2. *The Astrophysical Journal*. Vol. 794, no. 2, p. 102. Available from doi: 10.1088/0004-637X/794/2/102.

Thorne, K.S.; Price, R.H.; MacDonald, D.A., 1986. *Black Holes: The Membrane Paradigm*. Yale University Press. The Silliman Memorial Lectures Series. isbn 9780300037708. Available also from: https://books.google.sk/books?id=T94hD5rR8oYC.

Treister, E.; Urry, C. Megan; Virani, Shanil, 2009. The Space Density of Compton-Thick Active Galactic Nucleus and the X-Ray Background. *The Astrophysical Journal*. Vol. 696, no. 1, pp. 110–120. Available from doi: 10.1088/0004-637X/696/1/110.

Treister, Ezequiel; Urry, C. Megan, 2005. Active Galactic Nuclei Unification and the X-Ray Background. *The Astrophysical Journal*. Vol. 630, no. 1, pp. 115–121. Available from doi: 10.1086/431892.

Trippe, M. L.; Crenshaw, D. M.; Deo, R. P.; Dietrich, M.; Kraemer, S. B., et al., 2010. A Multi-wavelength Study of the Nature of Type 1.8/1.9 Seyfert Galaxies. *The Astrophysical Journal*. Vol. 725, no. 2, pp. 1749–1767. Available from doi: 10.1088/0004-637X/725/2/1749.

Tristram, Konrad R. W.; Burtscher, Leonard; Jaffe, Walter; Meisenheimer, Klaus; Hönig, Sebastian F., et al., 2014. The dusty torus in the Circinus galaxy: a dense disk and the torus funnel. *Astronomy & Astrophysics*. Vol. 563, A82. Available from doi: 10.1051/0004-6361/201322698.

Ueda, Yoshihiro; Akiyama, Masayuki; Hasinger, Günther; Miyaji, Takamitsu; Watson, Michael G., 2014. Toward the Standard Population Synthesis Model of the X-Ray Background: Evolution of X-Ray Luminosity and Absorption Functions of Active Galactic Nuclei Including Compton-thick Populations. *The Astrophysical Journal*. Vol. 786, no. 2, p. 104. Available from doi: 10.1088/0004-637X/786/2/104.

Ueda, Yoshihiro; Akiyama, Masayuki; Ohta, Kouji; Miyaji, Takamitsu, 2003. Cosmological Evolution of the Hard X-Ray Active Galactic Nucleus Luminosity Function and the Origin of the Hard X-Ray Background. *The Astrophysical Journal*. Vol. 598, no. 2, pp. 886–908. Available from doi: 10.1086/378940.

Ueda, Yoshihiro; Eguchi, Satoshi; Terashima, Yuichi; Mushotzky, Richard; Tueller, Jack, et al., 2007. Suzaku Observations of Active Galactic Nuclei Detected in the Swift BAT Survey: Discovery of a "New Type" of Buried Supermassive Black Holes. *The Astrophysical Journal Letters*. Vol. 664, no. 2, pp. L79–L82. Available from doi: 10.1086/520576.

Urry, C. Megan; Padovani, Paolo, 1995. Unified Schemes for Radio-Loud Active Galactic Nuclei. *Publications of the Astronomical Society of the Pacific*. Vol. 107, p. 803. Available from doi: 10.1086/133630.

van Dyk, David A.; Connors, Alanna; Kashyap, Vinay L.; Siemiginowska, Aneta, 2001. Analysis of Energy Spectra with Low Photon Counts via Bayesian Posterior Simulation. *The Astrophysical Journal*. Vol. 548, no. 1, p. 224. Available from doi: 10.1086/318656.

Venanzi, Marta; Hönig, Sebastian; Williamson, David, 2020. The Role of Infrared Radiation Pressure in Shaping Dusty Winds in AGNs. *The Astrophysical Journal*. Vol. 900, no. 2, p. 174. Available from doi: 10.3847/1538-4357/aba89f.

Verner, D. A.; Yakovlev, D. G., 1995. Analytic FITS for partial photoionization cross sections. *Astronomy and Astrophysics Suppl.* Vol. 109, pp. 125–133.

Wachter, K.; Leach, R.; Kellogg, E., 1979. Parameter estimation in X-ray astronomy using maximum likelihood. *The Astrophysical Journal*. Vol. 230, pp. 274–287. Available from doi: 10.1086/157084.

Ward, M. J.; Done, C.; Fabian, A. C.; Tennant, A. F.; Shafer, R. A., 1988. X-Ray Observations of IRAS Selected Seyfert Galaxies and Obscuration of the Broad-Line Region. *The Astrophysical Journal*. Vol. 324, p. 767. Available from doi: 10.1086/165935.

Wilms, J.; Allen, A.; McCray, R., 2000. On the Absorption of X-Rays in the Interstellar Medium. *The Astrophysical Journal*. Vol. 542, no. 2, pp. 914–924. Available from doi: 10.1086/317016.

XRISM Science Team, 2020. *Science with the X-ray Imaging and Spectroscopy Mission (XRISM)*. arXiv. Available from doi: 10.48550/ARXIV.2003.04962.

Appendix

A BXA posterior distributions

This section shows the posterior probability distributions in corresponding corner plots, each displaying 1D and 2D marginalized posteriors for all the fitted parameters showing 5σ intervals with uncertainties marked by dashed lines indicating 95% (2σ) interval.

The corner plots are showing all the fitted parameters with default names from the individual models with the posterior means and the corresponding uncertainties as plotted by the horizontal dashed lines in the histograms. Shown parameters in the columns (rows) are displayed as following, from left to right (top to bottom). All normalizations are in units of keV/cm^2/s and column densities in cm^{-2}.

PEXRAV: (1) logarithm of the intrinsic column density in units of 10^{22} cm^{-2}; (2) photon index Γ; (3) logarithm of power-law normalization; (4) negative value of the logarithm of relative reflection; (5) cosine of the inclination angle; (6) logarithm of the scattering fraction; (7) logarithm of the `apec` temperature in keV and (8) `apec` normalization and (9) normalization of the fluorescent Fe Kα line.

BORUS02 coupled: (1) logarithm of the `apec` temperature in keV and (2) `apec` normalization; (3) photon index; (4) logarithm of the global column density of the torus; (5) covering factor of the torus; (6) cosine of the inclination angle; (7) logarithm of the power-law normalization and (8) logarithm of the scattering fraction.

BORUS02 decoupled: (1) logarithm of the `apec` temperature in keV and (2) `apec` normalization; (3) photon index; (4) logarithm of the global column density of the torus; (5) covering factor of the torus; (6) logarithm of the line-of-sight column density; (7) logarithm of the power-law normalization and (8) logarithm of the scattering fraction.

MYTorus: (1) logarithm of the scattering fraction; (2) logarithm of the `apec` temperature; (3) `apec` normalization; (4) photon index Γ; (5) logarithm of

the power-law normalization; (6) logarithm of the global column density in units of 10^{24} cm^{-2} and (7) cosine of the inclination angle.

UxClumpy: (1) logarithm of the `apec` temperature; (2) `apec` normalization; (3) logarithm of the line-of-sight column density in units of 10^{24} cm^{-2}; (4) photon index; (5) cosine of `TORsigma`; (6) CTK covering factor; (7) cosine of the inclination angle; (8) logarithm of power-law normalization and (9) logarithm of the scattering fraction.

RXTorus: (1) logarithm of the `apec` temperature, (2) `apec` normalization; (3) logarithm of the scattering fraction; (4) photon index; (5) logarithm of the equatorial column density in units of 10^{22} cm^{-2}; (6) cosine of inclination; (7) covering factor as fraction r/R and (8) logarithm of the normalization of the power-law.

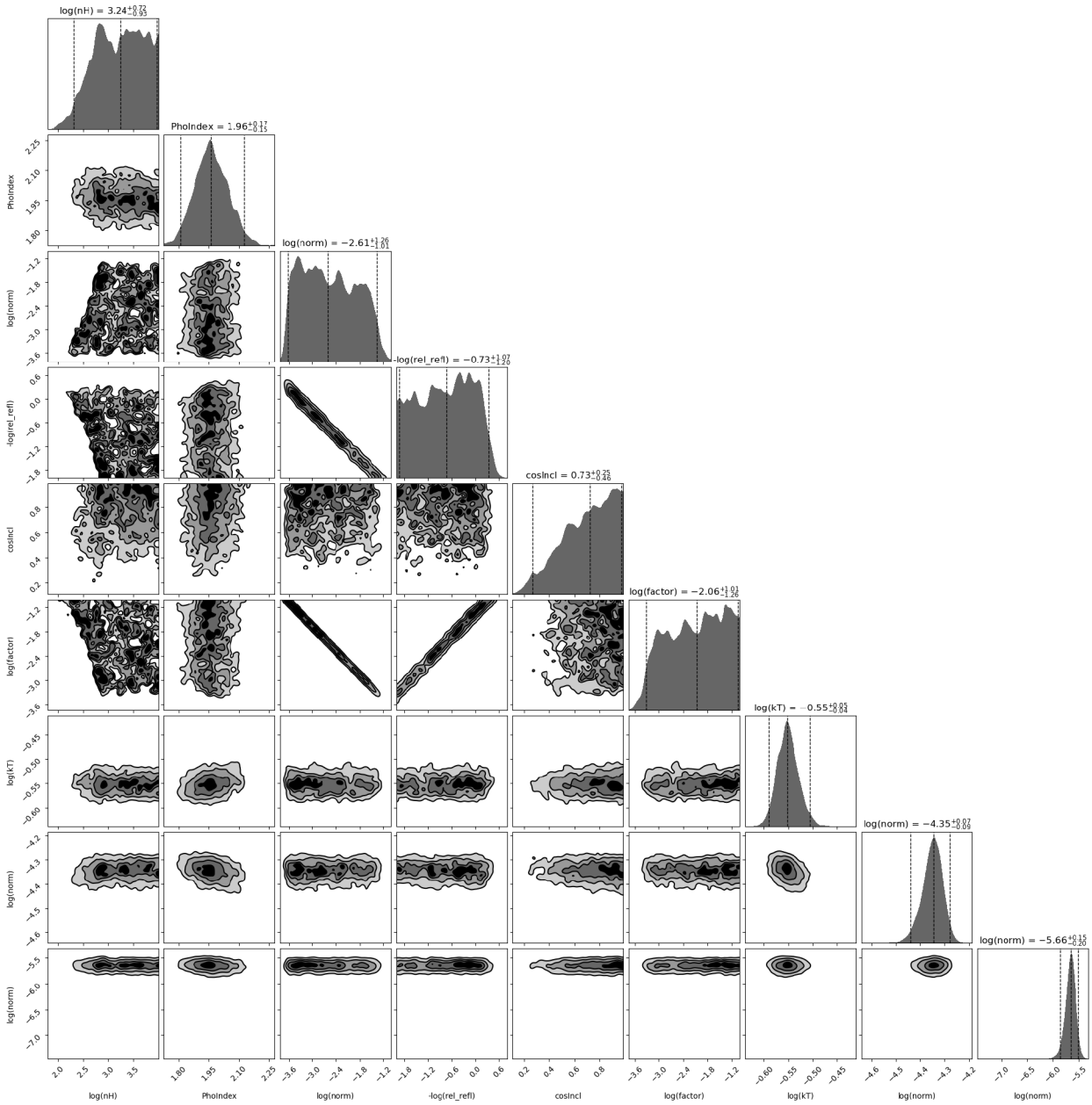

Figure 9: A parameter posterior plot is corner plot showing the posterior probability distributions for the PEXRAV model.

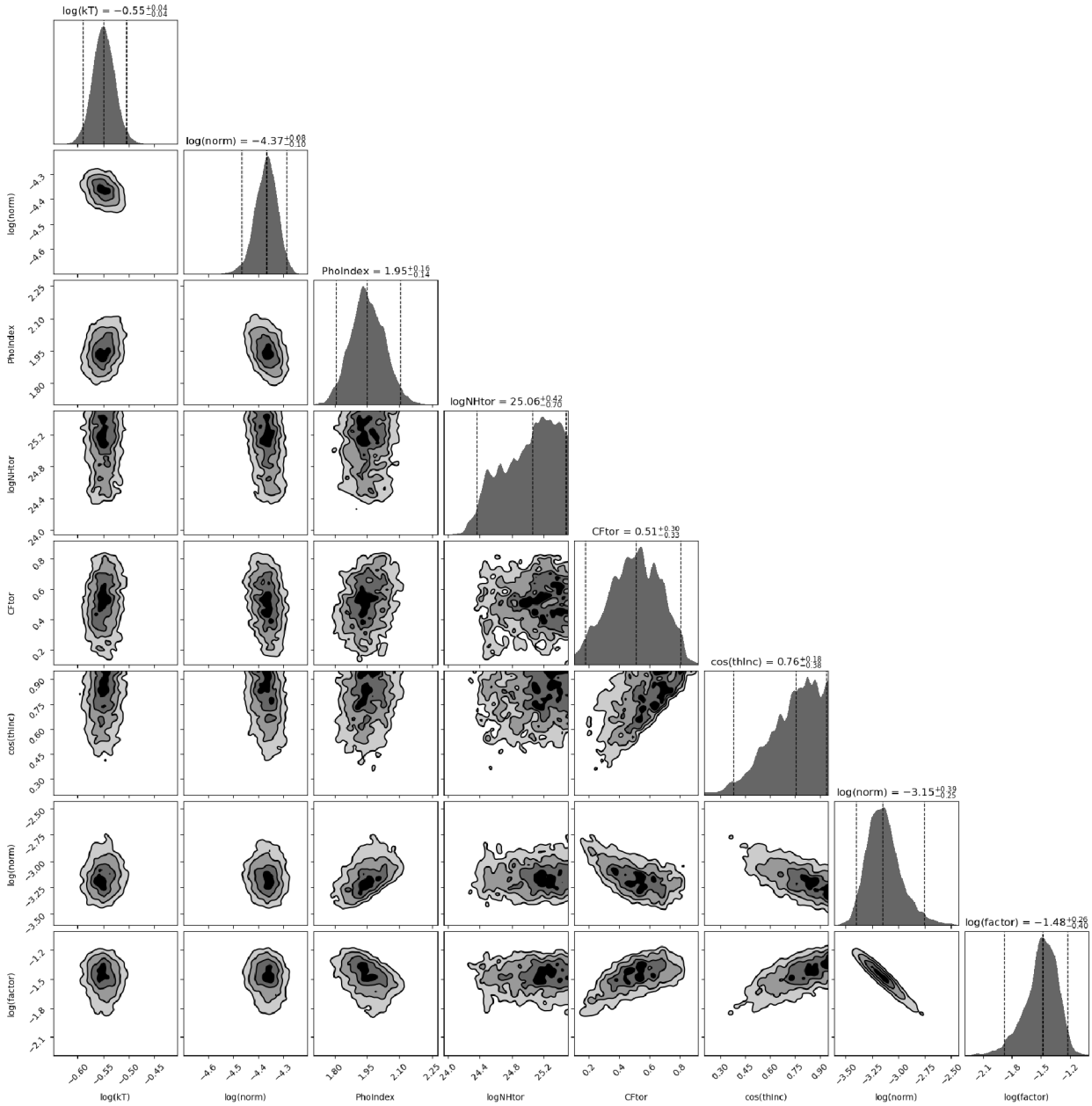

Figure 10: A corner plot showing the posterior probability distributions for the BORUS02 model in the coupled mode.

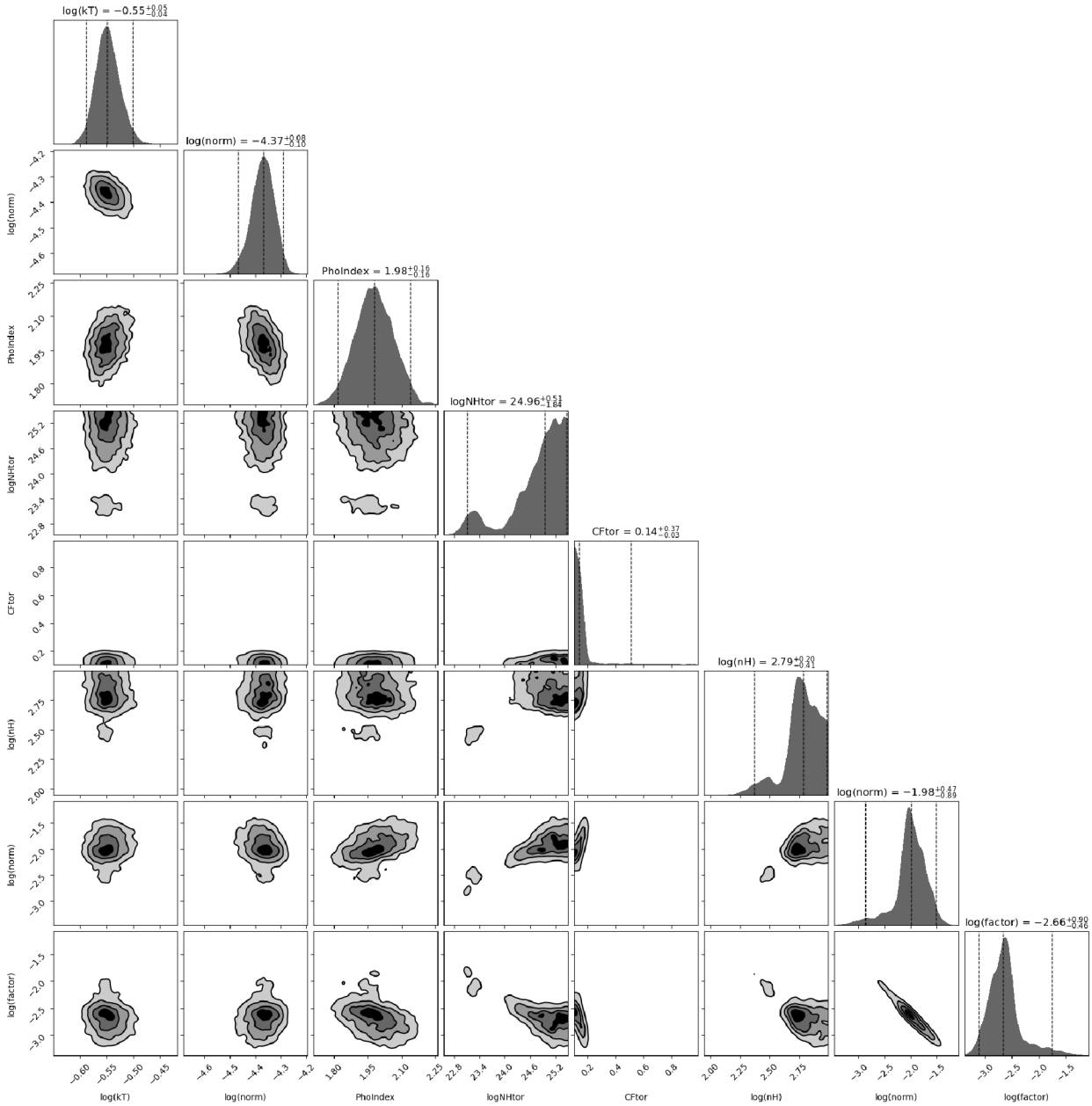

Figure 11: A corner plot showing the posterior probability distributions for the BORUS02 model in the decoupled mode.

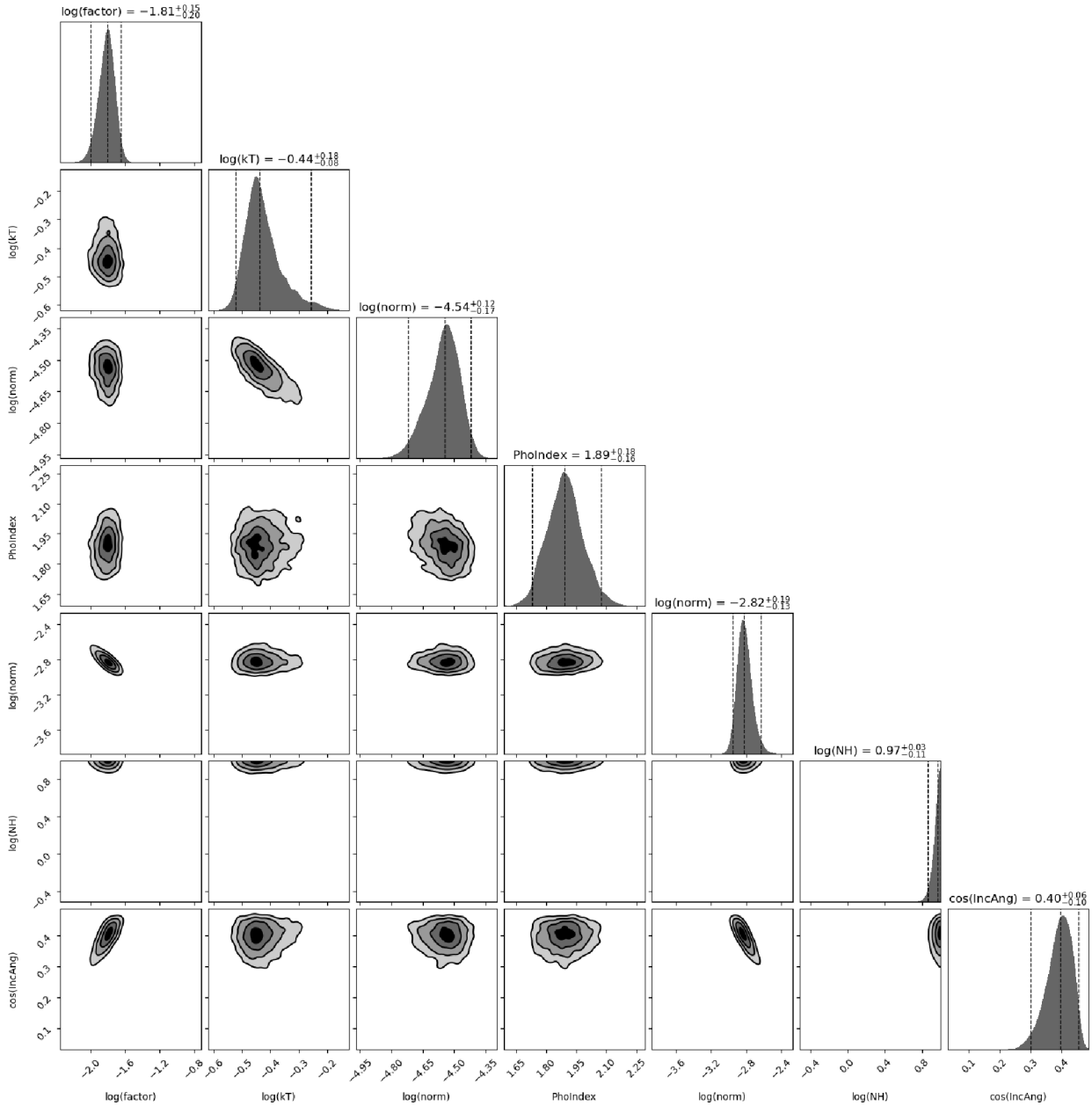

Figure 12: A corner plot showing the posterior probability distributions for the MYTorus model.

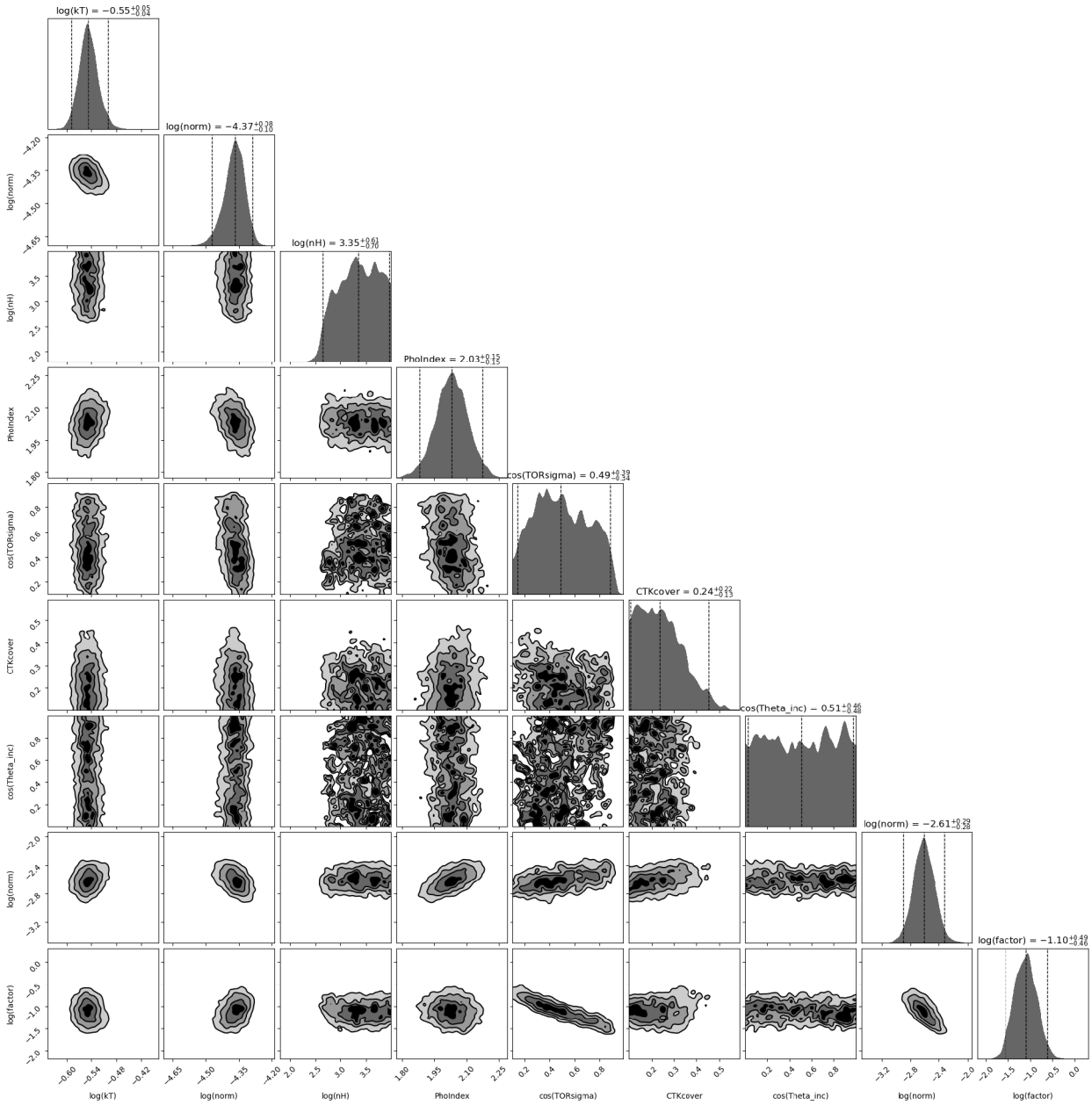

Figure 13: A corner plot showing the posterior probability distributions for the UxClumpy model.

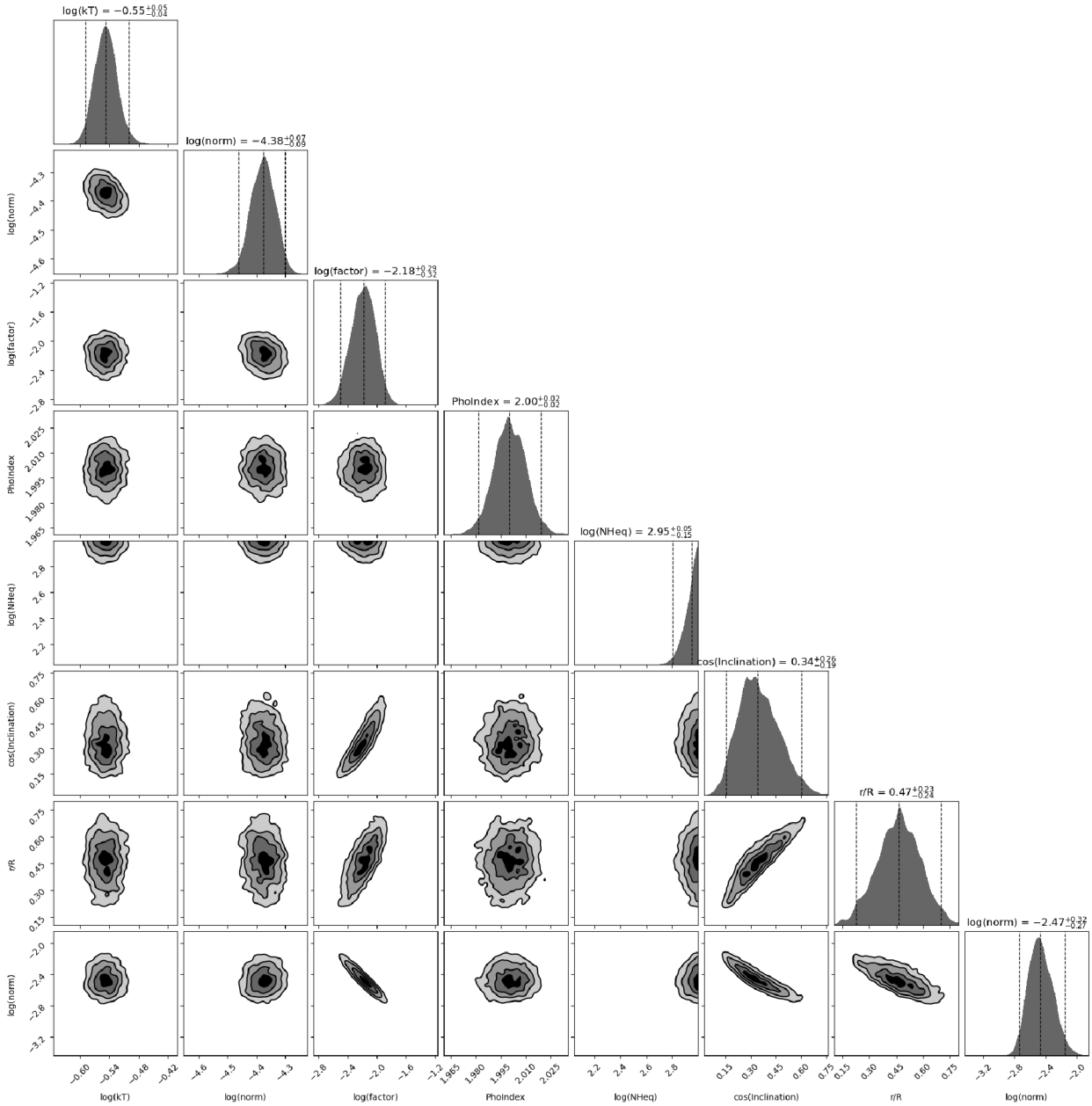

Figure 14: A corner plot showing the posterior probability distributions for the RXTorus model.

B Modelling method comparison

This section shows the comparison between the two modelling methods applied in this work, as described in section sec:coparison. For each model, the histograms on left-hand sided column show the BXA posterior distributions for each of the fitted parameters in *blue* and the best-fitted values of the fitted parameters from the local parameter estimation in XSPEC (in *orange*). The red solid line displays the 99% BXA quantile distribution from which the initial parameter guesses were randomly drawn. The histograms on the right-hand side show the same BXA distributions in *blue* and the best-fitted values of the fitted parameters from the local parameter estimation in XSPEC in *orange* but with the posterior samples used for the initial parameter guess for the local modelling.

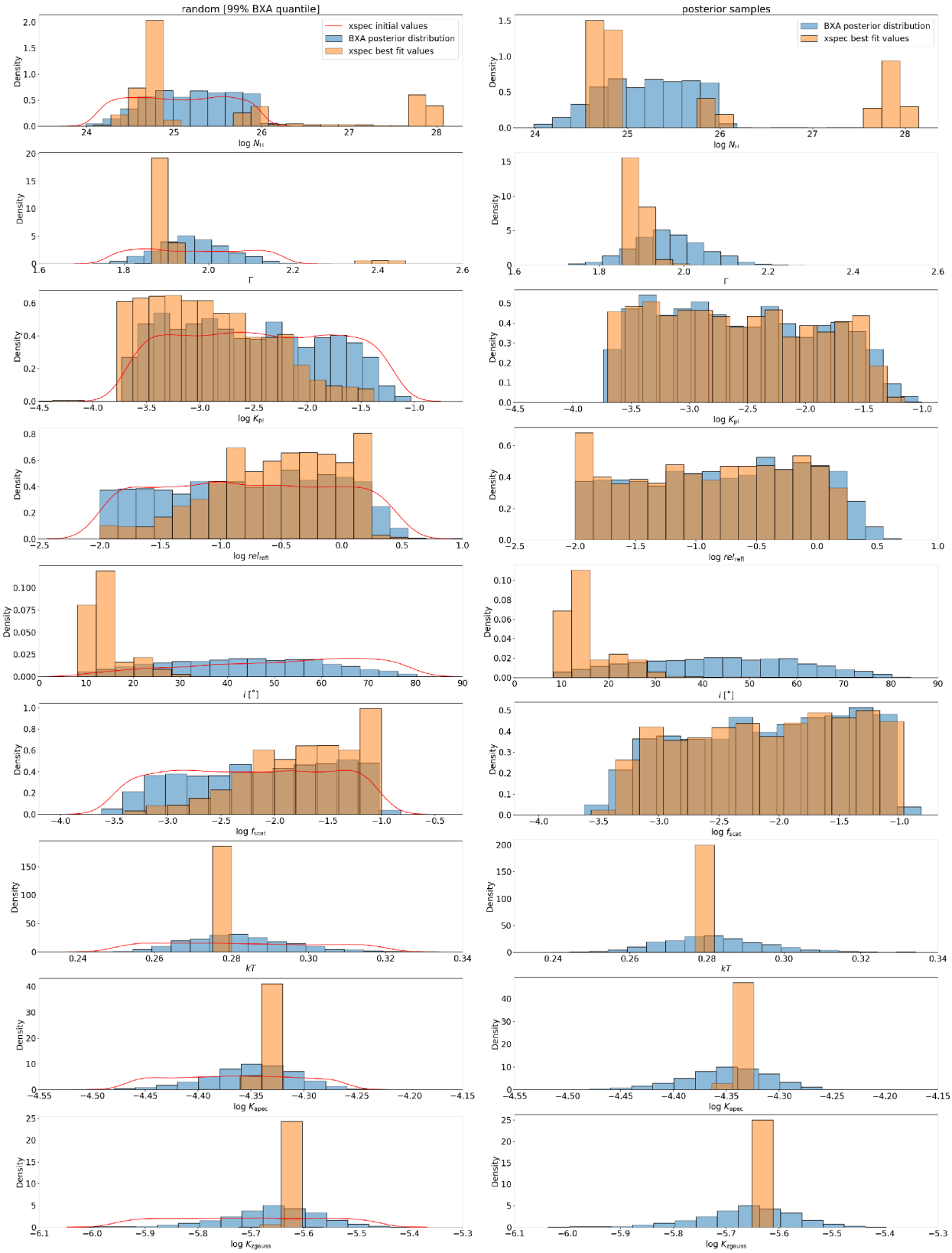

Figure 15: Histograms for PEXRAV with random selection of the initial parameter guess (*left*) and with BXA posterior samples used for the initial parameter guess (*right*).

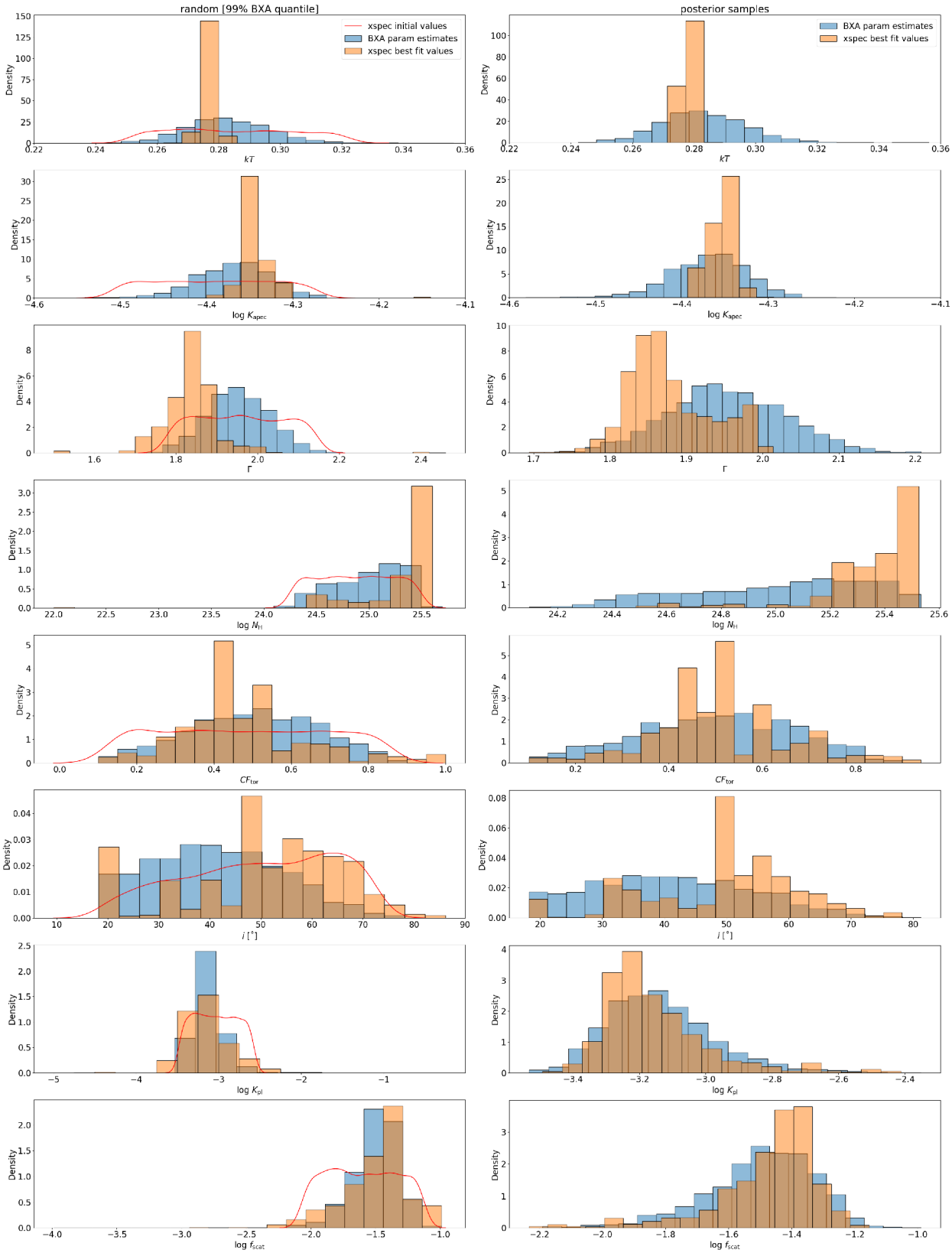

Figure 16: Histograms for BORUS02 coupled with random selection of the initial parameter guess (*left*) and with BXA posterior samples used for the initial parameter guess (*right*).

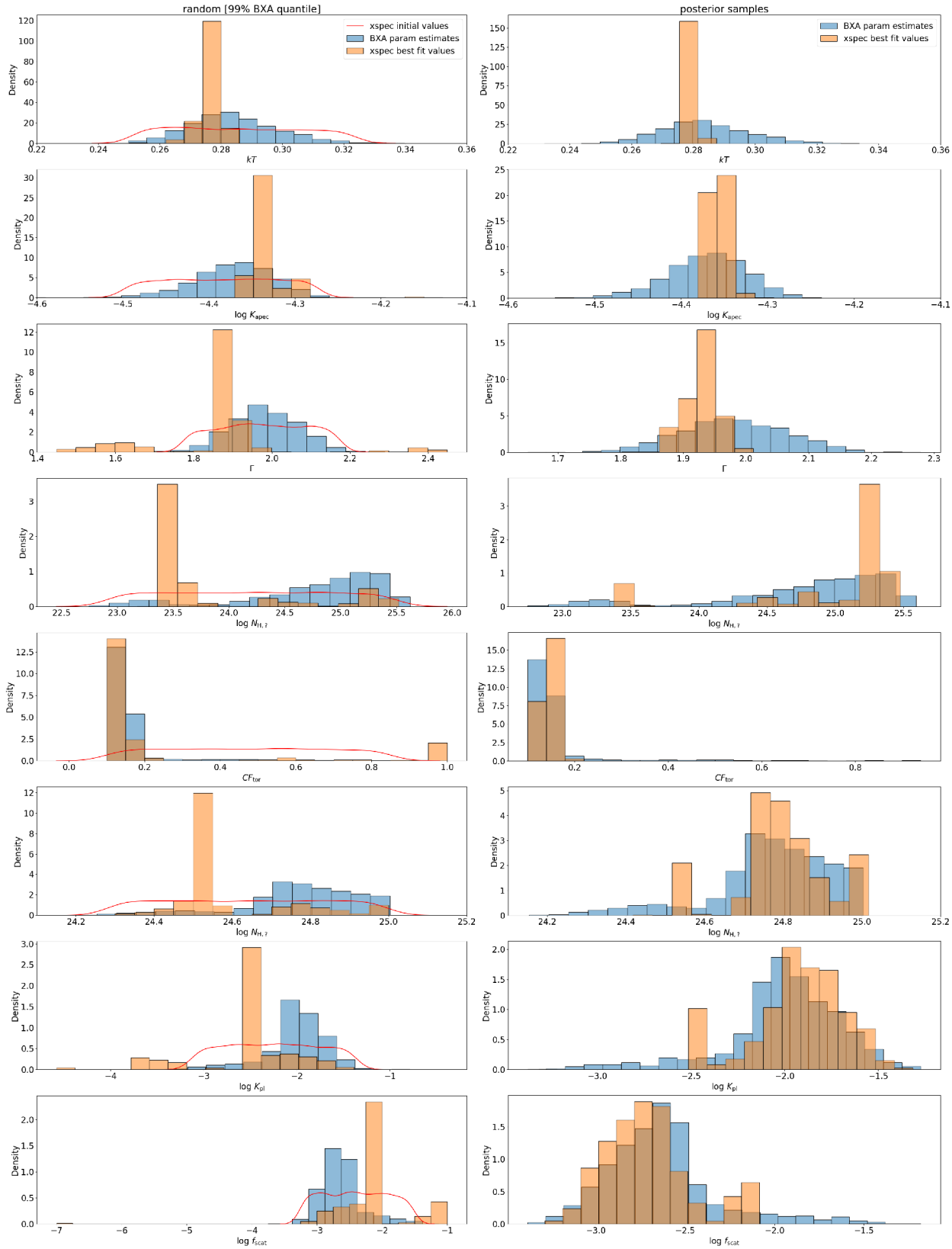

Figure 17: Histograms for BORUS02 decoupled with random selection of the initial parameter guess (*left*) and with BXA posterior samples used for the initial parameter guess (*right*).

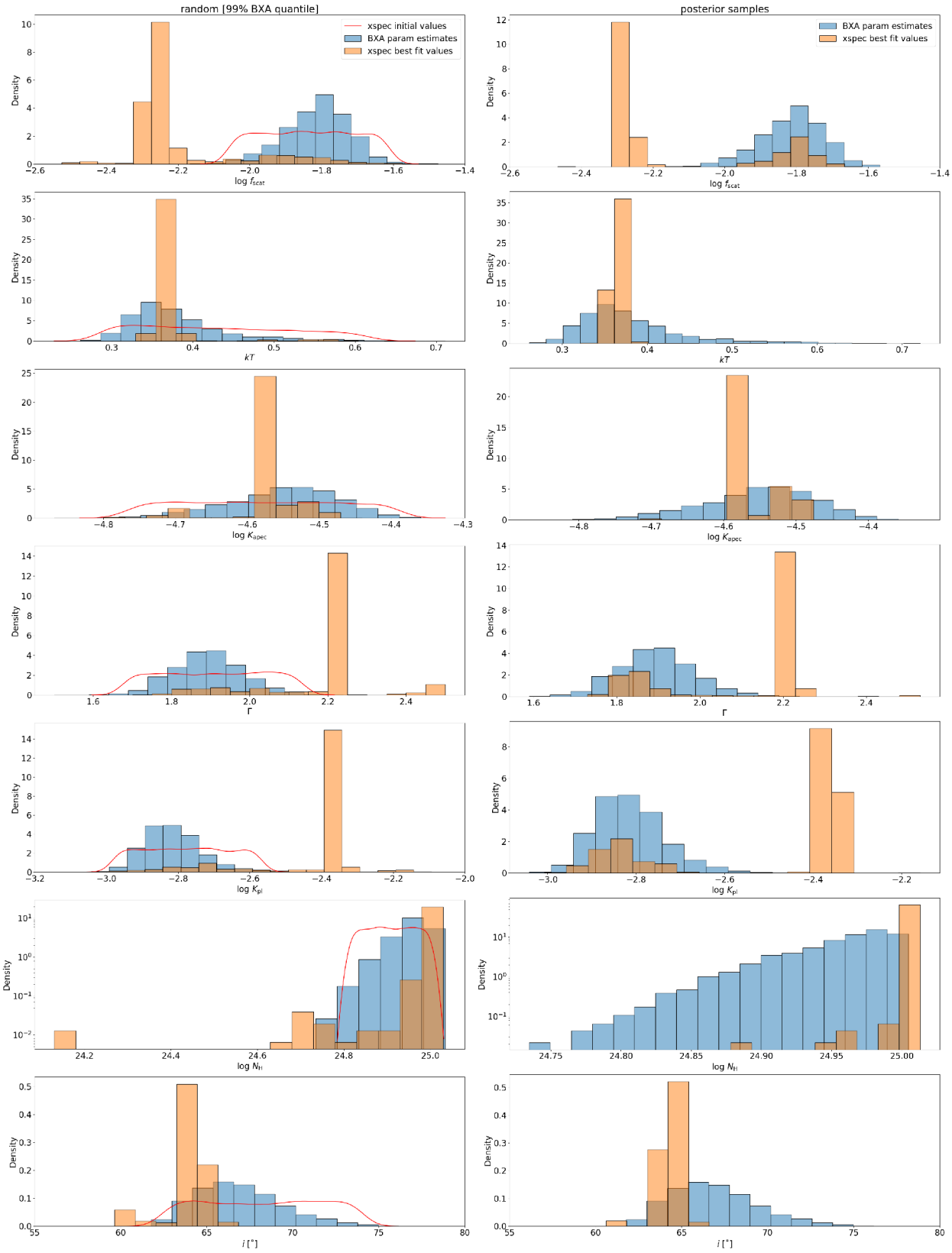

Figure 18: Histograms for MYTorus with random selection of the initial parameter guess (*left*) and with BXA posterior samples used for the initial parameter guess (*right*).

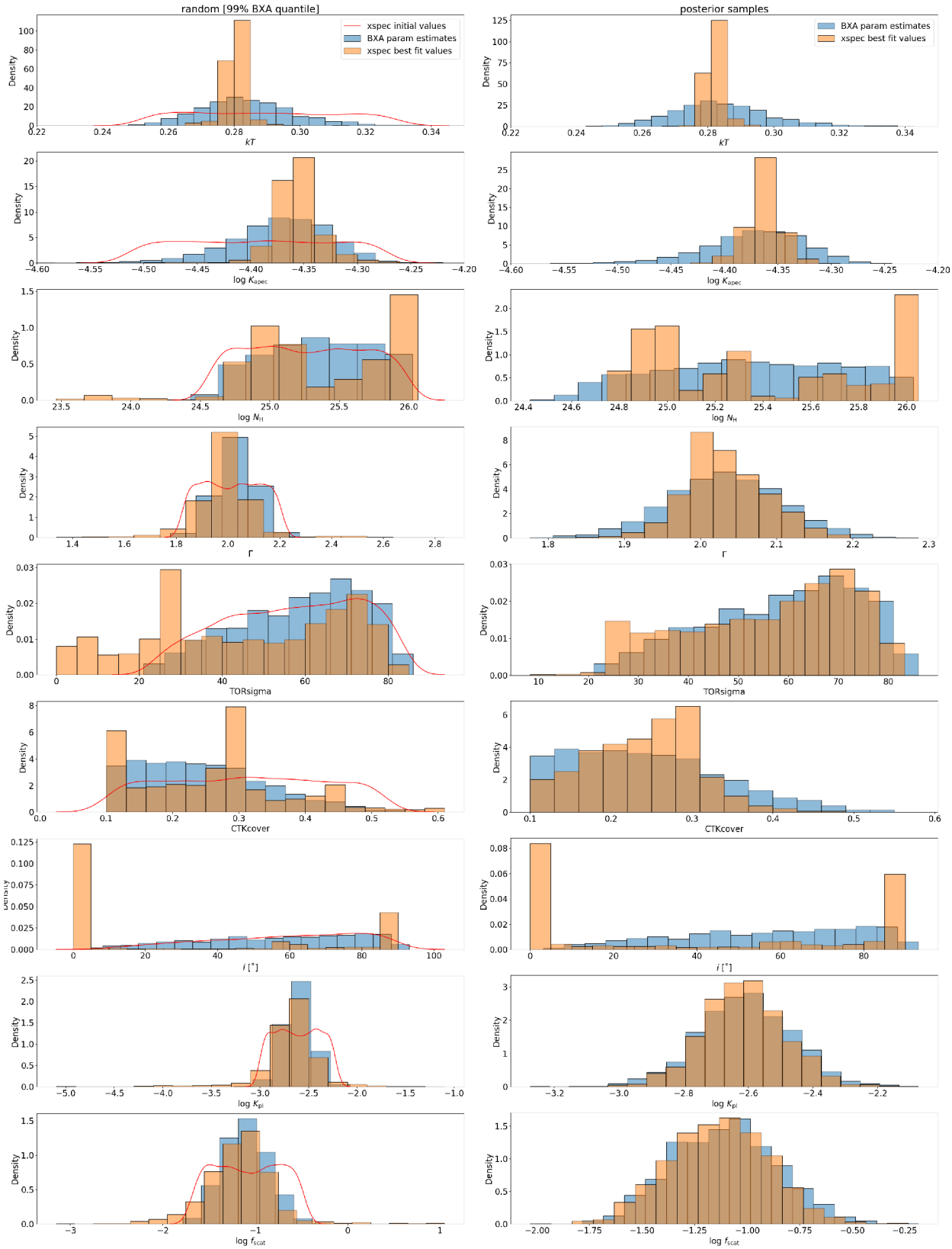

Figure 19: Histograms for UxClumpy with random selection of the initial parameter guess (*left*) and with BXA posterior samples used for the initial parameter guess (*right*).

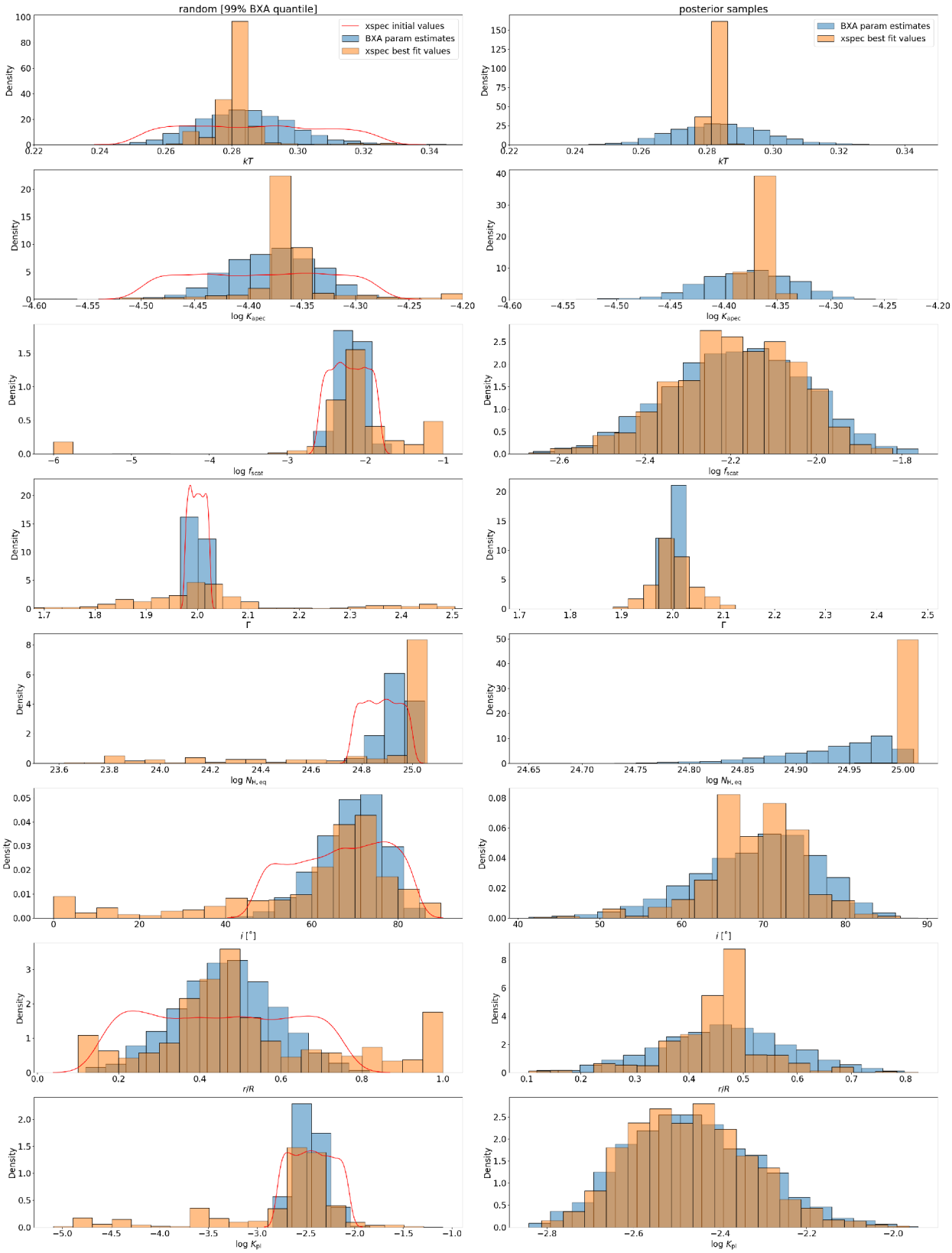

Figure 20: Histograms for RXTorus with random selection of the initial parameter guess (*left*) and with BXA posterior samples used for the initial parameter guess (*right*).